UNIVERSITY OF CALIFORNIA,
IRVINE

Analysis and Design of Passive and Active Transmission Lines with Coupled Modes with Exceptional Points of Degeneracy

DISSERTATION

submitted in partial satisfaction of the requirements
for the degree of

DOCTOR OF PHILOSOPHY

in Electrical and Computer Engineering

by

Farshad Yazdi

Dissertation Committee:

Professor Filippo Capolino, Chair
Professor Michael Green
Professor Henry Lee
Professor Ozdal Boyraz

2021

Dedication

To my lovely Persian parents who mean the world to me!

TABLE OF CONTENTS

	Page
LIST OF FIGURES	v
VITA	xvi
ABSTRACT OF THE DISSERTATION	xviii
Chapter 1 Introduction	1
Sec. 1.1 The Concept of Exceptional Points of Degeneracy	1
Sec. 1.2 Degenerate Band Edge (DBE)	3
Sec. 1.3 Third Order EPD (SIP)	5
Sec. 1.4 Sixth Order EPD (6DBE)	6
Sec. 1.5 Content of Each Chapter	7
References	10
Chapter 2 A New Amplification Regime for TWTs with third Order Modal Degeneracy	14
Sec. 2.1 Motivation	14
Sec. 2.2 Background and Problem Statement	18
Sec. 2.3 Cold SWS Featuring SIP	21
Sec. 2.4 Hot SWS Featuring SIP	29
Sec. 2.5 Conclusion	43
Appendix A Dispersion Relation for Interaction of the SWS with Electron Beam	45
Appendix B SWS and Beam Parameters Used in Simulations	50
References	53
Chapter 3 Third Order Modal Exceptional Degeneracy in *PT*-Glide Symmetric Microstrip Waveguides	57
Sec. 3.1 Motivation	57
Sec. 3.2 Periodic Three-way Coupled Waveguide	61
Sec. 3.3 Finite-Length Structure: Properties and Performance	76
Sec. 3.4 Conclusion	79
Appendix A Parameters Used in Simulations	80
Appendix B Transfer Matrix Formalism	81
References	83

CHAPTER 4 Wigner Time and LDOS Enhancement in Photonic Crystals with a DBE 86
Sec. 4.1 Motivation 86
Sec. 4.2 Electromagnetic Waves in Stratified Media 92
Sec. 4.3 Transfer Matrix for One Unit Cell 94
Sec. 4.4 Periodic Structure with *N* Cascaded Unit Cells 97
Sec. 4.5 Wigner Time and Local Density of States 101
Sec. 4.6 Conclusion 105
Appendix A Transformation of **T** Matrix into **T** Matrix Formalism 105
Appendix B Proof of Formula for **T**^*N* in Terms of **T** 106
References 111
CHAPTER 5 Triple Ladder Lumped Circuit with Sixth Order Modal Degeneracy 113
Sec. 5.1 Motivation 113
Sec. 5.2 Triple Ladder Circuit Theory 117
Sec. 5.3 Resonance Behavior of the Periodic Circuit 123
Sec. 5.4 Conclusion 129
Appendix A Transfer Matrix Formalism and Calculation 130
References 132
CHAPTER 6 Experimental Demonstration of Sixth Order Degenerate Band Edge in Coupled Microstrip Waveguides 135
Sec. 6.1 Motivation 135
Sec. 6.2 Exceptional Degeneracy of 6th Order 138
Sec. 6.3 Resonance of Passive Cascaded Circuit 142
Sec. 6.4 Experimental Verification of 6DBE in Periodic Microstrip Circuit 145
Sec. 6.5 Conclusion 148
References 149

LIST OF FIGURES

Page

Fig. 1.1 Dispersion relations of arbitrary periodic structures exhibiting EPDs with different orders of modal degeneracy at angular frequency ω_e and the coalescence of the modes at the same point with $k = k_e$ with: (a) Third order EPD (b) Fourth order EPD (c) Sixth order EPD. 2

Fig. 1.2 Example geometries of different periodic structures potentially supporting DBE condition: (a) lumped double ladder circuit [25] (b) printed microstrip lines (c) photonic crystal [14] (d) circular metallic waveguide [28]. 4

Fig. 2.1 (a) Schematic of a periodic CTLs consisting of three TLs that mimic a SWS supporting three coupled eigenmodes. The unit cell, of period d, is made of two segments (shown by different colors). Each segment is described using TLs distributed parameters. (b) Generalized Pierce model for the three CTL interacting with an electron beam. The dependent current sources are used in the generalized Pierce model to describe the interaction of the charge wave modulating the electron beam with the RF signal in the SWS. (c) Typical modal dispersion diagram, where only branches with purely real Floquet-Bloch wavenumbers are shown, of a periodic "cold" three CTLs (without including the beam interaction) having SIP at angular frequency ω_{SIP}. The beam line shows the charge wave velocity to be synchronized with the three RF modes in the TLs that is introduced in (2) and discussed in Sec. 2.4. Dispersion diagrams for the combined CTL-electron beam interactive system are shown in Sec. 2.4-A and Appendix A. This Result is obtained by F. Yazdi and M. Veysi using Matlab. 17

Fig. 2.2 (a) Finite length of a three CTLs periodic structure, with total length $L = Nd$ including loading and excitation, where N is the number of unit cells shown in Fig. (3.1). (b) Magnitude of the voltage transfer function $TF_1 = V_{out1}/V_{in1}$ for different number of unit cells (N = 8, 16, 24) with $Z_{s1} = Z_{L1} = 75\Omega$ and short circuit at all the other ports. This Result is obtained by F. Yazdi and M. Veysi using Matlab. 25

Fig. 2.3 (a) Engineering the slope of the upper branch of the dispersion diagram in Fig. 2.1 to have positive and negative slopes around the SIP compared to the ideal SIP case of zero group velocity (in blue). (b) Magnitude of the voltage transfer function $TF_1 = V_{out1}/V_{in}$ in dB for three different scenarios of ideal, tilted-positive and tilted negative dispersion relation around the SIP, for N = 16 unit cells with $Z_{s1} = Z_{L1} = 75\Omega$ and short circuit at all the other ports. The result is obtained by F. Yazdi. 26

Fig. 2.4 (a) Comparison of three different loading scenarios for the finite three CTL structure. (b) Magnitude of the voltage transfer function of the two schemes of ideal SIP and tilted-positive for two cases of no loss and lossy structures when we have N = 16 unit cells with $Z_{s1} = Z_{L1} = 75\Omega$ and short circuit at other ports as loading. This Result is obtained by F. Yazdi, M. Othman, and M. Veysi. 28

Fig. 2.5 Conceptual example of a three CTL structure interacting with an electron beam with the generalized Pierce model of the three CTLs, with unit cells as shown in Fig. 2.1(b) including the per unit length parameters. The blocks Un represent unit cells made of the two segments A and B in Figs. 2.1(a) and 2.2, with parameters given in Appendix B. 30

Fig. 2.6 Dispersion diagrams showing the real part of the complex Floquet-Bloch wavenumber k versus angular frequency, for both the “hot” and “cold” systems. Dispersion curves for the “hot” SWS-electron beam interactive system (shown in solid red lines) are

calculated using an electron beam current of I_0 = 0.5A. Dispersion curves for the "cold" lossless SWS are shown with solid blue lines that are under the red curves (hence not visible) except for a small region near the interaction point (k_{SIP}, ω_{SIP}) given in (2). Zooms and more detailed plots of the dispersion diagram for various beam currents are reported in Appendix A. This result is obtained by F. Yazdi, and M. Othman. 32

Fig. 2.7 Imaginary part of the pole nearest to SIP plotted versus beam current I_0 for four different scenarios: (i) tilted-negative regime (oscillator application) assuming loading scenario 1; (ii) ideal SIP regime assuming loading scenario 1; (iii) ideal SIP regime assuming loading scenario 3; (iv) tilted-positive regime (amplifier application) assuming loading scenario 3. The system is unstable when a pole has Im[ω]<0. The "tilted-positive" case is the most stable. This result is obtained by F. Yazdi. 35

Fig. 2.8 (a) Comparison of the power gain $GP_1=P_{L1}/P_{smax}$ for both the ideal and the tilted-positive SIP regimes interacting with an electron beam in which the value of beam current is selected such that the maximum power gain is set to be either 10 dB or 25 dB. (b) Power gain at each of the three output ports and the total output power gain GP, for a regime of operation based on the SWS with tilted-positive group velocity. For both plots the gain is calculated for a SWS with N = 16 unit cells with Z_{Li} = 75Ω, i = 1,2,3, Z_{s1} = 75Ω and open circuit for the two other input ports. We show only convective instability regimes of operation. This Result is obtained by F. Yazdi and M. Veysi. 38

Fig. 2.9 (a) Power gain (in dB) of the proposed ideal SIP and tilted-positive regimes of TWT operation, compared with a standard regime of amplification based on a finite, periodic TL, modeling a single mode TWT, having the same characteristic impedance, length and loading plotted versus the beam current. Results are based on structures with N = 16 unit

cells, with loads of Z_L = 75Ω (loading scenario 3) and R_{loss} = 5 Ω/m. (b) Total power gain versus the number of SWS unit cells, *N*. Comparison among amplification regimes based on SWS with the ideal SIP, the titled-positive dispersion, and a single TL model introduced in part (a). The values of the electron beam current are selected for each regime such that the same gain is achieved for the case of *N* = 8 unit cells. The resulting electron beam current values for the ideal and tilted-positive SIP is 263 mA, in both cases, whereas for single TL regime the beam current is 385 mA. The threshold beam currents (I_{th}) for ideal, tilted-SIP, and 1TL are 560 mA, 880 mA and 4.7 A respectively. This Result is obtained by F. Yazdi, M. Othman, and M. Veysi. 40

Fig. 2.10 (a) Comparison of the gain-bandwidth product (G×BW) of TWT amplifiers based on SWS regimes based on ideal SIP and tilted-positive dispersion, versus electron beam current I_0. Results are also compared with a TWT made of a SWS with only one periodic TL (single mode TWT) having the same length and average characteristic impedance. (b) Bandwidth comparison for the three aforementioned regimes of operation versus power gain (in dB). (c) Power added efficiency (PAE) in percentage for the three regimes as a function of power gain (in dB). In (b) and (c), different beam currents are chosen for the three regimes such that all three cases have equal gains. In all cases we are assuming a SWS made of *N* = 16 unit cells and the per unit length resistance of R_{loss} = 5 Ω/m with Z_{Li} = 75Ω, *i* = 1, 2, 3, Z_{s1} = 75Ω and open circuit at the two other input ports for the two SIP regimes, and $Z_L = Z_s$ = 75Ω for the single TL regime. This Result is obtained by F. Yazdi, M. Othman, and M. Veysi. 41

Fig. 3.1 (a) An example of the dispersion relation of an infinitely long periodic structure with three CTLs exhibiting third order modal degeneracy at angular frequency ω_e and the

coalescence of the modes at the exceptional point of degeneracy where all three modes coalesce at the same point with $k = k_e$. (b) Proposed 3-way periodic microstrip structure featuring a third order EPD. The structure can be viewed as two transmission lines coupled through a third serpentine transmission line. The 3-way periodic structure supports three modes in each longitudinal direction; hence, it can be made to exhibit an EPD by properly designing and tuning the dimensions and values of the parameters. 60

Fig. 3.2 Unit cell of the 3-way periodic microstrip structure that exhibits a third order degeneracy for Case *A* (used also in Secs. 3.3 and 3.4). The structure is composed of two uniform transmission lines coupled through a third serpentine transmission line in the middle, and two shunt conductances, gain and passive (e.g., a radiation resistance) added to the uncoupled sections with real positive and negative values as shown. (b) Unit cell of an alternative design (Case *B* and Case *C*) of the 3-way periodic microstrip structure where the shunt conductances (gain and loss) are added to the coupled sections instead. 62

Fig. 3.3 (a) Case *A*: complex wavenumber plotted in the complex k plane varying frequency. This plot shows the existence of the third order modal degeneracy condition and coalescence of the three modes at two different EPD wavenumbers, k_e and $-k_e + 2\pi/d$. (b) Coalescence parameter plotted versus normalized frequency in the vicinity of the EPD. (c) and (d) Typical modal dispersion diagram of the eigenmodes, showing both the real and imaginary parts of the normalized complex Floquet–Bloch wavenumber k versus normalized angular frequency around the EPD frequency ω_e. The purely real branches of the dispersion diagram are shown in solid black. Dashed-line dispersion branches represent the modes with complex wavenumber, using the same colors as in (a). Besides the lumped elements, we

have assumed the structure to be lossless for all the graphs shown in this figure. This Result is obtained by T. Mealy and F. Yazdi. 68

Fig. 3.4 (a) Case *B*: complex wavenumber plotted in the complex k plane varying frequency. This plot shows the existence of the third order modal degeneracy condition and coalescence of the three modes at two different EPD wavenumbers, k_e and $-k_e + 2\pi/d$. (b) Coalescence parameter plotted versus normalized frequency in the vicinity of the EPD. (c) and (d) Typical modal dispersion diagram of the eigenmodes, showing both the real and imaginary parts of the normalized complex Floquet–Bloch wavenumber *k* versus normalized angular frequency around the EPD frequency ω_e. The purely real branches of the dispersion diagram are shown in solid black. The circles represent branches with two modes (curves). Dashed-line dispersion branches represent the modes with complex wavenumber, using the same colors as in (a). Besides the lumped elements, we have assumed the structure to be lossless for all the graphs shown in this figure. This Result is obtained by T. Mealy and R. Marosi. 69

Fig. 3.5 (a) Case *C*: complex wavenumber plotted in the complex k plane varying frequency. This plot shows the existence of the third order modal degeneracy condition and coalescence of the three modes at two different EPD wavenumbers, k_e and $-k_e + 2\pi/d$. (b) Coalescence parameter plotted versus normalized frequency in the vicinity of the EPD. (c) and (d) Typical modal dispersion diagram of the eigenmodes, showing both the real and imaginary parts of the normalized complex Floquet–Bloch wavenumber *k* versus normalized angular frequency around the EPD frequency ω_e. The purely real branches of the dispersion diagram are shown in solid black. Dashed-line dispersion branches represent the modes with complex wavenumber, using the same colors as in (a). Besides the lumped elements,

we have assumed the structure to be lossless for all the graphs shown in this figure. This Result is obtained by T. Mealy and R. Marosi. 70

Fig. 3.6 Engineering of the dispersion diagram to exhibit different group velocities (different slopes) around ideal EPD. (a) By tuning the value of the R (or G) elements for Case A where we observe a slightly positive slope for R = 5.27Ω and a slightly negative slope for R = 9.11Ω where the ideal case with zero slope has R = 7.15Ω. (b) By tuning the value of the h (serpentine height) for Case A where we observe a slightly positive slope for h = 4.748 mm and a slightly negative slope for h = 5.948 mm where the ideal case with zero slope has h = 5.948 mm. For all the graphs shown above only the purely real branches of the dispersion diagram are plotted and we have assumed the structure to be lossless. This result is obtained by F. Yazdi. 72

Fig. 3.7 (a) Graphical representation of how the signal/power propagates inside the periodic structure moving along $+z$ for three different cases of: (i) purely real (k_1), (ii) complex wavenumber with positive imaginary part (k_2), and (iii) complex wavenumber with negative imaginary part (k_3). The propagating, growing and decaying cases are shown as discussed (b) Power (in mW) over the three lines of the infinitely long periodic structure plotted versus z evaluated exactly at EPD frequency for the design of Case A for the EPD is in the region $0 < kd < \pi$. This plot exhibits how the power moves over the structure for any specific mode and for each line of the three-way waveguide. (c) Summation of the powers (in mW) of the three lines shown in part (b) plotted versus z for the infinitely long periodic circuit. The jumps in the power are associated to the $+G$ and $-G$ contributions. This Result is obtained by F. Yazdi and T. Mealy. 75

Fig. 3.8 (a) Finite-length three-way structure with period d made by cascading the unit cells treated as a 6-port network that models wave propagation in the waveguide discussed in Section II with the total length of $L = Nd$, including loading and excitation. (b) $|S_{11}|$ and (c) $|S_{21}|$ for the finite length structure of Case *A* with $N = 8$ unit cells and $\tan(\delta)=0$ plotted versus frequency around EPD frequency, where we could achieve $|S_{11}|<1$ and the stability is confirmed. (d) The radiation gain and loads gain (both linear scale) versus the length of the finite structure (N) evaluated at the peak frequency nearest to the EPD for the finite structure of Case *A* with $\tan(\delta)=0$. For all results shown above we have assumed $Zy = Zs = Z_L = 50\Omega$ for the bottom and middle lines, and short circuit for the top lines ($Z_x = 0\ \Omega$). This result is obtained by A. Nikzamir and F. Yazdi. 77

Fig. 4.1 Two topologies of an FPC (a) PhC exhibiting RBE with alternative layers having refractive indices $n_1 = 1.5$ and $n_2 = 2.25$. (b) PhC exhibiting DBE composed of three layers, one isotopic with $n = 1.5$ and two anisotropic with misalignment angle of 45^o. 88

Fig. 4.2 Real parts of the k-ω dispersion relations where k is the Bloch complex wavenumber, for two photonic crystals (PhCs): one only exhibiting RBE and the other featuring also a DBE. 89

Fig. 4.3 A unit cell with length of d consisting three layers that can support DBE and relative electric permittivity tensor of $\boldsymbol{\varepsilon}(z)$. 95

Fig. 4.4 Periodic structure consisting of N unit cells featuring DBE. 97

Fig. 4.5 Magnitude of the transmission (a) and reflection (b) coefficients versus radian frequency for FPC formed by a periodic structure that exhibit a DBE at ω_d for four different polarizations ($N = 32$). (c-d) Zoomed region near the DBE radian frequency ω_d. This result is obtained by M. Othman and F. Yazdi. 101

Fig. 4.6 (a) Phase of the transmission coefficients, (b) Zoomed in version of the phase transition near the DBE for different polarizations (N = 32). This result is obtained by M. Othman. 102

Fig. 4.7 Wigner time for FPC formed by a periodic structure with N = 32 that exhibit a DBE at ω_d for four different polarizations. This result is obtained by M. Othman and F. Yazdi. 103

Fig. 4.8 Sampled local density of states (LDOS) normalized by the LDOS in free space inside FPC with DBE sampled at points $z = md$, m = 0, 1, 2, …, N with N = 32 for two polarizations. This result is obtained by M. Othman. 104

Fig. 5.1 (a) Unit cell of a periodic triple-ladder lumped circuit comprised of reactive lumped elements that develops a sixth order degeneracy at an angular frequency $\omega_h = 1/\sqrt{LC}$ (b) Dispersion diagram of the infinitely long periodic triple-ladder circuit exhibiting a 6DBE at angular frequency ω_h. The fitting curve shows analytically the flatness of the dispersion around the 6DBE. The 6DBE is flatter than the DBE and RBE. The result is obtained by F. Yazdi in Matlab. 116

Fig. 5.2 Complex dispersion relation of the infinite periodic circuit based on Puiseux series approximation (shown in solid red) in comparison with exact numerical dispersion relation (shown in solid blue) for the lossless circuit. The propagation phase angle φ is a generally complex number, both the real and imaginary parts are shown. The result is obtained by F. Yazdi in Matlab. 122

Fig. 5.3 (a) Triple ladder and (b) double ladder periodic LC circuits with finite length made of N unit cells with excitation voltage V_s, source resistance of $R_s = 50\Omega$, and load resistance of R_L at the second (middle) ladder. 123

Fig. 5.4 The voltage transfer function TF_2 of the circuit shown in Fig. 5.3 for (a) different number of unit cells and no loss in the elements and (b) different quality factors for elements in an $N = 8$ unit cells resonator. The important resonance is the one closest to ω_h, denoted as $\omega_{r,h}$. The Matlab result are obtained by F. Yazdi and A. Nikzamir. 125

Fig. 5.5 Loaded quality factor, Q_{tot}, versus element quality factor for different number of unit cells (N) (b) Loaded quality factor, Q_{tot}, versus the number of unit cells, N, for different elements' quality factors. The results are obtained by A. Nikzamir and F. Yazdi. 128

Fig. 6.1 (a) Periodic "three-way" waveguide, made of three coupled microstrip lines, that exhibits a sixth order DBE. The grounded substrate has a dielectric constant of 3 and the stubs are short circuited at their end. (b) Wavenumber-frequency dispersion diagram of the six Floquet-Bloch eigenmodes in the periodic three-way waveguide showing the 6DBE frequency at f_d = 2.95 GHz, where six dispersion curves coalesce at the single point with wavenumber $kd = \pi/d$. Branches that represent two modes are denoted by a dashed blue circle. When losses are considered, the dispersion diagram is modified and shown later in Fig. 6.3. The ADS results are obtained by T. Mealy and F. Yazdi. 139

Fig. 6.2 (a) A resonance cavity formed by connecting 8 unit cells. The left and right terminations are shorted to the ground except for the middle line at the left end of the structure. We have applied a phasor voltage of 1 V as input to the resonator. (b) Frequency response of the voltage at the middle of the structure where a peak is observed at the frequency close to the 6DBE frequency. (c) Voltage profile across the structure at the 6DBE resonance frequency showing the voltage distribution at each period of the three TLs. This result is obtained by T. Mealy and A. Nikzamir. 144

Fig. 6.3 (a) Fabricated unit cell of the proposed periodic three-way waveguide implemented in microstrip technology. (b) Bloch wavenumbers dispersion based on measurement (red dots) versus the one obtained via Method of Moments full-wave electromagnetic simulation (solid black). Both measurement and simulation are based on a six-port evaluation of the scattering parameters of the unit cell. Six modes coalescing are clearly visible, though the coalescence is not perfect because of losses and manufacturing imperfections. (c) Coalescence factor, D_H in linear scale versus frequency around the 6DBE, as a measure of closeness to the 6DBE, for the full-wave simulation results, in comparison to the measured results. (d) Tunability of 6DBE showing dispersion diagrams obtained from full-wave simulation of unit cell in Fig. 6.1(a) (black) and same unit cell after adding 1mm extension of transmission line at each port (period is extended by 2mm). The comparison shows that 6DBE frequency is very sensitive to any added extra length. Simulation results are done by T. Mealy, A. Nikzamir, and F. Yazdi, and measurements are done by D. Oshmarin and A. Almutawa. 146

Vita

Farshad Yazdi

2021 Ph.D. in Electrical and Computer Engineering, University of California, Irvine

2015 M.Sc. in Electrical and Computer Engineering, University of California, Irvine

2009 B.S in Electrical Engineering-Telecommunications, University of Tehran, Iran

EXPERIENCE

2013-2021 Graduate Student Researcher, Electrical Engineering and Computer Science, University of California, Irvine, Advisor: Prof. Filippo Capolino

2013-2021 Teaching Assistant, Electrical Engineering and Computer Science, University of California, Irvine

2009-2012 Teaching Assistant, Electrical Engineering, University of Tehran, Iran

FIELD OF STUDY

Analysis and Design of Passive and Active Devices with Coupled Modes Featuring Exceptional Points of Degeneracy. Gain and Density of States Enhancement in Photonic Crystals with a Degenerate Band Edge. Perturbation Analysis of Periodic Structures with Small Losses and Gain. Novel Oscillator/Amplifier Designs Based on Exceptional Points of Degeneracy of Periodic Systems.

PUBLICATIONS

[1] **F. Yazdi**, M. A. K. Othman, M. Veysi, A. Figotin, and F. Capolino, "A New Amplification Regime for Traveling Wave Tubes with Third Order Modal Degeneracy," *IEEE Trans. on Plasma Science*, Vol. 46, No.1, pp. 43-56, Jan. 2018, doi: 10.1109/TPS.2017.2781245.

[2] **F. Yazdi**, D. Oshmarin, A. T. Almutawa, and F. Capolino, "Experimental Demonstration of Sixth Order Degenerate Band Edge in Coupled Microstrip Waveguides," *ArXiv190603331 Phys.*, Jun. 2019, Accessed: May 04, 2021. [Online]. Available at: http://arxiv.org/abs/1906.03331.

[3] M. A. K. Othman, **F. Yazdi**, A. Figotin and F. Capolino, "Giant gain enhancement in photonic crystals with a degenerate band edge," *Phys Rev. B*, Vol. 93, 024301, 2016, doi: https://doi.org/10.1103/PhysRevB.93.024301.

[4] Dmitry Oshmarin, **Farshad Yazdi**, Mohamed AK Othman, Jeff Sloan, Mohammad Radfar, Michael M Green, Filippo Capolino, "New oscillator concept based on band edge degeneracy in lumped double-ladder circuits," *IET Circuits, Devices & Systems*, vol. 13, no. 7, pp. 950–957, 2019, doi: 10.1049/iet-cds.2018.5048.

[5] **F. Yazdi**, M. A. K. Othman, M. Veysi, F. Capolino, and A. Figotin, "Third order modal degeneracy in waveguides: Features and application in amplifiers," in *2017 USNC-URSI Radio Science Meeting (Joint with AP-S Symposium)*, Jul. 2017, pp. 109–110, doi: 10.1109/USNC-URSI.2017.8074921.

[6] M. A. K. Othman, **F. Yazdi**, and F. Capolino, "Exceptional points of degeneracy in coupled-mode periodic structures," in *2016 URSI International Symposium on Electromagnetic Theory (EMTS)*, Aug. 2016, pp. 38–41, doi: 10.1109/URSI-EMTS.2016.7571305.

[7] M. Y. Nada, T. Mealy, **F. Yazdi**, A. F. Abdelshafy, A. Figotin, and F. Capolino, "General Conditions to Realize Exceptional Points of Degeneracy and Applications," in *2018 12th International Congress on Artificial Materials for Novel Wave Phenomena (Metamaterials)*, Aug. 2018, pp. 287–289.

ABSTRACT OF THE DISSERTATION

Analysis and Design of Passive and Active Transmission Lines with Coupled Modes with Exceptional Points of Degeneracy

By

Farshad Yazdi

Doctor of Philosophy in Electrical and Computer Engineering

University of California, Irvine, 2021

Professor Filippo Capolino, Chair

Periodic structures have been utilized in many novel active devices due to their unique properties such as the presence of electromagnetic band-edges and band-gaps. Dispersion diagrams are associated to such structures with a unit cell repeated periodically and show the relation between frequency and periodic state phase shift or the eigen-states of the system. The dispersion characteristics of periodic structures can be engineered to exhibit exceptional modal characteristics, which can be exploited to design novel devices with improved features and enhanced performance. Distinct sorts of degeneracy may exist in periodic schemes where the eigen-states of the system coalesce and form a single degenerate periodic eigen-state. These phenomena can be classified as exceptional points of degeneracy (EPD) and is shown to have some fascinating features which make them desirable for a wide variety of applications including oscillators, amplifiers, lasers, and pulse compressors which are widely used in IoT scenarios.

A special and well-known category of degeneracies in periodic structures is recognized as the fourth order degenerate band edge (DBE) where four periodic eigenstates coincide at the edge of the Brillouin zone. In this work we put the focus on two other significant types of

EPDs which are the stationary inflection point (SIP, with third order degeneracy) and the sixth order degenerate band edge (6DBE). In particular, the 6DBE characteristics are expected to be noteworthy in enhancement of the Q-factor and in lowering the oscillation threshold in finite length resonators with gain compared to conventional uniform or homogeneous structures. Furthermore, a novel amplification regime based on special dispersion characteristics of an SIP, also called "frozen mode regime", is proposed leading to a higher gain and larger gain-bandwidth product compared to conventional Pierce-type traveling wave tubes. Moreover, a novel design of a periodically coupled three-way microstrip waveguide is presented utilizing PT-glide symmetry by proper balancing of the loss/gain featuring third order EPDs. This latter concept could be advantageous in diverse applications including but not limited to distributed amplifiers and radiating arrays of antennas.

The first physical realization and experimental demonstration of an exceptional point of sixth order (6DBE) in a triple ladder (three-way) microwave waveguide is provided; the unique properties of the 6DBE may be exploited in designing innovative high-Q resonators, oscillators, filters, and pulse shaping devices.

An in-depth investigation of the modes and dispersion relations based on the state vectors and transfer matrix formalism is offered where we have also provided the analytical framework for the Puiseux fractional power series expansion of the system's eigenvalues around the degeneracy condition that will be used to approximate the dispersion relation, local density of states (LDOS), and other important parameters. The analytical framework and physical concepts established in this thesis may be applied to a variety of structure designs and applications featuring degeneracy conditions of different orders and can be a useful tool in designing and evaluating novel passive and active devices.

CHAPTER 1

INTRODUCTION

Sec. 1.1 The Concept of Exceptional Points of Degeneracy

This dissertation is based on the concept of exceptional points of degeneracy (EPDs) developed over the course of electromagnetics engineering in a quest to propose and evaluate novel designs for passive and active devices with improved characteristics. We will investigate the theory, properties, and applications of the exceptional points of degeneracy in periodic coupled structures with the focus to make better active/passive devices.

Periodic structures (e.g. circuits, transmission lines, and microstrips) have been utilized in many electromagnetic devices due to their unique properties such as the presence of electromagnetic band-edges and band-gaps. Dispersion diagrams are associated to such structures with a unit cell repeated periodically and show the relation between frequency and periodic state phase shift or the eigen-states (represented by k also known as the Bloch wavenumber in literature) of the system. The dispersion characteristics of periodic structures can be engineered (by varying and tuning the frequency and physical/design parameters of waveguiding structure) to exhibit exceptional modal characteristics, which

can be exploited to propose innovative devices with enhanced features and boosted performance for a wide variety of applications.

Degeneracy in electromagnetic waveguides means that independent eigenmodes or eigenstates of the system defining the transfer characteristics of the periodic structure coalesce into one single eigenstate at a certain angular frequency, denoted by ω_e, and form a single degenerate mode. These special phenomena in the parameter space of the waveguide is known as exceptional point of degeneracy (EPD) in the literature [1]–[3]. Distinct sorts of degeneracy may exist in periodic schemes having different orders. In Fig. 1.1 a few important EPDs of different orders is demonstrated. Mathematically, this special degeneracy is manifested when the system matrix describing the propagation is defective and a complete basis of eigenvectors cannot be obtained [1], [4]. Degeneracies of eigenmodes in periodic structures were first investigated by Figotin and Vitebskiy in [5]–[10], demonstrating the existence of unique features associated with modal degeneracies. The EPDs associated to the coalescence of the modes is a relatively recent concept in the study of active devices.

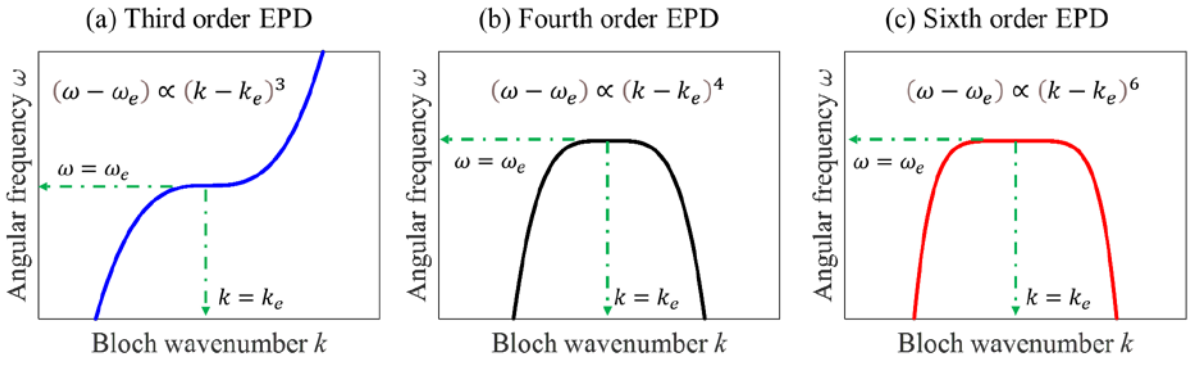

Fig. 1.1 Dispersion relations of arbitrary periodic structures exhibiting EPDs with different orders of modal degeneracy at angular frequency ω_e and the coalescence of the modes at the same point with $k = k_e$ with: (a) Third order EPD (b) Fourth order EPD (c) Sixth order EPD.

The effect of perturbations introduced to the system such as frequency and loss will result in deviation from the ideal degeneracy condition. As a matter of fact, the degeneracy condition is very sensitive to disorders. In this thesis an in-depth investigation of the modes and dispersion relations based on the state vectors and transfer matrix formalism is offered where we have also provided the analytical framework for the Puiseux fractional power series expansion of the system's eigenvalues around the degeneracy condition that will be used to approximate the dispersion relation, density of states (DOS), and other important parameters in the presence of perturbations. The analytical framework established in this thesis may be applied to a variety of structure designs and applications featuring degeneracy conditions of different orders and will be a useful tool in designing and evaluating novel active device designs.

Sec. 1.2 Degenerate Band Edge (DBE)

A special and well-known category of degeneracies in periodic structures is recognized as the fourth order degenerate band edge (DBE) where four periodic eigenstates coincide at the center or edge of the Brillouin zone [11]–[15]. Such unique band edge condition is associated with many slow light properties such as enhancement of local density of states, and enhancement of gain in active devices comprising DBE structures. The existence and characteristics of the fourth order DBE has been exhibited in various periodic structures including transmission lines and striplines [15]–[17], as well as metallic [18] and optical waveguides [19]–[22]. A very promising way to further enhance the quality and Purcell factors of resonators for laser applications is by utilizing the special band edge condition associated to the DBE of the structural eigenmodes of a PhC [23] and [24]. We demonstrate

in this thesis that a Fabry-Perot cavity (FPC) composed of repeating a cascade of unit cells capable of supporting a DBE, allows substantial enhancement in group delay (or Winger time) and local density of states for laser applications. We also provide analytical results that provide insight into the design of photonic crystal lasers utilizing the DBE.

In [25] a double ladder periodic lumped circuit is introduced to exhibit a DBE, explaining also the advantages associated to it such as high quality factor and stability to load changes. These properties have been found useful in conceiving new regimes of oscillation where a new oscillator concept is proposed in [26] based on DBE condition which will lead to lower oscillation threshold and more robustness to the effects of loss and loading as opposed to devices featuring only regular band edge [14], [27] based on the enhanced quality factor associated to the DBE condition.

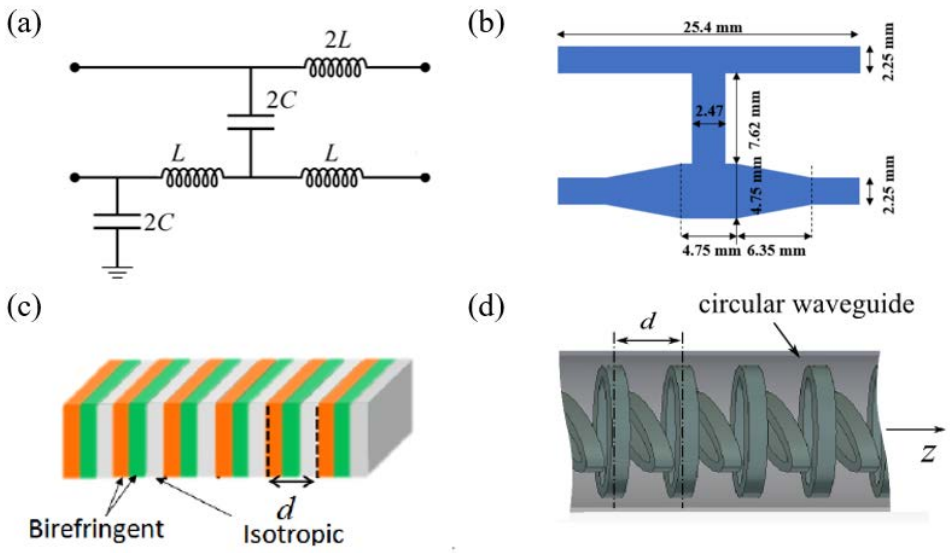

Fig. 1.2 Example geometries of different periodic structures potentially supporting DBE condition: (a) lumped double ladder circuit [25] (b) printed microstrip lines [15] (c) photonic crystal [14] (d) circular metallic waveguide [28].

Sec. 1.3 Third Order EPD (SIP)

The third order degeneracy typically referred to as the stationary inflection points (SIP) is a degeneracy condition associated to the coalescence of three Floquet-Bloch eigenmodes in the periodic structure [5], [29]–[31] that cause an inflection point in the dispersion diagram and has potential to demonstrate unique features compared to conventional devices [32]. In the vicinity of third-order EPDs in the $\omega - k$ dispersion relation we observe that $(\omega - \omega_e) \propto (k - k_e)^3$, where ω_e is the angular frequency at which three modes coalesce and k_e is the Bloch wavenumber at the degeneracy point (note that $k_e \neq \pi/d$, meaning that the EPD does not occur at the band edge of the Brillouin zone). An illustration of an ideal dispersion relation exhibiting a third order EPD is shown in Fig. 1.1 (a) for a normalized case in which the real branches of an $\omega - k$ dispersion diagram (where k is the Bloch-wavenumber and ω is the angular frequency) is plotted and the coalescence of the modes is shown. It should also be noted that by tuning the parameters of a periodic coupled structure one can achieve an SIP with nearly ideal flat dispersion relationship with zero group velocity or a slightly slanted one with a very small (positive or negative) group velocity leading to different operating schemes.

Specifically, a novel amplification regime based on special dispersion characteristics of SIP is proposed in this thesis leading to a higher gain and larger gain-bandwidth product compared to a conventional Pierce-type TWTs where we demonstrate (1) a significant gain enhancement of the proposed TWT with SIP in comparison to a periodic single mode Pierce one (orders of magnitude higher gain for same length and/or same DC power supplied), and (2) substantial gain-bandwidth product improvement for SIP schemes as well as (3)

significantly higher power efficiency (especially for high power gain values) compared to a single mode Pierce TWT modeled with one transmission line.

Furthermore, the novel design of a periodic coupled three-way microstrip device is presented utilizing *PT*-glide symmetry by proper balancing of the loss/gain featuring third order EPDs that has diverse applications including but not limited to distributed amplifiers and radiating arrays.

Sec. 1.4 Sixth Order EPD (6DBE)

The sixth order degenerate band edge (6DBE) is a particular degeneracy condition that happens when six Floquet-Bloch modes (eigenstates) coalesce at the edge of the Brillouin zone. At this condition the dispersion relation around the degeneracy point is approximated by $(\omega - \omega_e) \propto (k - k_e)^6$, in which k_e is the Bloch wavenumber at the degeneracy point and ω_e is the frequency that features the sixth order degeneracy. We have presented in this thesis a new resonator concept made by cascading unit cells of a simple triple-ladder circuit periodically that leads to a degeneracy of order sixth (6DBE) in its phase-frequency dispersion relation. The proposed design exploits the fascinating features and enhancements of higher order degeneracies over previously introduced designs with double ladder (exhibiting DBE) and single ladder (exhibiting only RBE) circuits particularly in terms of Q-factor and sensitivity to perturbations.

A physical realization of a novel three-way periodic waveguide exhibiting a sixth-order degeneracy (6DBE) is also demonstrated for the first time using microstrip technology. Both theoretical and experimental verifications are provided. Remarkable physical properties may arise due to this sixth-order exceptional point of degeneracy including increased quality

factor, high density of states, and sensitivity which can lead to novel designs for microwave and optical pulse generation [33], microwave and millimeter wave oscillators [34]–[36], low-threshold lasers [37], [38], short delay lines with significant group delay, filters, and ultra-sensitive sensors.

Sec. 1.5 Content of Each Chapter

The dissertation is organized into chapters that include the design and analysis of various periodic topologies and structures featuring modal degeneracies of different orders and their novel applications from amplifiers and oscillators to sensors and filters.

Chapter 2: Engineering of the eigenmode dispersion of slow-wave structures (SWSs) to achieve desired modal characteristics, is an effective approach to enhance the performance of high-power traveling wave tube (TWT) amplifiers or oscillators. In this chapter, we investigate for the first time a new synchronization regime in TWTs based on SWSs operating near a third order degeneracy condition in their dispersion relation. This special three-eigenmode synchronization is associated with a stationary inflection point (SIP) that is manifested by the coalescence of three Floquet-Bloch eigenmodes in the SWS. We demonstrate the special features of "cold" (without electron beam) periodic SWSs with SIP modeled as coupled transmission lines (CTLs) and investigate resonances of SWSs of finite length. We also show that by tuning the parameters of a periodic SWS one can achieve an SIP with nearly ideal flat dispersion relationship with zero group velocity or a slightly slanted one with a very small (positive or negative) group velocity leading to different operating schemes. When the SIP structure is synchronized with the electron beam potential benefits for amplification include (i) gain enhancement, (ii) gain-bandwidth product improvement,

and (iii) higher power efficiency, when compared to conventional Pierce-like TWTs. The proposed theory in this chapter paves the way for a new approach for potential improvements in gain, power efficiency and gain-bandwidth product in high power microwave amplifiers.

Chapter 3: The dispersion characteristics of microstrip structures can be engineered to exhibit exceptional modal characteristics, which can be exploited to design novel devices with improved features and enhanced performance for a wide variety of applications. Two coupled waveguides with *PT*-symmetry were known to exhibit second order exceptional point of degeneracy (EPD). In this work we introduce and investigate a particular class of EPD whereby three coupled waveguides satisfy *PT*-glide symmetry to exhibit a third order degeneracy condition in the dispersion relation of the periodic structure comprised of three-way microstrip coupled transmission lines (3CTLs) with periodically-spaced lumped elements to achieve loss/gain in a *PT*-glide symmetric manner, causing three Floquet–Bloch eigenmodes to coalesce under certain conditions. We show for the first time the novel design of such three-way microstrip device utilizing *PT*-glide symmetry and investigate the remarkable characteristics of the designs featuring third order EPDs. The proposed scheme may have diverse applications including but not limited to distributed amplifiers, radiating arrays, and sensors.

Chapter 4: The main goal of this chapter is to report that slow-wave resonance associated with a degenerate band edge (DBE) in the dispersion diagram of photonic crystals can substantially increase the local density of states (DOS) and Wigner time in a Fabry-Perot cavity (FPC). The enormous enhancement of the local density of states and therefore the density of states (DOS) at frequencies close to the DBE can be interpreted as a giant gain

enhancement in the FPC. We provide analytic steps and calculations in order to find the transfer matrix and complex transmission coefficients of an *N*-period, one-dimensional structure made by stacking anisotropic tri-layers, to be able to exhibit DBE characteristics, in the simplest form possible. These findings then will be used to calculate Wigner time and LDOS of the cavity under investigation. The asymptotic analysis provides valuable insight into this new scheme operating at the degenerate band edge condition of photonic crystals.

Chapter 5: We introduce a circuit topology based on a simple triple-ladder circuit realized with lumped reactive components that provides a sixth order degenerate band-edge (6DBE). The 6DBE is a special kind of sixth order exceptional point of degeneracy in a lossless and gainless ladder. This degeneracy provides a very flat band edge in the phase – frequency dispersion diagram. The proposed topology exhibits unique structured resonance features associated with a high loaded *Q*-factor. We investigate the Floquet-Bloch modes, and dispersion relation of an infinite length periodic triple-ladder using the transfer matrix formalism and we also provide the analytic approximate expressions of the eigenmodes and dispersion relation around the degenerate point based on Puiseux series expansion. We also investigate the filtering characteristics of a finite structure terminated with loads to highlight the extraordinary properties of the 6DBE compared to the regular band edge (RBE) and the fourth order degenerate band edge (DBE). The circuit framework introduced here with a 6DBE can be exploited in designing novel high *Q*-factor oscillators, filters, and pulse shaping networks.

Chapter 6: In this chapter we show the first physical realization and experimental demonstration of an exceptional point of 6^{th} order in a triple ladder (or three-way) microwave waveguide realized using three coupled microstrips on a grounded dielectric

substrate. This three-way waveguide supports six Bloch eigenmodes and all coalesce onto a degenerate single eigenmode at a given frequency. The three-way waveguide is gainless, and this exceptional point is associated to a vanishing group velocity and its multiple derivatives. Indeed the $\omega - k$ dispersion diagram has six coalescing branches that we call the 6^{th} order degenerate band edge (6DBE). We provide the first experimental verification of this kind of 6^{th} order exceptional point by reconstructing the degenerate wavenumber-frequency dispersion diagram from the measurement of scattering parameters of a six-port unit cell, and also by observing the coalescence of the six system's eigenvectors obtained from measurements. The unique properties of 6DBE can be exploited in designing innovative high-Q resonators, oscillators, filters, and pulse shaping devices.

References

[1] T. Kato, *Perturbation theory for linear operators*. Verlag, NY: Springer Science & Business Media, 2013.

[2] W. D. Heiss, "Exceptional points of non-Hermitian operators," *J. Phys. Math. Gen.*, vol. 37, no. 6, pp. 2455–2464, Jan. 2004, doi: 10.1088/0305-4470/37/6/034.

[3] W. D. Heiss, "The physics of exceptional points," *J. Phys. Math. Theor.*, vol. 45, no. 44, p. 444016, Oct. 2012, doi: 10.1088/1751-8113/45/44/444016.

[4] N. Dunford, J. T. Schwartz, W. G. Bade, and R. G. Bartle, *Linear operators*. New York: Wiley intersciense, 1958.

[5] A. Figotin and I. Vitebskiy, "Electromagnetic unidirectionality in magnetic photonic crystals," *Phys. Rev. B*, vol. 67, no. 16, p. 165210, 2003.

[6] A. Figotin and I. Vitebskiy, "Gigantic transmission band-edge resonance in periodic stacks of anisotropic layers," *Phys. Rev. E*, vol. 72, no. 3, p. 036619, Sep. 2005, doi: 10.1103/PhysRevE.72.036619.

[7] A. Figotin and I. Vitebskiy, "Frozen light in photonic crystals with degenerate band edge," *Phys. Rev. E*, vol. 74, no. 6, p. 066613, Dec. 2006, doi: 10.1103/PhysRevE.74.066613.

[8] A. Figotin and I. Vitebskiy, "Slow-wave resonance in periodic stacks of anisotropic layers," *Phys. Rev. A*, vol. 76, no. 5, p. 053839, Nov. 2007, doi: 10.1103/PhysRevA.76.053839.

[9] A. Figotin and I. Vitebskiy, "Slow light in photonic crystals," *Waves Random Complex Media*, vol. 16, no. 3, pp. 293–382, 2006, doi: 10.1080/17455030600836507.

[10] A. Figotin and I. Vitebskiy, "Slow wave phenomena in photonic crystals," *Laser Photonics Rev.*, vol. 5, no. 2, pp. 201–213, Mar. 2011, doi: 10.1002/lpor.200900049.

[11] A. Figotin and I. Vitebskiy, "Slow light in photonic crystals," *Waves Random Complex Media*, vol. 16, no. 3, pp. 293–382, 2006.

[12] A. Figotin and I. Vitebskiy, "Slow wave phenomena in photonic crystals," *Laser Photonics Rev.*, vol. 5, no. 2, pp. 201–213, 2011.

[13] M. A. Othman and F. Capolino, "Demonstration of a degenerate band edge in periodically-loaded circular waveguides," *IEEE Microw. Wirel. Compon. Lett.*, vol. 25, no. 11, pp. 700–702, 2015.

[14] M. A. K. Othman, F. Yazdi, A. Figotin, and F. Capolino, "Giant gain enhancement in photonic crystals with a degenerate band edge," *Phys. Rev. B*, vol. 93, no. 2, p. 024301, Jan. 2016, doi: 10.1103/PhysRevB.93.024301.

[15] A. F. Abdelshafy, M. A. K. Othman, D. Oshmarin, A. T. Almutawa, and F. Capolino, "Exceptional Points of Degeneracy in Periodic Coupled Waveguides and the Interplay of Gain and Radiation Loss: Theoretical and Experimental Demonstration," *IEEE Trans. Antennas Propag.*, vol. 67, no. 11, pp. 6909–6923, Nov. 2019, doi: 10.1109/TAP.2019.2922778.

[16] C. Löcker, K. Sertel, and J. L. Volakis, "Emulation of propagation in layered anisotropic media with equivalent coupled microstrip lines," *Microw. Wirel. Compon. Lett. IEEE*, vol. 16, no. 12, pp. 642–644, 2006.

[17] J. L. Volakis and K. Sertel, "Narrowband and Wideband Metamaterial Antennas Based on Degenerate Band Edge and Magnetic Photonic Crystals," *Proc. IEEE*, vol. 99, no. 10, pp. 1732–1745, Oct. 2011, doi: 10.1109/JPROC.2011.2115230.

[18] M. A. K. Othman, X. Pan, G. Atmatzakis, C. G. Christodoulou, and F. Capolino, "Experimental Demonstration of Degenerate Band Edge in Metallic Periodically Loaded Circular Waveguide," *IEEE Trans. Microw. Theory Tech.*, vol. 65, no. 11, pp. 4037–4045, Nov. 2017, doi: 10.1109/TMTT.2017.2706271.

[19] N. Gutman, C. Martijn de Sterke, A. A. Sukhorukov, and L. C. Botten, "Slow and frozen light in optical waveguides with multiple gratings: Degenerate band edges and stationary inflection points," *Phys. Rev. A*, vol. 85, no. 3, Mar. 2012, doi: 10.1103/PhysRevA.85.033804.

[20] M. G. Wood, J. R. Burr, and R. M. Reano, "Degenerate band edge resonances in periodic silicon ridge waveguides," *Opt. Lett.*, vol. 40, no. 11, pp. 2493–2496, 2015.

[21] M. Y. Nada, M. A. K. Othman, and F. Capolino, "Theory of coupled resonator optical waveguides exhibiting high-order exceptional points of degeneracy," *Phys. Rev. B*, vol. 96, no. 18, p. 184304, Nov. 2017, doi: 10.1103/PhysRevB.96.184304.

[22] M. Y. Nada, M. A. K. Othman, O. Boyraz, and F. Capolino, "Giant Resonance and Anomalous Quality Factor Scaling in Degenerate Band Edge Coupled Resonator Optical Waveguides," *J. Light. Technol.*, vol. 36, no. 14, pp. 3030–3039, Jul. 2018, doi: 10.1109/JLT.2018.2822600.

[23] J. Ballato, A. Ballato, A. Figotin, and I. Vitebskiy, "Frozen light in periodic stacks of anisotropic layers," *Phys. Rev. E Stat. Nonlin. Soft Matter Phys.*, vol. 71, no. 3 Pt 2B, p. 036612, Mar. 2005, doi: 10.1103/PhysRevE.71.036612.

[24] A. Figotin and I. Vitebskiy, "Frozen light in photonic crystals with degenerate band edge," *Phys. Rev. E Stat. Nonlin. Soft Matter Phys.*, vol. 74, no. 6 Pt 2, p. 066613, Dec. 2006, doi: 10.1103/PhysRevE.74.066613.

[25] J. T. Sloan, M. A. K. Othman, and F. Capolino, "Theory of Double Ladder Lumped Circuits With Degenerate Band Edge," *IEEE Trans. Circuits Syst. Regul. Pap.*, vol. 65, no. 1, pp. 3–13, Jan. 2018, doi: 10.1109/TCSI.2017.2690971.

[26] D. Oshmarin *et al.*, "New oscillator concept based on band edge degeneracy in lumped double-ladder circuits," *IET Circuits Devices Syst.*, vol. 13, no. 7, pp. 950–957, 2019, doi: https://doi.org/10.1049/iet-cds.2018.5048.

[27] J. P. Dowling, M. Scalora, M. J. Bloemer, and C. M. Bowden, "The photonic band edge laser: A new approach to gain enhancement," *J. Appl. Phys.*, vol. 75, no. 4, pp. 1896–1899, Feb. 1994, doi: 10.1063/1.356336.

[28] M. A. K. Othman, M. Veysi, A. Figotin, and F. Capolino, "Giant amplification in degenerate band edge slow-wave structures interacting with an electron beam," *Phys. Plasmas*, vol. 23, no. 3, p. 033112, Mar. 2016, doi: 10.1063/1.4942791.

[29] M. B. Stephanson, K. Sertel, and J. L. Volakis, "Frozen Modes in Coupled Microstrip Lines Printed on Ferromagnetic Substrates," *IEEE Microw. Wirel. Compon. Lett.*, vol. 18, no. 5, pp. 305–307, May 2008, doi: 10.1109/LMWC.2008.922107.

[30] N. Apaydin, L. Zhang, K. Sertel, and J. L. Volakis, "Experimental Validation of Frozen Modes Guided on Printed Coupled Transmission Lines," *IEEE Trans. Microw. Theory Tech.*, vol. 60, no. 6, pp. 1513–1519, Jun. 2012, doi: 10.1109/TMTT.2012.2192746.

[31] H. Ramezani, S. Kalish, I. Vitebskiy, and T. Kottos, "Unidirectional Lasing Emerging from Frozen Light in Nonreciprocal Cavities," *Phys. Rev. Lett.*, vol. 112, no. 4, p. 043904, 2014.

[32] F. Yazdi, M. A. K. Othman, M. Veysi, A. Figotin, and F. Capolino, "A New Amplification Regime for Traveling Wave Tubes With Third-Order Modal Degeneracy," *IEEE Trans. Plasma Sci.*, vol. 46, pp. 43–56, Jan. 2018, doi: 10.1109/TPS.2017.2781245.

[33] V. A. Tamma, A. Figotin, and F. Capolino, "Concept for Pulse Compression Device Using Structured Spatial Energy Distribution," *IEEE Trans. Microw. Theory Tech.*, vol. 64, no. 3, pp. 742–755, Mar. 2016, doi: 10.1109/TMTT.2016.2518160.

[34] D. Oshmarin *et al.*, "New oscillator concept based on band edge degeneracy in lumped double-ladder circuits," *IET Circuits, Devices & Systems*, vol. 13, no. 7, pp. 950–957, 2019, doi: https://doi.org/10.1049/iet-cds.2018.5048.

[35] M. Y. Nada *et al.*, "Microwave Circuits with Exceptional Points and Applications in Oscillators and Sensors," in *2018 18th Mediterranean Microwave Symposium (MMS)*, Oct. 2018, pp. 108–111. doi: 10.1109/MMS.2018.8611828.

[36] A. F. Abdelshafy, D. Oshmarin, M. A. K. Othman, M. M. Green, and F. Capolino, "Distributed Degenerate Band Edge Oscillator," *IEEE Trans. Antennas Propag.*, vol. 69, no. 3, pp. 1821–1824, Mar. 2021, doi: 10.1109/TAP.2020.3018539.

[37] M. Y. Nada and F. Capolino, "Exceptional point of sixth-order degeneracy in a modified coupled-resonator optical waveguide," *JOSA B*, vol. 37, no. 8, pp. 2319–2328, Aug. 2020, doi: 10.1364/JOSAB.385198.

[38] M. Veysi, M. A. K. Othman, A. Figotin, and F. Capolino, "Degenerate band edge laser," *Phys. Rev. B*, vol. 97, no. 19, p. 195107, May 2018, doi: 10.1103/PhysRevB.97.195107.

CHAPTER 2

A New Amplification Regime for Traveling Wave Tubes with Third Order Modal Degeneracy

Sec. 2.1 Motivation

Engineering of the eigenmode dispersion of slow-wave structures (SWSs) to achieve desired modal characteristics, is an effective approach to enhance the performance of high-power traveling wave tube (TWT) amplifiers or oscillators. In this chapter, we investigate for the first time a new synchronization regime in TWTs based on SWSs operating near a third order degeneracy condition in their dispersion relation. This special three-eigenmode synchronization is associated with a stationary inflection point (SIP) that is manifested by the coalescence of three Floquet-Bloch eigenmodes in the SWS. We demonstrate the special features of "cold" (without electron beam) periodic SWSs with SIP modeled as coupled transmission lines (CTLs) and investigate resonances of SWSs of finite length. We also show that by tuning the parameters of a periodic SWS one can achieve an SIP with nearly ideal flat dispersion relationship with zero group velocity or a slightly slanted one with a very small (positive or negative) group velocity leading to different operating schemes.

When the SIP structure is synchronized with the electron beam potential benefits for amplification include (i) gain enhancement, (ii) gain-bandwidth product improvement, and (iii) higher power efficiency, when compared to conventional Pierce-like TWTs. The proposed theory in this chapter paves the way for a new approach for potential improvements in gain, power efficiency and gain-bandwidth product in high power microwave amplifiers.

The classical approach for designing high power microwave amplifiers provides for an efficient energy transfer from high energy electron beams to electromagnetic fields at radio and microwave frequencies [1], [2]. A traveling wave tube (TWT) amplifier is a conventional high power device comprising of a slow-wave structure (SWS) whose interacting mode has a synchronous phase velocity to the average electron's velocity of the electron beam [1]–[4]. Pierce and his contemporaries [3], [5]–[8] developed a ubiquitous framework and design procedure for such devices through circuit theory. According to simple but physically incisive Pierce model [3], the amplification in a TWT is attributed to amplification of a slow wave radio frequency (RF) signal in an equivalent transmission line (TL) due to perturbation of the electron charge density thanks to bunching of the electron beam (the charge wave). Remarkably, Pierce predicted the small signal gain of a TWT and provided design rules for TWT amplifiers in terms of the SWS and electron beam parameters [2], [9]. In essence, state of the art of the high power TWT technology employs all-metallic slow-wave guiding structures whose dispersion is engineered for (i) matching phase velocity to an electron beam over a wide bandwidth; and (ii) high interaction impedance [10]–[17]. Consequently, dispersion engineering of the SWS eigenmodes would potentially enhance the gain, efficiency and bandwidth of conventional TWTs [18]–[22] and

backward wave oscillators (BWOs) [23]–[26]. We investigate here in this chapter a novel amplification regime based on special dispersion characteristics of SWS potentially leading to a higher gain and larger gain-bandwidth product (typical figure of merit for amplifiers) compared to a conventional Pierce-type TWT. In particular, the proposed regime of operation relies on electromagnetic eigenmode degeneracy in periodic SWS, namely, the third order degeneracy typically referred to as the stationary inflection points (SIP). The SIP condition is found when three Floquet-Bloch eigenmodes in the "cold" periodic structure coalesce [27]–[30] and cause an inflection point in the dispersion diagram. The "cold" term refers to a SWS which is not coupled to an electron beam. In [31]–[33], some of the authors have developed the theory of a SWS-electron beam interaction based on a different modal degeneracy, the degenerate band edge (DBE) [34]–[38], which inherently has limited bandwidth. The theory in [31]–[33], [39] describes four Floquet-Bloch eigenmodes synchronous scheme of oscillators operating with a fourth order degeneracy at the degenerate band edge (DBE).

In this premise, instead, we investigate amplification in TWTs operating near the SIP in their dispersion relation. Such operational principle is referred to as *three Floquet-Bloch eigenmode interaction* which promises special features which are not present in conventional single mode TWTs, or even in TWTs operating at the DBE. The main reason for these special features is that a SWS with SIP exploits three degenerate eigenmodes that (i) do not have negative group velocity, and (ii) have frequencies inside the band and are far from any *bandgap.* In contrast, an SWS based on the DBE exploits both positive and negative group velocity in the DBE neighborhood that has been proposed for a new regime of operation for low-threshold oscillators [33].

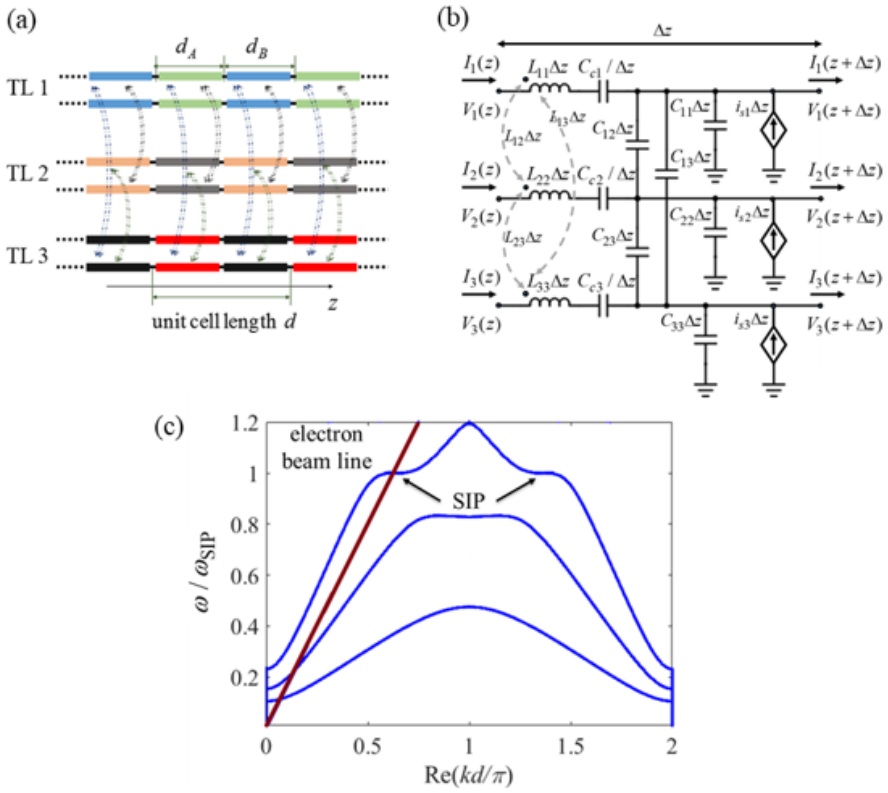

Fig. 2.1 (a) Schematic of a periodic CTLs consisting of three TLs that mimic a SWS supporting three coupled eigenmodes. The unit cell, of period d, is made of two segments (shown by different colors). Each segment is described using TLs distributed parameters. (b) Generalized Pierce model for the three CTL interacting with an electron beam. The dependent current sources are used in the generalized Pierce model to describe the interaction of the charge wave modulating the electron beam with the RF signal in the SWS. (c) Typical modal dispersion diagram, where only branches with purely real Floquet-Bloch wavenumbers are shown, of a periodic "cold" three CTLs (without including the beam interaction) having SIP at angular frequency ω_{SIP}. The beam line shows the charge wave velocity to be synchronized with the three RF modes in the TLs that is introduced in (2.2) and discussed in Sec. 2.4. Dispersion diagrams for the combined CTL-electron beam interactive system are shown in Sec. 2.4-*A* and Appendix A.

We demonstrate (i) a significant gain enhancement of the proposed TWT with SIP in comparison to a periodic single mode Pierce one (orders of magnitude higher gain for same length and/or same DC power supplied), and (ii) substantial gain-bandwidth product

improvement for SIP schemes as well as (iii) significantly higher power efficiency (especially for high power gain values) compared to a single mode Pierce TWT modeled with one transmission line.

The rest of the chapter is organized as follows: in Section 2.2 the background and the main idea to be developed is presented. In Section 2.3 the theory of waveguides with SIP in the dispersion diagram is summarize and the three, coupled transmission line (CTLs) model that is capable of exhibiting SIP [see Fig. 2.1(a) and (b)] is introduced. The engineering of the SIP to have slightly positive or slightly negative slope (i.e., group velocity) is also discussed. Then the finite-length SWS is considered where an inspection of the transfer functions, effects of loss and loading is provided. In Section 2.4, the unique interaction scheme of such SWS with SIP with the electron beam is investigated where the convective instability regime (i.e., amplification) is studied and the instabilities associated with oscillator is briefly discussed. Finally, the advantages of the proposed regime of amplification focusing on the three aforementioned properties (i)-(iii) is discussed. Throughout this chapter, I assume linear operation of the TWT and assume that the time-dependence is implicit in the form of $e^{j\omega t}$ and hence suppressed.

Sec. 2.2 Background and Problem Statement

We investigate the simultaneous synchronization of the charge wave modulating the electron beam with *three* Floquet-Bloch eigenmodes with positive phase velocity along the $+z$-direction of a periodic SWS near the SIP. The simultaneous beam-synchronization of three electromagnetic modes affects amplification of the electromagnetic waves in an SWS. As discussed in [27] and in Sections 2.3 and 2.4, the SIP in the cold periodic, lossless,

structure has a dispersion relation that, in the neighborhood of ω_{SIP}, is approximated by a third order power as

$$(\omega - \omega_{\mathrm{SIP}}) \approx h(k - k_{\mathrm{SIP}})^3 \tag{2.1}$$

where ω_{SIP} is the angular frequency at which three eigenmodes coalesce, h is a constant that depends on the chosen SWS parameters, k is the Floquet-Bloch wavenumber in the periodic and lossless SWS and k_{SIP} is the same at the SIP. As shown in the dispersion diagram of the fundamental Brillouin zone in Fig. 2.1(c), two different SIPs are possible at ω_{SIP}: (i) an SIP in the region $0 < kd < \pi$ that exhibits positive group velocity for frequencies higher and lower than the SIP frequency and (ii) another SIP in the region $\pi < -kd + 2\pi < 2\pi$ that is associated to negative group velocity for frequencies higher or lower than the SIP frequency. In the rest of the chapter we are assuming that the electron beam is synchronized with electromagnetic modes with wavenumber in the range $0 < kd < \pi$ as shown in Fig. 2.1(c). Therefore, the electron beam interacts with eigenmodes with SIP associated to the positive-slope branch of the dispersion diagram for frequencies in the vicinity of ω_{SIP}. Indeed, *near* the SIP angular frequency ω_{SIP} there are three eigenmodes with distinct Floquet-Bloch wavenumbers k provided by (2.1) where h is positive. Two eigenmodes have complex conjugate wavenumbers and thus represent evanescent waves while the third one has a purely real Floquet-Bloch wavenumber and thus represents a propagating wave in the lossless SWS (the one shown in the upper branch of Fig. 2.1(c)). These three eigenmodes are independent in the sense that they have independent eigenvectors, i.e., different field distributions in the unit cell of the periodic structure for $\omega \neq \omega_{\mathrm{SIP}}$. Note that the group velocity is always positive near ω_{SIP}, contrarily to what happens in SWSs with DBE [31]–[33] where near the DBE four eigenwaves with

both positive and negative group velocities are present. Exactly at $\omega = \omega_{\mathrm{SIP}}$ the three eigenmodes associated to the SIP coalesce in their wavenumbers and eigenvectors; and the system matrix description of the periodic structure becomes defective [27], [40]. To provide a complete basis for the field propagating at the SIP; generalized eigenvectors shall be considered and thus such fields grow linearly and quadratically along the z-direction [34], [40] because of the special SIP dispersion.

To realize an SIP in a cold reciprocal SWS, three waves must be periodically-coupled. Therefore, the minimum realization of such phenomenon is achieved using three CTLs as in Fig. 2.1(a) that are able to support three eigenmodes in each direction, i.e., a total of six eigenmodes at each frequency if we account for both the k and the $-k$ solutions. In contrast to the proposition in [27] that showed that one dimensional magnetic photonic crystals (MPCs) develop SIP and DBE characteristics, provided that nonreciprocal magnetic materials (ferrites for instance) are utilized. As such, in MPCs the dispersion diagram is asymmetric due to non-reciprocity. In [41] multi-ladder lumped circuit model is shown to emulate a $\omega - k$ dispersion diagram with a stationary inflection point.

We utilize here the three CTLs model in Fig. 2.1(b) to mimic the dispersion of an SWS with SIP. The series capacitance models cutoff frequencies in metallic waveguides (see Ch. 8 in [42]). The *generalized Pierce theory* developed in [22], [31], [32] allows the electron beam to interact with multiple waves in an SWS. The electron beam effect on the CTL is described using the equivalent, distributed, dependent current generators as seen in Fig. 2.1(b). See Refs. [31]–[33], [38] for more details on the generalized Pierce theory of multimodal periodic SWS interaction with an electron beam, including a Lagrangian formalism in [37]. We employ such general framework to investigate a specific SWS that

develops an SIP. An example of the dispersion relation around the SIP is shown in Fig. 2.1(c) for a normalized case of the three CTLs shown in Fig. 2.1(a) where, as customary, only the real branches (i.e., with k purely real, assuming absence of losses) of the $\omega - k$ diagram is plotted. The plot also shows the so called "beam line" given by the charge wave dispersion relation $(u_0 k - \omega)^2 = 0$, where u_0 is the average speed of the electrons in the electron beam [3], [44]. The three-eigenmode synchronous interaction occurs when the beam line is chosen to intersect the SIP as seen graphically in Fig. 2.1(c). In other words, the proposed regime of operation mandates a *three-eigenmode synchronization* with the electron beam in which the phase velocity of the eigenmodes in the SWS equals the velocity u_0 of electrons, i.e., in the proposed regime the TWT design formula is

$$u_0 = \omega_{\mathrm{SIP}}/k_{\mathrm{SIP}}. \tag{2.2}$$

In the following sections, we first investigate the characteristics of the cold structure exhibiting the SIP in terms of transmission and bandwidth, which are essential for achieving wideband amplification. Then, we show the amplification characteristic of the three-mode SWS synchronous regime with an electron beam. We explore mainly two cases of SWS interacting with electron beams: SWSs with ideal SIP, and SWSs with slightly positive dispersion slope (i.e. positive group velocity) at the frequency where modes tend to coalesce.

Sec. 2.3 Cold SWS Featuring SIP

A. Three CTL Model and Cold SWS Structure

The proposed multimode periodically coupled SWS featuring SIP is modeled by three CTLs as schematically shown in Fig. 2.1(a). In Fig. 2.1(a), each unit cell of the periodic three

CTLs is composed of two successive CTL segments *A* and *B* and has the total length of *d*. In addition, each segment is described using TL distributed parameters including coupling capacitances and inductances per unit length in Fig. 2.1(b), whose values are reported in Appendix B.

In order to show the SIP in periodic structures and the slow-wave resonance behavior of the cold periodic CTLs with finite length (*L=Nd*), we use a transfer matrix procedure already explained in [22], [31], [32], [45]. In particular, we use a six-dimensional state vector $\boldsymbol{\Psi}(z) = [\boldsymbol{V}^T(z) \quad \boldsymbol{I}^T(z)]^T$, where we have $\boldsymbol{V}^T(z) = [V_1(z) \quad V_2(z) \quad V_3(z)]$, and $\boldsymbol{I}^T(z) = [I_1(z) \quad I_2(z) \quad I_3(z)]$, that describes the evolution of the RF field amplitudes in the SWS. The evolution of this state vector from a coordinate z_1 to z_2 is described by $\boldsymbol{\Psi}(z_2) = \underline{\mathbf{T}}(z_2, z_1)\boldsymbol{\Psi}(z_1)$, where $\underline{\mathbf{T}}$ is a 6×6 transfer matrix [31], [32]. The six eigenmodes supported by three CTLs are provided by the eigenvalue problem

$$\left[\underline{\mathbf{T}}(z+d, z) - e^{-jkd}\underline{\mathbf{1}}\right]\boldsymbol{\Psi}(z) = 0, \tag{2.3}$$

where $\underline{\mathbf{1}}$ is the 6×6 identity matrix. The six Floquet-Bloch wavenumbers are obtained by solving the dispersion equation

$$D_{\mathrm{SWS}}(\omega, k) = \det\left[\underline{\mathbf{T}}(z+d, z) - e^{-jkd}\underline{\mathbf{1}}\right] = 0 \tag{2.4}$$

discussed in the following sections and in Appendix A. The ω, k pairs solutions of (2.4) provide the dispersion diagram in Fig. 2.1(c), where, as customary, only the pairs with both real ω and wavenumber k are plotted for simplicity. Note that (2.3) provides the six associated eigenvectors at any angular frequency different from ω_{SIP}. However exactly at the SIP frequency there is only an independent eigenvector associated to k_{SIP} and one to $-k_{\mathrm{SIP}}$, and two generalized eigenvectors associated to each wavenumber [34], [40]. Generalized

eigenvectors provide field solutions that grow linearly and quadratically along the z-direction [34], [40].

We find that, as an illustrative example, the periodic three CTLs model in Fig. 2.1(a), is able to support an SIP at $f_{\mathrm{SIP}} = \omega_{\mathrm{SIP}}/(2\pi) = 1.16$ GHz, when using the CTLs parameters provided in Appendix B. The coupling among the three CTLs are tuned such that its cold, lossless, dispersion relation features an SIP in the upper branch, as shown in Fig. 2.1(c) where only the modes with purely real k (Floquet-Bloch wavenumber) are plotted.

Notice that the cold SWS is a reciprocal periodic structure, therefore if k is a Floquet-Bloch wavenumber solution of the dispersion equation (2.4),$-k$ is also a solution of (2.4). Thus, the SIP also exists when the three modes with $-k$ coalesce at $-k_{\mathrm{SIP}}$, still at $\omega = \omega_{\mathrm{SIP}}$. Furthermore, because of periodicity, if k is a solution of the dispersion equation, then also $k + m2\pi/d$ is a solution, where m = 0,±1, ±2, ..., is the Floquet harmonic index and d is the period of the SWS. Therefore, if SIP exists at $\pm k_{\mathrm{SIP}}$, an SIP is visible in the dispersion diagram at all the Floquet harmonics whose wavenumber is given by $\pm k_{\mathrm{SIP}} + 2m\pi/d$. It is important to point out that with SWSs that support three eigenwaves in each direction the SIP occurs *inside* the Brillouin zone of the periodic structure; it does not occur at the Brillouin zone boundaries ($k = 0$ and $k = 2\pi/d$) nor at its center ($k = \pi/d$) hence it is not a band edge condition. The dispersion diagram in Fig. 2.1(c) provides the Floquet-Bloch wavenumber in the Brillouin zone defined here from $k = 0$ to $k = 2\pi/d$, keeping in mind that the dispersion is symmetric around any $k = m\pi/d$ which is a result of reciprocity of the cold SWS. Note that both the SIP frequency and the flatness of the dispersion curve at $\omega = \omega_{\mathrm{SIP}}$ can be arbitrarily changed by tuning the coupling parameters between the three CTLs.

To further explore the properties of the CTLs with third order modal degeneracy in Fig. 2.1(a), we consider a finite-length cold CTLs structure consists of N unit cells as in Fig. 2.2(a). The cold voltage transfer function

$$TF_1 = \frac{V_{\text{out1}}}{V_{\text{in1}}}, \tag{2.5}$$

is obtained from the transfer matrix formalism. Here V_{out1} is the voltage at the first TL output termination impedance Z_{L1} and V_{in1} is the input voltage of the first TL as shown in Fig. 2.2(a). Here we only excite the first TL as in Fig. 2.2(a), and we first assume that $Z_{\text{s1}} = Z_{\text{L1}} = 75\ \Omega$, while all the other input and output terminals are short circuited. The magnitude of the voltage transfer function TF_1 is plotted versus frequency for different number of unit cells (N) in Fig. 2.2(b), where results are shown for N=8 in dashed red, N=16 in solid blue, and N=24 in dotted black. It is observed that there are multiple resonance peaks near the SIP angular frequency ω_{SIP}, and the main resonance denoted by ω_r, is the sharpest and the closest to ω_{SIP}, featuring higher quality- (Q-) factor than the others. As the number of unit cells (N) increases more and more resonance peaks are observed and the main one becomes even sharper.

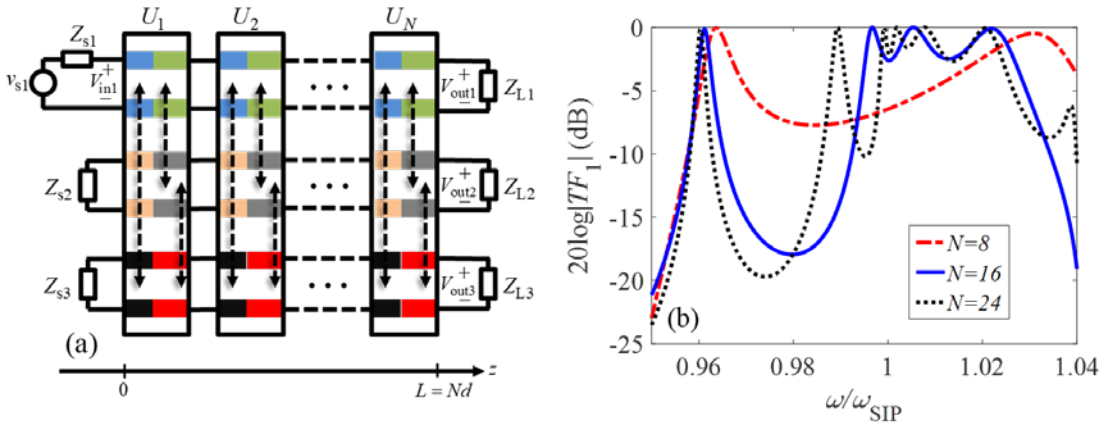

Fig. 2.2 (a) Finite length of a three CTLs periodic structure, with total length $L = Nd$ including loading and excitation, where N is the number of unit cells shown in Fig. (2.1). (b) Magnitude of the voltage transfer function $TF_1 = \frac{V_{out1}}{V_{in1}}$ for different number of unit cells (N = 8, 16, 24) with $Z_{s1} = Z_{L1} = 75\ \Omega$ and short circuit at all the other ports. This Result is obtained by F. Yazdi and M. Veysi using Matlab.

B. Engineering of the Dispersion Diagram with SIP

The transmission peaks in Fig. 2.2(b) are associated with the Fabry-Perot resonances of the finite cold periodic SWS. The sharper the resonance, the larger the group delay associated with it. This leads to high field enhancement and high Q-factors as the length of the SWS increases, which may also induce oscillations.

Depending on the target application, either to reduce the starting oscillation beam current (i.e., threshold current) for oscillators or to improve the gain and bandwidth for amplifiers, in this section we show how to synthesize and control the group velocity near the SIP frequency. By tuning the coupling amount between the TLs we can engineer the dispersion diagram to have small positive group velocities ($\partial\omega/\partial k > 0$) or small negative group velocities ($\partial\omega/\partial k < 0$) around the SIP frequency instead of the ideal case with zero group velocity (see Appendix A). The dispersion diagrams of the three cases near the SIP frequency are shown in Fig. 2.3(a) where we obtain a positive slope (dotted green curve)

and negative slope (dashed red curve) group velocities around the SIP by having small changes in the coupling capacitors and inductors as provided in Appendix B. The magnitude of the voltage transfer function defined in (2.3) for these three cases is calculated and plotted in Fig. 2.3(b) for the case of having N=16 unit cells and $Z_{s1} = Z_{L1} = 75\ \Omega$ while the other TL terminals are short circuited.

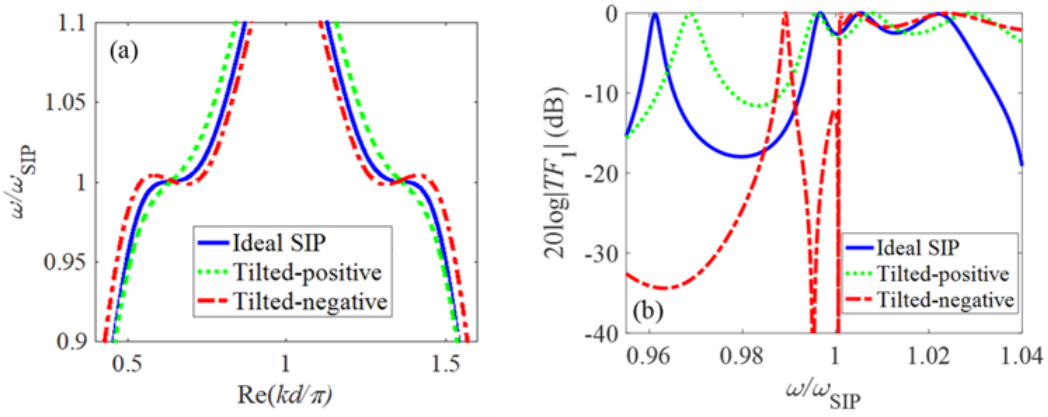

Fig. 2.3 (a) Engineering the slope of the upper branch of the dispersion diagram in Fig. 2.1 to have positive and negative slopes around the SIP compared to the ideal SIP case of zero group velocity (in blue). (b) Magnitude of the voltage transfer function $TF_1 = \frac{V_{out1}}{V_{in1}}$ in dB for three different scenarios of ideal, tilted-positive and tilted negative dispersion relation around the SIP, for N=16 unit cells with $Z_{s1} = Z_{L1} = 75\Omega$ and short circuit at all the other ports. The result is obtained by F. Yazdi.

By increasing the slope of the dispersion curve around the SIP frequency to achieve a positive group velocity, the resonance transmission peaks near the SIP frequency become wider compared to those for the ideal SIP having zero group velocity. This is beneficial for achieving higher bandwidth in amplifier applications while retaining gain enhancement, and we will elaborate further on that in Section 2.4. On the other hand, by changing the coupling parameters we also obtain a negative slope in the dispersion diagram curve around the SIP frequency which results in sharper resonance peaks and consecutively

higher Q-factors, as shown in Fig. 2.3(b). Therefore, such CTLs with locally negative slopes would be beneficial for oscillator applications which would be further discussed in Section 2.4, though the main focus of this chapter is to discuss amplification properties of SWSs with SIP.

C. Effects of Loss and TL Terminating Loads

The Q-factor of a cavity made by a finite length SWS depends also on the terminating loads of the CTLs. A proper loading choice is of critical importance for the design of oscillators and amplifiers. Therefore, in this section, we examine different loading scenarios for the finite length CTLs with SIP. The magnitude of the voltage transfer function for the ideal SIP scheme is shown in Fig. 2.4(a) for three different loading scenarios. In the first loading scenario (blue solid curve), we terminate both input and output of the first TL with a resistive load ($Z_{s1} = Z_{L1} = 75\Omega$) while all the other TL terminals are short circuited. The second loading scenario [red dotted curve in Fig. 2.4(a)] is the case where the input terminal of the first TL and all the three output TL terminals are terminated by an equal resistive load ($Z_{s1} = Z_{L1} = Z_{L2} = Z_{L3} = 75\Omega$) while the input terminal of the two other TLs are short circuited. The third loading scenario (black dashed curve) is similar to the second one, i.e., $Z_{s1} = Z_{L1} = Z_{L2} = Z_{L3} = 75\Omega$ except that now the *input* terminals of the second and third TLs are open. It is observed that by terminating all the three output terminals with a load, the amplitude of the transfer function [defined in (2.5)] drops compared to the case where two output terminals are short circuited. However, the bandwidth increases dramatically specially for the third loading scenario where the second and third TLs' input terminals are left as open circuit. Therefore, for amplifier applications since we are interested in having higher bandwidth, we use the third loading scenario here after. Note that the value of the

resistive load would also affect the bandwidth. Here, we use the resistance loads of 75 Ω which seems providing the widest bandwidth. In the next section we will focus on this specific choice, though a deeper investigation of loading schemes in multiple CTLs could be beneficial to further maximize the bandwidth.

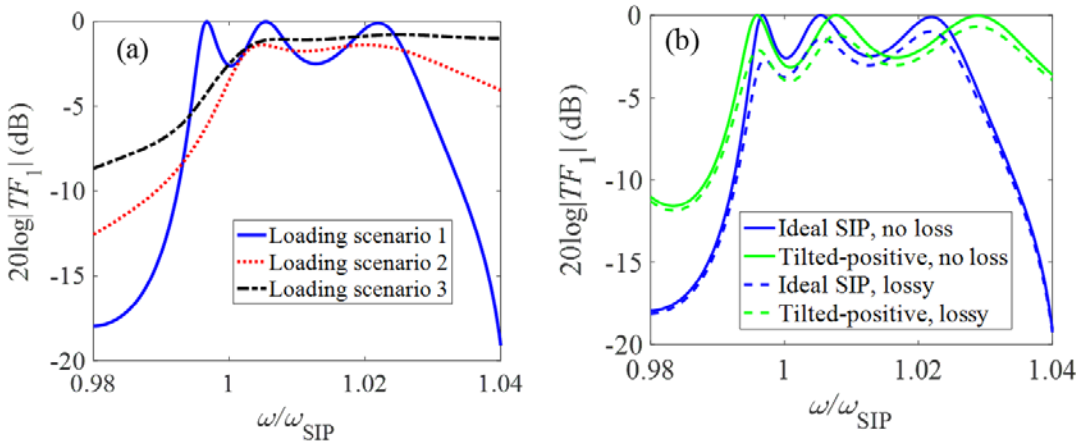

Fig. 2.4 (a) Comparison of three different loading scenarios for the finite three CTL structure. (b) Magnitude of the voltage transfer function of the two schemes of ideal SIP and tilted-positive for two cases of no loss and lossy structures when we have N = 16 unit cells with $Z_{s1} = Z_{L1} = 75\Omega$ and short circuit at other ports as loading. This Result is obtained by F. Yazdi, M. Othman, and M. Veysi.

Next, we investigate the impact of the SWS losses on the transfer function. The presence of loss can impact the quality factor of the SWS structure and therefore its performance especially where we have high sensitivity to defects near the SIP. In Fig. 2.4(b) we plot the magnitude of the voltage transfer function for the two SWS with ideal and tilted-positive SIP with and without considering loss effects. Here we have assumed the loss as a distributed series resistance of $R_{loss} = 5\ \Omega/m$ in each segment of the periodic three CTLs, composed of N=16 unit cells. The results in Fig. 2.4(b) show how the magnitude of the transfer function as well as the Q-factor decrease as compared to that in the absence of losses as expected, for both tilted and ideal SIP, when losses are accounted for.

Sec. 2.4 Hot SWS Featuring SIP

We investigate here the amplification in TWTs modeled as three CTLs interacting with an electron beam. We use the generalized Pierce theory developed in [31], [32] for multi transmission lines interaction with an electron beam. Accordingly, the interaction of the SWS modes with an electron beam is taken into account by modeling the beam as a continuous flow of charges, i.e., by charge waves as in [3], [22]. Such charge wave describes the bunching and debunching of the beam's electrons, which causes energy exchange between the beam and the modes in the SWS. The electron beam has an average (d.c.) current $-I_0$ (I_0 is a real, positive number) along the $+z$ direction and a d.c. equivalent beam voltage V_0 that is related to the average electron velocity u_0 by $V_0 = u_0^2/(2\eta)$, where $\eta = e/m = 1.758 \times 10^{11}$ C/kg is the electron charge-to-mass ratio, where $-e$ and m refer to the charge and mass of the electron, respectively. The electromagnetic fields in the waveguide induce a perturbation (modulation or disturbance) on the charge wave [3] described by a modulation of the charge wave current, I_b, and modulation of beam velocity, u_b, and equivalent kinetic voltage modulation $V_b = u_0 u_b/\eta$ [22], [31], oscillating at the same frequency as the electromagnetic fields in the SWS. Therefore the total beam current along the positive z direction is $-I_0 + I_b$ with $|I_b| << I_0$ and the total equivalent beam voltage $V_0 + V_b$ with $|V_b| << V_0$, for small-signal considerations. We conveniently define a space-varying *eight-dimensional state vector* composed of all the field quantities that vary along the z-direction, which are the transmission line voltage and current vectors already discussed in Sec. 2.3, as well as the charge wave modulation terms I_b and V_b. In summary, the system state vector made of eight components is

$$\boldsymbol{\Psi}(z) = [\boldsymbol{V}^T(z) \quad \boldsymbol{I}^T(z) \quad V_b(z) \quad I_b(z)]^T \tag{2.6}$$

and it describes the evolution of time-harmonic electromagnetic waves and beam charge wave along the z-direction using our multi TLs approach [22], [31], [32].

In order to investigate the oscillation and amplification behavior of the proposed three CTLs with SIP, in Sec. 2.4-*B*, we consider a finite length SWS composed of N unit cells as in Fig. 2.5 with appropriate source and loads. The power gain transfer function is defined as

$$G_{\mathrm{P1}} = P_{\mathrm{L},1}/P_{\mathrm{smax}} \tag{2.7}$$

where $P_{\mathrm{smax}} = |v_{\mathrm{s1}}|^2/[8\,\mathrm{Re}(Z_{\mathrm{s1}})]$ is the maximum available power at the input terminals of the first TL and $P_{\mathrm{L},1}$ is the power delivered to the load Z_{L1} of the first TL, since it is the port where most of the power is delivered as it will be clarified later on.

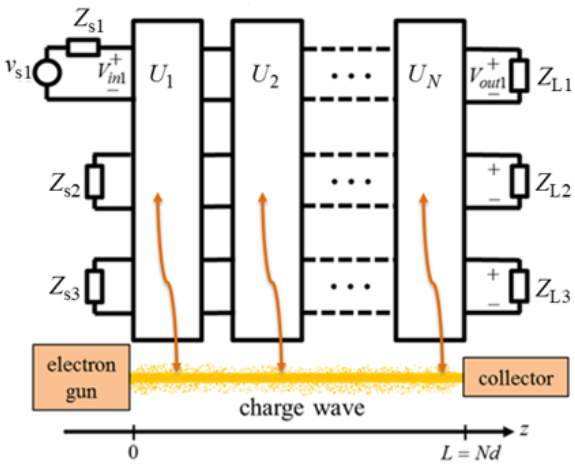

Fig. 2.5 Conceptual example of a three CTL structure interacting with an electron beam with the generalized Pierce model of the three CTLs, with unit cells as shown in Fig. 2.1(b) including the per unit length parameters. The blocks U_n represent unit cells made of the two segments *A* and *B* in Figs. 2.1(a) and 2.2, with parameters given in Appendix B.

A. Dispersion Relation of the Combined SWS-Electron Beam Interactive System

In this section, we analyze the dispersion relation of modes in a SWS, designed to have a SIP, interacting with an electron beam. We investigate the effect of the electron beam current on the dispersion diagram assuming the real frequency and a wavenumber k that can have complex values. Modes in the cold SWS are degenerate and satisfy the synchronous condition (2.2). The addition of gain perturbs the degeneracy condition though the degeneracy structure is somewhat preserved when gain levels per unit length are not so high. Here and in Appendix A we show the complex k dispersion diagram varying the electron beam current and observe how much the SIP condition is perturbed from the "cold" case.

The eight complex k modal solutions at any real angular frequency ω are found by solving for the eigenvalues of a system as in (2.3), where now $\boldsymbol{\Psi}(z)$ is the 8-dimensional state vector given in (2.6) and $\underline{\mathbf{T}}(z+d,z)$ is a 8×8 system matrix assocviated to the periodic CTLs interacting with the electron beam as discussed in [22], [31], [32]. In general, one can write the dispersion equation of the coupled SWS-electron beam system, simply as

$$D_{\mathrm{SWS}}(\omega,k)P_{\mathrm{beam}}(\omega,k)=C(\omega,k,I_0) \tag{2.8}$$

in which $D_{\mathrm{SWS}}(\omega,k)=0$ is the dispersion relation of the cold SWS given in (2.4), and $P_{\mathrm{beam}}(\omega,k)=0$ is the dispersion relation of the cold beam [44], namely

$$P_{\mathrm{beam}}(\omega,k)=(u_0k-\omega)^2-\Omega_P^2=0 \tag{2.9}$$

where Ω_P is the plasma angular frequency, which includes space charge effects [3], [9]. Note that (2.9) provides two solutions $k=\omega/u_0\pm\Omega_P$ for the electron beam-alone modal

solutions of the modulated charge wave; these solutions are positive and do not satisfy reciprocity, i.e., k and $-k$ are not both solutions of (2.9).

In the CTL-beam system, the function $C(\omega, k, I_0)$ on the right hand side of (2.8) represents phenomenologically the coupling between the electromagnetic modes of the cold SWS and those that would be supported by the electron beam alone. In simple cases such as in the original Pierce model, $C(\omega, k, I_0)$ can be written in an exact analytical form, (see for instance [3], [44] or [46]). The function $C(\omega, k, I_0)$ also might be understood as a perturbation term of the SWS system due to the electron beam.

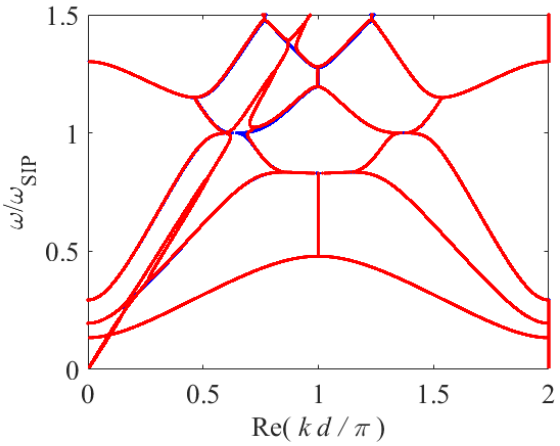

Fig. 2.6 Dispersion diagrams showing the *real* part of the complex Floquet-Bloch wavenumber k versus angular frequency, for both the "hot" and "cold" systems. Dispersion curves for the "hot" SWS-electron beam interactive system (shown in solid red lines) are calculated using an electron beam current of $I_0 = 0.5$A. Dispersion curves for the "cold" lossless SWS are shown with solid blue lines that are under the red curves (hence not visible) except for a small region near the interaction point (k_{SIP}, ω_{SIP}) given in (2.2). Zooms and more detailed plots of the dispersion diagram for various beam currents are reported in Appendix A. This result is obtained by F. Yazdi and M. Othman.

Note that one can always cast the dispersion of the interactive systems in the form given by (2.8). However, for the investigated cases reported here, where periodicity is involved and the SWS is made of three TLs, it is extremely tedious to find analytical expressions for $D_{\mathrm{SWS}}(\omega, k)$ or $C(\omega, k)$ since they involve the determinant of the 8×8 system matrix. On the other hand, it is useful to investigate the interaction in the vicinity of the SIP where the dispersion of the cold SWS is approximated by the SIP dispersion in (2.1) as shown in Appendix A.

Since synchronization between the electron beam and the CTLs occurs around the SIP frequency [see (2.2)], where three SWS eigenwaves coalesce, a strong interaction between the electron beam and the SWS modes is expected. As mentioned earlier we assume the beam interacting with the three degenerate eigenwaves associated to the SIP on the left side of the dispersion relation in Figs. 2.1(c) and 6 to exploit positive group velocity for high power amplification. To show what happens to the dispersion diagram of the hot SWS (in the presence of the electron beam) we plot in Fig. 2.6 the real part of k for both cold (blue curves) and hot structures (red curves) in a wide frequency range around the SIP frequency. Blue curves represent the dispersion diagram of the "cold" SWS and are covered by the red curves (blue curves are coincident with those in Fig. 2.1), except for a region close to the interaction point $(k_{\mathrm{SIP}}, \omega_{\mathrm{SIP}})$. There, one can see the deformation and splitting of the modal curves around the point where synchronization with the electron beam happens. However, away from the interaction point $(k_{\mathrm{SIP}}, \omega_{\mathrm{SIP}})$ the modes (red curves) asymptotically approach those of the cold structure (blue curves) because waves in the CTLs are no longer synchronized with the electron beam. For beam currents larger than that considered in Fig. 2.6 the deformation of the dispersion diagram of the hot structure

from that of the cold one extends significantly further from the SIP point. In any case the diagram is not symmetric with respect to $k = \pi/d$. A comprehensive investigation of the impact of the beam average current I_0 on the dispersion diagram for the hot structure is carried out in Appendix A.

B. Study of Instabilities at the SIP

In an infinitely long SWS interacting with an electron beam, the oscillation condition and the starting oscillation current can be calculated from the dispersion diagram of the structure as explained in Section 2.4. In an infinitely-long structure with the e-beam as a source of linear gain, the electromagnetic waves exhibit either unbounded growing oscillations in time at every fixed point in space, or growing oscillations only in space, i.e., progressing along *z*; those instabilities are commonly referred to as *absolute and convective instabilities, respectively* [47], [48]. Criteria for these two distinct instabilities in an infinitely-periodic interactive system can be drawn from investigating the dispersion diagram thereof following the Briggs-Bers condition [49], [50].

Amplification at a given real frequency is due to convective instability, i.e., one or more eigenwaves of the infinitely-long SWS coupled to the electron beam, whose propagation is described by $\exp(-jkz)$, is exponentially growing while they progress along *z*, hence their complex wavenumber should be such that $\mathrm{Im}(k) > 0$. Even though a system made of an *infinitely-long* SWS interacting with an electron beam does not exhibits absolute instability, there is another reason of why a system of *finite length* with internal amplification (i.e., convective instability) could start to oscillate. Growing oscillations could occur when amplified waves provide constructive interference with positive feedback after reflections

at the two ends of the SWS with gain. Condition for such occurrence of oscillations in a *finite length* structure is examined by tracing the location of the poles of the transfer function (i.e., (2.5)) in the complex angular frequency ω-plane as a function of the electron beam current I_0. In the following, the synchronous condition for RF amplification is assumed by choosing the velocity u_0 of the electrons to match the phase velocity of the three degenerate forward eigenmodes in the +z-direction according to (2.2).

For a stable (i.e., amplifying) system, all the system poles have positive imaginary parts in the complex ω-plane.

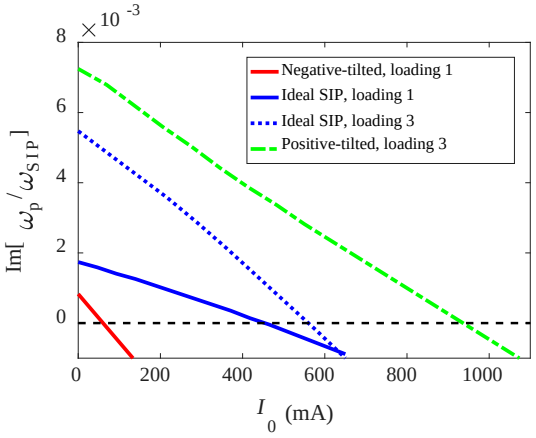

Fig. 2.7 Imaginary part of the pole nearest to SIP plotted versus beam current I_0 for four different scenarios: (i) tilted-negative regime (oscillator application) assuming loading scenario 1; (ii) ideal SIP regime assuming loading scenario 1; (iii) ideal SIP regime assuming loading scenario 3; (iv) tilted-positive regime (amplifier application) assuming loading scenario 3. The system is unstable when a pole has $\mathrm{Im}[\omega] < 0$. The "tilted-positive" case is the most stable. This result is obtained by F. Yazdi.

The system starts to oscillate whenever one of the ω-poles moves to the part of the ω-plane with negative imaginary part. Here, for simplicity we consider the voltage transfer function defined in (2.5) relative to a system made of an electron beam interactive with three lossless CTLs with load terminations of loading scenarios 1 and 3 introduced in

previous section. Although the *TF* in (2.5) exhibits many poles in the ω-plane, the pole closest to the SIP frequency (represented by $\omega_p = \omega_{\text{pr}} + j\omega_{\text{pi}}$) is of special interest. This is the ω-pole that transitions from the positive imaginary part of the ω-plane to the negative imaginary part (unstable region) with the increase of the electron beam current I_0, much faster than the other poles of the transfer function. Hence, it is the pole that is responsible for starting oscillations. For an amplifier regime, all poles should be in the stable region. Fig. 2.7 shows the trajectory of the imaginary part of such a pole as a function of beam current I_0, for four different scenarios, all with a SWS made of N = 16 unit cells. We are considering two loading scenarios here: (loading scenario 1) terminating both input and output of the first TL with a resistive load of 75 Ω while all the other four TL terminals are short circuited, and loading scenario 3) terminating the first TL input and all the three TL output terminals by an equal resistive load of 75 Ω while the input terminal of the two other TLs are left open. The starting oscillation beam current (I_{th}) is the beam current value for which the pole enters the unstable region ($\text{Im}[\omega_p] < 0$) from the stable region ($\text{Im}[\omega_p] > 0$). In other words, the pole crosses the realωaxis if a strong enough electron beam current is used in the SWS device, and after that the system will start oscillations. We observe from Fig. 2.7 that the SWS with titled SIP regime with *negative group velocity* (red solid curve) has the closest pole to the realωaxis which moves very quickly into the oscillation region by slightly increasing the beam current. Consequently, it has the lowest starting oscillation electron beam current and is best suited for oscillator designs. On the other hand, the SWS based on the regime with titled SIP with *positive group velocity* (dashed green curve) has the largest starting oscillation beam current compared to the other regimes. Hence the SWS with titled positive slope regime is best suited (compared to

the other cases in Fig. 2.7) for the high-power amplifier design. In the next subsection, we specifically examine the potential applications of SWS with ideal and titled SIP with positive group velocity for conceiving amplifier regimes, i.e., regimes based on convective instability. We observe from Fig. 2.7 that the starting oscillation beam currents for ideal SIP and tilted-positive SIP with the loading scenario 3 are $I_{\text{th}} = 0.56$ A and $I_{\text{th}} = 0.94$ A, respectively, and in all of our results hereafter we consider electron beam currents much smaller than these starting currents to avoid oscillations.

C. Amplification

The power gain defined in (2.7) is plotted in Fig. 2.8(a) versus normalized angular frequency near the SIP frequency for both amplifiers based on the ideal SIP regime and the tilted-positive one. The beam current value for each case is chosen such that the maximum power gains for both cases are equal to either 10 dB or 25 dB. In addition, the electron beam current values are chosen such that the structure operates in the stable region, so in each respective case we have $I_0 < I_{\text{th}}$.

In our simulations for SIP amplifiers we assume loads of 75 Ω at every output port while the two lower input terminals are left open circuited (loading scenario 3), since this configuration provides a large enough bandwidth to prove benefits, though optimization of the regime of operation would lead to even better results. It is observed from Fig. 2.8(a) that the amplifier based on tilted SIP regime with the positive group velocity requires a larger beam current as compared to the amplifier based on an ideal SIP to provide the same amount of the power gain. Although the amplifier with tilted SIP with positive group

velocity features a lower gain, it provides a higher bandwidth as compared to an ideal SIP case.

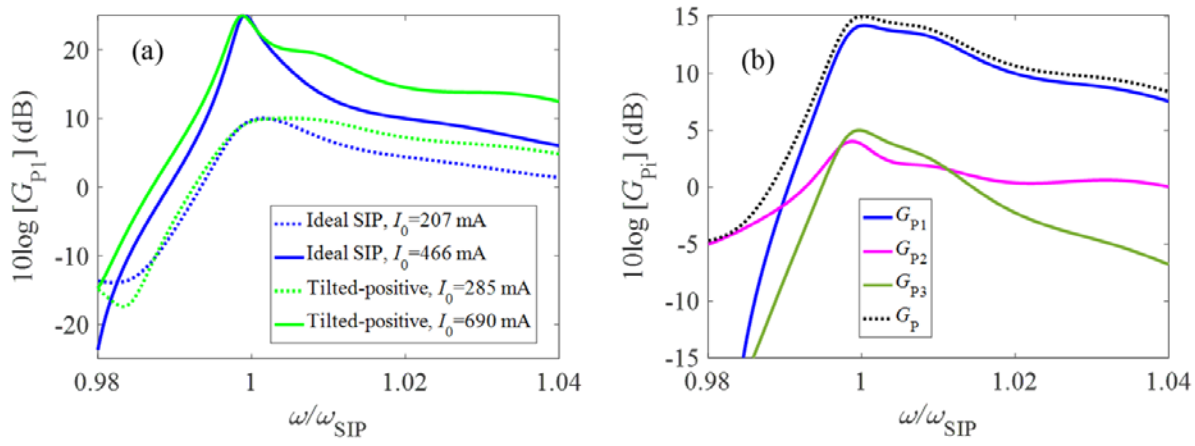

Fig. 2.8 (a) Comparison of the power gain $G_{\mathrm{P1}} = P_{\mathrm{L},1}/P_{\mathrm{smax}}$ for both the ideal and the tilted-positive SIP regimes interacting with an electron beam in which the value of beam current is selected such that the maximum power gain is set to be either 10 dB or 25 dB. (b) Power gain at each of the three output ports and the total output power gain G_{p}, for a regime of operation based on the SWS with tilted-positive group velocity. For both plots the gain is calculated for a SWS with N=16 unit cells with $Z_{Li} = 75\Omega$, i=1,2,3, $Z_{\mathrm{s1}} = 75\Omega$ and open circuit for the two other input ports. We show only convective instability regimes of operation. This Result is obtained by F. Yazdi and M. Veysi.

Next, we investigate in Fig. 2.8(b) the distribution of output power $P_{\mathrm{L,i}}$, with i = 1, 2, 3, on the output CTLs terminals. The power gain of each output is defined as $G_{\mathrm{P,i}} = P_{\mathrm{L,i}}/P_{\mathrm{smax}}$. In addition, the total power gain, i.e., $G_P = \sum_i P_{\mathrm{L,i}}/P_{\mathrm{smax}}$, is also plotted for comparison. It is observed from Fig. 2.8(b) that most of the available power is delivered to the first TL's output terminal and very small portions of the available power is transferred to the other two TLs' output terminals. Though this condition may vary depending on the adopted CTL configuration.

In Fig. 2.9(a), we plot the total power gain (G_P) relative to the amplification regimes with ideal SIP and tilted SIP with positive group velocity versus electron beam current I_0. To provide a better assessment on the performance of the SIP regimes of operation, we also plot the power gain in a TWT amplifier made of a single periodic TL having the same total length and the same characteristic impedance as the one in the TLs used for the SIP cases. The SWS made of single TL is assumed to be periodic to provide a fair comparison, since results are compared to those of amplifiers made of periodic SWS with SIP. The parameters of the single TL interacting with the electron beam are provided in Appendix B, and the results are based on a Pierce model for the single mode SWS made of one TL interacting with the electron beam, with calculations done using a transfer matrix formalism.

Note that for each amplification regime the range of the beam current is such that $I_0 < I_{\text{th}}$ so it operates in the stable region. From Fig. 2.9(a) we observe that, for the same amount of electron beam current, the amplifier based on the ideal SIP regime provides the highest power gain as compared to the two other cases. However, the amplifier with ideal SIP has a very limited bandwidth as compared to the amplifier with tilted-positive SIP as it is going to be discussed in the following. Note also that the gain for the amplifier with tilted SIP with positive group velocity is still much larger than the single TL case.

The power gain of the proposed tilted-positive SIP amplifier is plotted in Fig. 2.9(b) versus the length of the periodic SWS with N unit cells and compared it to that of the single TL amplifier. This figure shows a huge advantage for the proposed amplifiers based on the ideal SIP and tilted-positive SIP regimes in terms of power gain as N increases, when compared to the single TL.

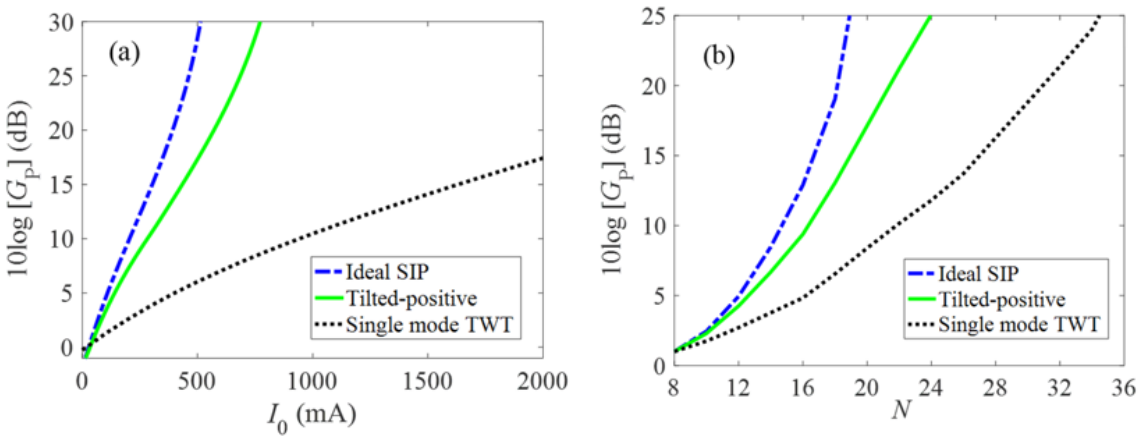

Fig. 2.9 (a) Power gain (in dB) of the proposed ideal SIP and tilted-positive regimes of TWT operation, compared with a standard regime of amplification based on a finite, periodic TL, modeling a single mode TWT, having the same characteristic impedance, length and loading plotted versus the beam current. Results are based on structures with N=16 unit cells, with loads of $Z_L = 75\,\Omega$ (loading scenario 3) and $R_{\text{loss}} = 5\,\Omega/m$. (b) Total power gain versus the number of SWS unit cells, N. Comparison among amplification regimes based on SWS with the ideal SIP, the titled-positive dispersion, and a single TL model introduced in part (a). The values of the electron beam current are selected for each regime such that the same gain is achieved for the case of N = 8 unit cells. The resulting electron beam current values for the ideal and tilted-positive SIP is 263 mA, in both cases, whereas for single TL regime the beam current is 385 mA. The threshold beam currents (I_{th}) for ideal, tilted-SIP, and 1TL are 560 mA, 880 mA and 4.7 A respectively. This Result is obtained by F. Yazdi, M. Othman, and M. Veysi.

As an important figure of merit for amplifiers, we plot in Fig. 2.10(a) the gain-bandwidth product ($G \times BW$) results for the ideal SIP and the tilted-positive amplification regimes as compared to that of the periodic single TL pierce model versus electron beam current. In this figure, the $G \times BW$ is defined as the product of the maximum power gain and the 3dB-gain bandwidth. The transmission lines parameters as well as loading for the three regimes of operation are provided in the Appendix B and also in the caption of Fig. 2.10. The results of Fig. 2.10(a) show that both the SIP amplification regimes outperform the conventional

regime based on the single TL Pierce model, for electron beam currents larger than I_0 =300 mA where the gain is high enough to be desirable for amplifier applications.

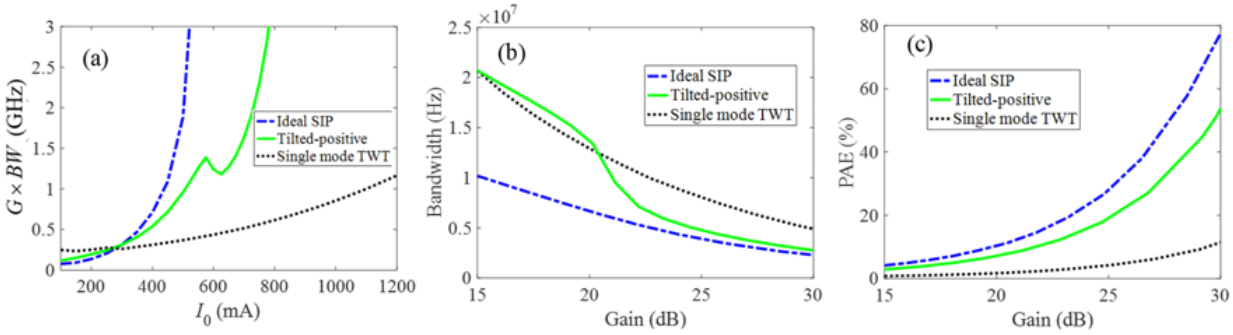

Fig. 2.10 (a) Comparison of the gain-bandwidth product (G×BW) of TWT amplifiers based on SWS regimes based on ideal SIP and tilted-positive dispersion, versus electron beam current I_0. Results are also compared with a TWT made of a SWS with only one periodic TL (single mode TWT) having the same length and average characteristic impedance. (b) Bandwidth comparison for the three aforementioned regimes of operation versus power gain (in dB). (c) Power added efficiency (PAE) in percentage for the three regimes as a function of power gain (in dB). In (b) and (c), different beam currents are chosen for the three regimes such that all three cases have equal gains. In all cases we are assuming a SWS made of N=16 unit cells and the per unit length resistance of $R_{\text{loss}} = 5\ \Omega/\text{m}$ with $Z_{\text{Li}} = 75\ \Omega$, i = 1, 2, 3, $Z_{\text{s1}} = 75\Omega$ and open circuit at the two other input ports for the two SIP regimes, and $Z_L = Z_s = 75\ \Omega$ for the single TL regime. This Result is obtained by F. Yazdi, M. Othman, and M. Veysi.

In addition, we plot in Fig. 2.10(b) the 3dB-gain bandwidth versus power gain for the three regimes of amplification discussed previously. Different values of gain are obtained by changing the electron beam current I_0. It should be noted that in order to have equal power gain for the three cases mentioned above, the values of the electron beam current are different for each case which results in different power added efficiency for each case as discussed next. The first and foremost observation of the Fig. 2.10(b) is that although higher bandwidths is expected for the single TL amplifier, for similar gain the tilted-

positive SIP amplifier has slightly higher bandwidth, within the 15 to 20 dB gain range. Though bandwidth of the new SIP amplification regimes is not higher than that of the single TL amplifier in these results (proposed here for the first time), if we look at the $G \times BW$ figure of merit in Fig. 2.10(a), it is clear that both SIP regimes of amplification provide higher values than the single TL regime. Furthermore, it must be noted that the amplifier based on the tilted-positive SIP regime, though it provides smaller gain than the ideal SIP regime, it provides higher bandwidth.

Finally, we examine another important parameter for amplifiers, the power added efficiency (PAE), which is defined (in percentage) as

$$\mathrm{PAE} = \frac{P_{\mathrm{out(RF)}} - P_{\mathrm{in(RF)}}}{P_{\mathrm{DC}}} \times 100, \tag{2.10}$$

where P_{DC} is the d.c. electron beam power (defined as $P_{\mathrm{DC}} = V_0 I_0$), whereas $P_{\mathrm{in(RF)}}$ and $P_{\mathrm{out(RF)}}$ are the input and total output RF powers respectively. In all cases, we use the same $P_{\mathrm{in(RF)}} = (1/2)\, Re\{V_{\mathrm{in1}} I_{\mathrm{in1}}^{*}\}$, and $P_{\mathrm{out(RF)}} = G_p P_{\mathrm{in(RF)}}$. The total output power is on the three loads, though the power on load 1 is dominant. We observe from Eq. (2.10) that when comparing the three regimes with equal gain, the larger the required beam current I_0 for a given gain value, the smaller the PAE. Hence, the SWS-beam regime that requires the smaller beam current, at equal gain, has the largest PAE. In Fig. 2.10(c) we have plotted the PAE for the three SWS regimes mentioned above versus the power gain (power gain is varied by changing the electron beam current I_0). The foremost observation is that amplifiers based on the SIP regimes of operation feature significantly higher PAE as compared to the amplifier based on the single TL regime of operation, in particular at large power gains.

Sec. 2.5 Conclusion

We have reported a new regime of operation for SWSs with a third order degeneracy interacting with an electron beam with possible application in TWT amplifiers. The new regime of operation is based on a strong synchronous interaction between an electron beam and three Floquet-Bloch eigenmodes in a SWS having a stationary inflection point (SIP). Previously, in [31]–[33] we have analyzed a regime of operation where the electron beam was interacting with four degenerate eigenmodes at the DBE, which is a fourth order degeneracy at which eigenmodes have zero group velocity. Both positive and negative group velocities exist at frequencies near that of the DBE (like other band edge conditions, such as the RBE). The DBE was proposed to conceive low-threshold or high-efficiency oscillators. Instead, the SIP interaction regime for amplifiers investigated here does not exploit electromagnetic band gaps.

The proposed SIP-based regime of amplification utilizes only vanishing or slightly positive group velocity for frequencies either higher or lower than the SIP one leading to high power amplifiers. Note that the considered SIP associated with positive group velocities is the one shown in Figs. 2.1(c) and 2.6 occurring in the range $0 < kd < \pi$. Though not shown here one could conceive also a regime where the electron beam is synchronized with the SIP in the range $\pi < kd < 2\pi$, the range of wavenumbers associated with negative group velocity for backward wave oscillator designs, which are left for future investigation.

We have demonstrated that the new proposed amplification regime based on SIP provides a route for three improvements in TWT amplifiers: large gain, large gain-

bandwidth product ($G \times BW$) as well as higher power efficiencies in TWTs compared to a Pierce-like TWT regime of operation (modeled as a single TL here) having the same length and electron beam current.

Besides amplifiers based on SWSs with ideal SIP condition we have explored also one regime of operation where dispersion engineering leads to a modified SIP condition where group velocity is non-vanishing and always slightly positive. The important feature of the proposed scheme is that the slope of the dispersion relation can be engineered for enhancing the bandwidth. We have shown that the SIP with a slightly positive group velocity results in a higher bandwidth at the cost of gain/efficiency.

We have investigated how the positive group velocity of the three eigenmode degeneracy exploited in this study makes these TWTs less prone to start oscillations compared to the regimes with vanishing group velocity (Fig. 2.6). Indeed the proposed SIP regime with vanishing or slightly positive group velocity is less prone to start oscillations than the previously studied regime based on the DBE [33] whose degeneracy involved also Floquet-Bloch modes with negative group velocity. We have also shown that we can engineer the SIP regime to have a slightly negative group velocity in the region $0 < kd < \pi$ and this provides significantly lower oscillation threshold than the SIP counterpart with positive group velocity, and may be beneficial for low threshold oscillator designs which can be a future research venue.

Despite the SWS with SIP dispersion is here based on an ideal periodic CTLs, realistic metallic waveguides with SIP can be devised analogously to what was previously demonstrated theoretically [35] and experimentally [51]. such circular metallic

waveguides are able to support the DBE. The strategy to obtain realistic SWSs with SIP is to consider a periodic waveguide that supports three modes that are periodically coupled by modulating the shape in the longitudinal direction. Nevertheless, here we have shown for the first time some possible advantages of a new regime of operation for TWT amplifiers that could benefit microwave and millimeter wave generation. Precise engineering of such a multimode metallic waveguide with SIP is left to a future investigation now that we have demonstrated the possible advantages of TWT amplifiers based on SWSs exhibiting ideal SIP or SIP with positive tilt.

This chapter is reproduced based on the material in: [F. Yazdi, M. A. K. Othman, M. Veysi, A. Figotin, and F. Capolino, "A New Amplification Regime for Traveling Wave Tubes with Third Order Modal Degeneracy," *IEEE Trans. on Plasma Science*, Vol. 46, No.1, pp. 43-56, Jan. 2018.]

Appendix A Dispersion Relation for Interaction of the SWS with Electron Beam

In this Appendix, a detailed investigation of the dispersion relation of the hot SWS structure (the combined SWS-electron beam system) is offered and we observe how the complex wavenumber k is affected by the strength of the electron beam current I_0.

As mentioned in Section 2.4, the general dispersion equation of the coupled SWS-electron beam system is written as in Eq. (2.8) with the beam dispersion relation provided in Eq. (2.9). Therefore, complex wavenumber solutions of Eq. (2.8) for real frequency provide the eight curves of the modal dispersion diagram in Fig. 2.6. In Eq. (2.8) the dispersion diagram of the combined structure is obtained by modifying the dispersion of the cold SWS. Therefore, it is important to characterize the dispersion of the cold SWS for

the ideal SIP and also for the titled cases described in this chapter. In the following $D_{\mathrm{SWS}}(\omega,k)$ =$D_{\mathrm{SIP}}(\omega,k)$ represents the case of ideal SIP, whereas $D_{\mathrm{SWS}}(\omega,k)$ = $D_{\mathrm{SIP,titled}}(\omega,k)$ represents a SWS that instead of the ideal SIP expresses a slightly *tilted* version of it. Note that the dispersion diagram for a SWS that exhibits an ideal SIP, can be approximated as $D_{\mathrm{SIP}}(\omega,k) \approx (\omega-\omega_{\mathrm{SIP}}) - h(k-k_{\mathrm{SIP}})^3 = 0$ in the vicinity of the SIP, which is coincident with Eq. (2.1). It is noteworthy to show that after some algebraic manipulations the dispersion relation for the *titled* SIP can be approximated as a perturbation of $D_{\mathrm{SIP}}(\omega,k)$ as

$$D_{\mathrm{SIP,titled}} \approx D_{\mathrm{SIP}} - v_t k = (\omega-\omega_{\mathrm{SIP}}) - h(k-k_{\mathrm{SIP}})^3 - v_t k = 0, \qquad \text{(A1)}$$

where v_t is the minimum group velocity (in magnitude) of titled SIP cases, that occurs at the original SIP wavenumber $k = k_{\mathrm{SIP}}$. In other words, the minimum group velocity of the titled-SIP mode occurs at $k = k_{\mathrm{SIP}}$, and based on (A1) is given by

$$\left.\frac{d\omega}{dk}\right|_{k=k_{\mathrm{SIP}}} = v_t \qquad \text{(A2)}$$

The formula in (A1) assumes that the tilt results in a small but non-vanishing group velocity at $\omega = \omega_{\mathrm{SIP}}$, for which the SWS retains some of the degeneracy features within the limit of small perturbation. For $v_t > 0$ the dispersion has a positive slope and that is what we proposed in a TWT amplifier, while for $v_t < 0$ the dispersion has negative slope at the original SIP angular frequency ω_{SIP}, and this regime could be used for low-threshold oscillators.

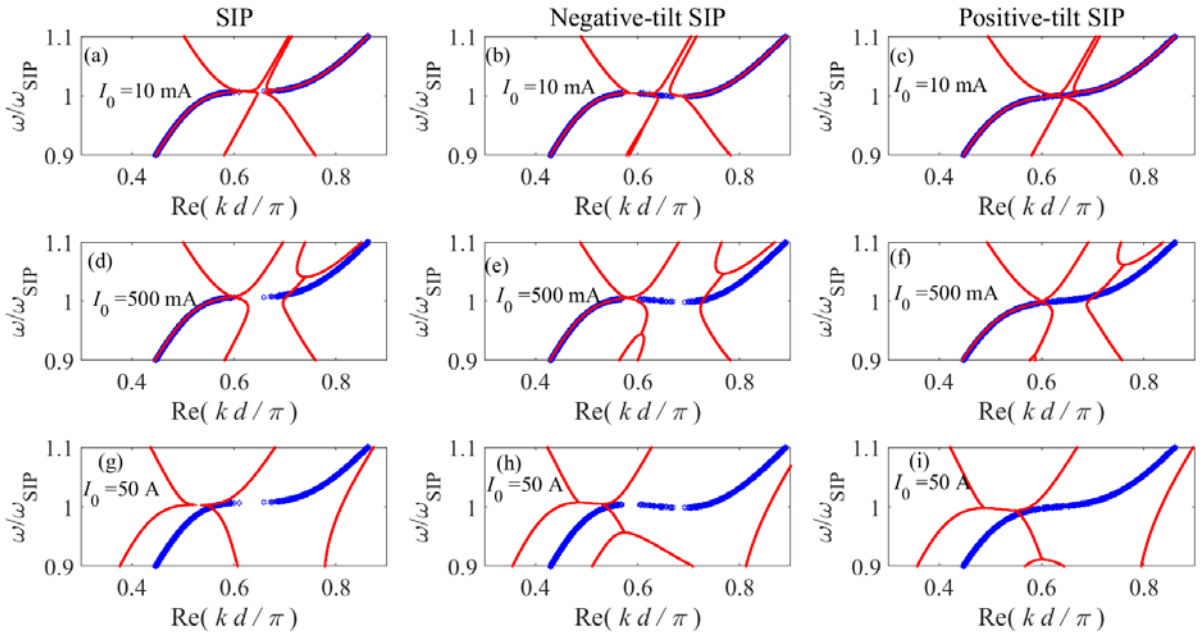

Fig. A1. Dispersion diagrams for the SWS-electron beam interactive "hot" system. In particular, we show the evolution of the *real* part of the complex Floquet-Bloch wavenumber k versus angular frequency for the three cases: ideal SIP, negative and positive tilted SIP, features for the cold SWS; considering different values of the beam current: for 10 mA in (a, b, c), for 500 mA in (d, e, f), and for 50 A in (g, h, i). The SWS structure is made of three CTLs. Solid red lines represent the dispersion of the interacting "hot" structure, whereas blue symbols represent the eigenmode with purely real wavenumber in the "cold" lossless SWS structure. This result is obtained by M. Othman.

Next, we analyze the interaction between the SWS made of three TLs with SIP and the electron beam through the modal dispersion diagram calculated using the state vector defined in (2.6) and the associated 8×8 transfer matrix $\underline{\mathbf{T}}$ for a unit cell as investigated thoroughly in [31]. Complex modes, i.e., modes with complex wavenumber k, are found by numerically solving $\det\left[\underline{\mathbf{T}}(z+d,z) - e^{-jkd}\underline{\mathbf{1}}\right] = 0$ that is equivalent to (2.8). In Fig. A1 we plot the complex dispersion diagram (red curves) of such interactive structures for three different values of electron beam currentI_0. Since we focus on amplification regimes we look for complex k solutions of (2.8) with real ω. Therefore, Floquet harmonics that provide

amplification along the positive z direction propagate as $\exp(-jkz)$ with $\mathrm{Im}(k) > 0$. In our CTL interacting with the electron beam there could be more than one eigenwave that contributes to amplification.

We consider three regimes of operations: an SWS with an SIP, and two others with positive and negative-tilt in the dispersion diagram of the "cold" SWS structure. Modes in the cold SWS are denoted with blue symbols. A strong interaction with electron beam occurs due to synchronization between the CTLs and electron beam around the SIP point $(\omega_{\mathrm{SIP}}, k_{\mathrm{SIP}})$ which results in the deformation of the dispersion curves as a function of the electron beam intensity. While in Fig. 2.6 we show the diagram for a wide frequency range, in Fig. A1 for clarity we show what happens around ω_{SIP} by plotting the real part of k in the normalized wavenumber range $0.35\pi < kd < 0.85\pi$, to show how modal curves deform and even split in that region. Notice how the SIP modes in the "cold" CTLs cases (curves with blue symbols) are deformed when the SWS interacts with the electron beam, and how this perturbation increases with increasing the beam current intensity. At each frequency, there are eight Floquet-Bloch modes solutions in the dispersion diagram for the "hot" SWS structure (i.e., the CTLs interacting with the beam), but only five complex ones are shown in Fig. A1 since the other three have negative $\mathrm{Re}(k)$. Three curves are originated by the SWS (i.e., from $D_{\mathrm{SWS}}(\omega, k)$ in (2.8)) and two are originated by the charge wave dispersion relation (i.e., $P_{\mathrm{beam}}(\omega, k)$ in (2.8)), but they are perturbed and connected to each other because of the term $C(\omega, k, I_0)$ on the right side of (2.8).

In some cases, only three distinct curves are visible, i.e., three values of $\mathrm{Re}(k) > 0$ at each frequency, which means in that case at least two curve-branches have two distinct values of $\mathrm{Im}(k)$, for the same value of $\mathrm{Re}(k)$.

For electron beam d.c. current $I_0 = 10$mA we see that the SIP condition (solid curves) in Fig. A1(a) has been deteriorated, compared to the "cold" CTLs (blue symbols), and the modes no longer satisfy the relation $\Delta\omega \sim (\Delta k)^3$ coming from (2.1) but rather a perturbed version given in (2.8). However, for frequencies away from the SIP (not shown in Fig. A1) the modes asymptotically approach those of the cold structure because waves in the CTLs are no longer synchronized with the electron beam. Increasing the beam average current I_0 results in higher deformation of the dispersion diagram (red curves), and for a current of $I_0 = 0.5$A the dispersion is so deformed that the original SIP of the "cold" structure cannot be recognized anymore. Interestingly (see for example the case of $I_0 = 50$A), a feature that resembles the SIP is present in the hot structure as seen in Fig. A1(g). However, the SIP in the hot structure is at a slightly different frequency and wavenumber compared to the one in the cold SIP (blue symbols).

The degree of amplification in the interacting periodic SWS is characterized by the imaginary part of the Floquet-Bloch wavenumber for the modes having Re(k) > 0 for an SWS with SIP interacting with an electron beam. We plot in Fig. A2 the scaling of the imaginary part of the Floquet-Bloch wavenumber with the beam current for the hot SWS-beam system, at the SIP angular frequency ω_{SIP} of the cold SWS. As explained there are five modes in Fig. A1 having Re(k) > 0, however in Fig. A2 we plot only the three, out of these five, that have Im(k) > 0, i.e., those that are amplified in their propagation along z. Thanks to the presence of the electron beam, the Floquet-Bloch wavenumber becomes complex for growing I_0 and it scales as $I_0^{1/3}$ as seen in Fig. A2 which signifies the strong amplification in the SWS for small beam current at SIP. Interestingly there is more than one eigenmode contributing to amplification, as was theorized in [31] though in this particular case one is

dominant for large beam current and follows an $I_0^{1/3}$ trend. Note that for higher current (outside the range shown in Fig. A2) the $I_0^{1/3}$ trend is ceased because of the high effect of perturbations, however such large beam current scheme can be exploited when losses are present (as in gain and loss balanced systems, see [52], [53]).

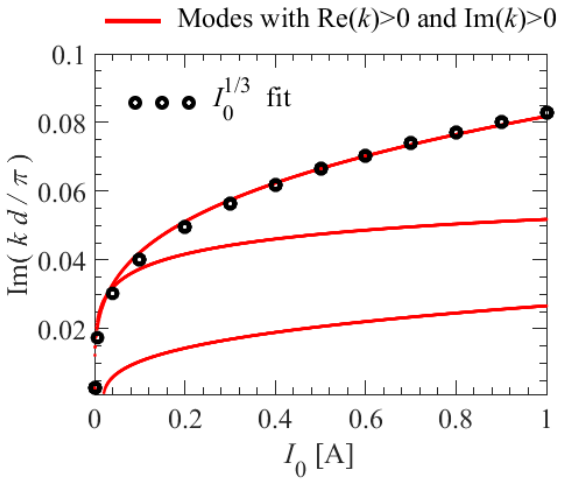

Fig. A2. Imaginary part of the Floquet-Bloch wavenumber, at fixed angular frequency, of the three amplifying modes having Re(k) > 0 and Im(k) > 0 of the "hot" SWS with SIP interaction with an electron beam varying as a function of the beam current. Note that there are five modes having Re(k) > 0, but only three of them provide amplification since they have Im(k) > 0. The chosen frequency of operation corresponds to that of the SIP frequency of the cold SWS. The imaginary part which is responsible for amplification for one of the modes grows with the beam current as $I_0^{1/3}$. This Result is obtained by, M. Othman.

Appendix B SWS and Beam Parameters Used in Simulations

We consider a periodic multiple transmission line model composed of unit cells having three CTLs. Each unit cell has the period of $d = d_A + d_B = 25$ mm and is made of two consecutive segments A with length d_A and B with length d_B, each made of three coupled TLs. The model is like the one in Sec. 2.4 of [31] with the only difference that here the CTLs is made of 3 TLs while in [31], [32] the CTLs was made of only 2 TLs, though the matrix

formalisms is the same. Therefore each 8 × 8 system matrix $\underline{\mathbf{M}}_A$ and $\underline{\mathbf{M}}_B$ in Sec. 2.4 of [31] includes 3 × 3 matrices representing distributed inductance $\underline{\underline{\mathbf{L}}}_m$, distributed capacitance $\underline{\underline{\mathbf{C}}}_m$, and distributed series capacitance $\underline{\underline{\mathbf{C}}}_{m,c}$ (assumed diagonal), where m = A, B. The distributed series capacitance is used to model the high pass feature associated to the presence of cutoff frequencies in a waveguide, as shown in Ch. 8 of [42] and in [31], [32]. A distributed series resistance matrix $\underline{\underline{\mathbf{R}}}_m$ (assumed diagonal) is used to represent Ohmic losses in the metal.

The values are obtained based on a cylindrical metallic waveguide geometry supporting three coupled modes and are selected such that the average characteristic impedance (defined as the average of the characteristic impedances of all the segments of the three TLs in each unit cell) is around 50Ω and develops an SIP around 1 GHz. Segment A of the CTLs has the length of d_A=10 mm and the following per unit length parameters: L_{A1}=0.56μH/m, L_{A2}=0.07μH/m, L_{A3}=0.74μH/m, C_{A1}=80.6 pF/m, C_{A2}=58 pF/m, and C_{A3}=151.6 pF/m. For the coupling parameters of segment A we have C_{A12}=22 pF/m, and C_{A23}=0.7 pF/m. Segment B has the length of d_B=15 mm and the following per unit length parameters: L_{B1}=0.99μH/m, L_{B2}=0.68μH/m, L_{B3}=1.24μH/m, L_{B12}=47 nH/m, L_{B13}=63 nH/m, L_{B23}=0.3μH/m, C_{B1}=387 pF/m, C_{B2}=258 pF/m, C_{B3}=339 pF/m, and C_{B12}=25 pF/m, C_{B23}=111 pF/m and C_{B13}=145 pF/m. It should be noted here that in the matrix form of the per unit length capacitances, non-diagonal (coupling) elements have the negative values as in equation (3.24) of [54]. The distributed series capacitances per unit length are C_{c1}=0.6 pF · m, C_{c2}=0.5 pF · m, and C_{c3}=1 pF · m, in both CTLs segments A and B. SWS Ohmic losses in the metal are accounted in the CTLs as series per unit length resistances of 5 Ω/m, in each of the 3 TLs, in both segments A and B.

For the SWS with tilted-positive dispersion diagram only a few parameters are different compared to ideal SIP in segment *B,* and have the values of L_{B12}=78 nH/m, L_{B13}=1 nH/m. For the SWS with tilted-negative dispersion diagram the only different values are L_{B12}=240 nH/m, L_{B13}=310 nH/m and C_{B13}=97 pF/m. The length of the SWS interacting with the electron beam is $L=Nd$ where N = 16 is the number of unit cells in every example, unless otherwise specified.

For the electron beam, in all the simulations we assume an average velocity of the electrons $u_0 = 0.3c$, therefore the beam voltage $V_0 = u_0^2/(2\eta) = 22{,}995V$, and we also assume the plasma angular frequency Ω_P=0 for simplicity. The threshold electron beam current to start oscillations in a SWS with ideal SIP is $I_{\text{th}} = 560\text{mA}$, whereas for a SWS with tilted-positive the starting electron beam current is $I_{\text{th}} = 880\text{mA}$. In both regimes of operations, the CTLs in Fig. 2.5 is terminated by $Z_{\text{s1}} = Z_{\text{L1}} = Z_{\text{L2}} = Z_{\text{L3}} = 75\Omega$, and the input terminals of the two lower TLs ($Z_{\text{s2}}, Z_{\text{s3}}$) are left open circuited. This loading has been used for all the results except for those in Figures 2.2, 2.3, 2.4 and 2.6.

The periodic single TL modeling a single mode TWT used for comparison is designed to have a unit cell with the same length as that of the SIP case (i.e., d = 25 mm) and same average characteristic impedance(50Ω) as the CTLs used for SIP schemes. Specifically, for comparison purposes we utilize a periodic TL since realistic TWTs are indeed constructed from periodic structures. This periodic single TL is composed of two segments *A* and *B* in each unit cell. The first segment has the physical length of d_{A}=10 mm and per unit length capacitance and inductance of C_A = 56.41 pF/m and L_A = 0.141μH/m and the second segment has the physical length of d_{B} =15 mm and per unit length capacitance and inductance of C_B = 564.1 pF/m and L_B = 1.41μH/m. Also, we are assuming the cut-off series

distributed capacitances of C_c = 0.12 pF $\cdot$ m in each segment and a series per unit length resistances of 5 Ω/m that represents losses. The starting electron beam current to start oscillations in a SWS made of a periodic single TL is $I_{\text{th}} = 4.7\text{A}$. Both ends of the single TL are terminated on $Z_s = Z_L = 75\Omega$ loads.

References

[1] A. S. Gilmour, *Klystrons, traveling wave tubes, magnetrons, crossed-field amplifiers, and gyrotrons*. Boston, MA: Artech House, 2011.

[2] E. Schamiloglu, *High-power microwave sources and technologies*. Wiley-IEEE Press, 2001.

[3] J. R. Pierce, *Travelling-wave tubes*. Van Nostrand; Macmillan, 1950.

[4] A. S. Gilmour, *Principles of traveling wave tubes*. Boston, MA: Artech House, 1994.

[5] H. A. Haus, "Electron beam waves in microwave tubes," in *Proc. Symp. Electronic Waveguides*, Polytechnic Institute of Brooklyn, 1958.

[6] L. J. Chu and J. D. Jackson, "Field theory of traveling-wave tubes," *Proc. IRE*, vol. 36, no. 7, pp. 853–863, 1948.

[7] L. M. Field, "Some slow-wave structures for traveling-wave tubes," *Proc. IRE*, vol. 37, no. 1, pp. 34–40, 1949.

[8] R. Kompfner, "The traveling-wave tube as amplifier at microwaves," *Proc. IRE*, vol. 35, no. 2, pp. 124–127, 1947.

[9] S. E. Tsimring, *Electron beams and microwave vacuum electronics*, vol. 191. Hoboken, NJ: John Wiley & Sons, 2006.

[10] V. Kesari and J. P. Keshari, "Interwoven-disk-loaded circular waveguide for a wideband gyro-traveling-wave tube," *Plasma Sci. IEEE Trans. On*, vol. 41, no. 3, pp. 456–460, 2013.

[11] R. C. Fletcher, "A broad-band interdigital circuit for use in traveling-wave-type amplifiers," *Proc. IRE*, vol. 40, no. 8, pp. 951–958, 1952.

[12] S. Bhattacharjee *et al.*, "Folded waveguide traveling-wave tube sources for terahertz radiation," *Plasma Sci. IEEE Trans. On*, vol. 32, no. 3, pp. 1002–1014, 2004.

[13] J. D. Wilson, "Electromagnetic field shaping for efficiency enhancement in terahertz folded-waveguide traveling-wave tube slow-wave circuit design," in *Vacuum Electronics Conference, 2007. IVEC'07. IEEE International*, 2007, pp. 1–2.

[14] Y. S. Tan and R. Seviour, "Wave energy amplification in a metamaterial-based traveling-wave structure," *EPL Europhys. Lett.*, vol. 87, no. 3, p. 34005, 2009.

[15] D. T. Lopes and C. C. Motta, "Characterization of Ring-Bar and Contrawound Helix Circuits for High-Power Traveling-Wave Tubes," *Electron Devices IEEE Trans. On*, vol. 55, no. 9, pp. 2498–2504, 2008.

[16] M. A. Shapiro, S. Trendafilov, Y. Urzhumov, A. Alu, R. J. Temkin, and G. Shvets, "Active negative-index metamaterial powered by an electron beam," *Phys. Rev. B*, vol. 86, no. 8, p. 085132, 2012.

[17] D. Shiffler, R. Seviour, E. Luchinskaya, E. Stranford, W. Tang, and D. French, "Study of Split-Ring Resonators as a Metamaterial for High-Power Microwave Power Transmission and the Role of Defects," *Plasma Sci. IEEE Trans. On*, vol. 41, no. 6, pp. 1679–1685, 2013.

[18] M. Zuboraj, N. Apaydin, K. Sertel, and J. L. Volakis, "Half-ring helical structure for traveling wave tube amplifiers," *IEEE Trans. Plasma Sci.*, vol. 42, no. 11, pp. 3465–3470, 2014.

[19] M. Zuboraj and J. L. Volakis, "Curved ring-bar slow-wave structure for wideband MW-power traveling wave tubes," *IEEE Trans. Plasma Sci.*, vol. 44, no. 6, pp. 903–910, 2016.

[20] E. Schamiloglu, "Dispersion engineering for high power microwave amplifiers", *Proc. EAPPC-Beams Conf.*, pp. 1-6, Sep. 2012.

[21] J. Benford, J. A. Swegle, and E. Schamiloglu, *High power microwaves*. Boca Raton, FL: CRC Press, 2015.

[22] V. A. Tamma and F. Capolino, "Extension of the Pierce Model to Multiple Transmission Lines Interacting With an Electron Beam," *IEEE Trans. Plasma Sci.*, vol. 42, no. 4, pp. 899–910, Apr. 2014.

[23] U. Chipengo, M. Zuboraj, N. K. Nahar, and J. L. Volakis, "A novel slow-wave structure for high-power K_ {a} band backward wave oscillators with mode control," *IEEE Trans. Plasma Sci.*, vol. 43, no. 6, pp. 1879–1886, 2015.

[24] S. C. Yurt, M. I. Fuks, S. Prasad, and E. Schamiloglu, "Design of a metamaterial slow wave structure for an O-type high power microwave generator," *Phys. Plasmas*, vol. 23, no. 12, p. 123115, 2016.

[25] J. S. Hummelt, X. Lu, H. Xu, I. Mastovsky, M. A. Shapiro, and R. J. Temkin, "Coherent Cherenkov-Cyclotron Radiation Excited by an Electron Beam in a Metamaterial Waveguide," *Phys. Rev. Lett.*, vol. 117, no. 23, p. 237701, 2016.

[26] U. Chipengo, N. K. Nahar, and J. L. Volakis, "Cold Test Validation of Novel Slow Wave Structure for High-Power Backward-Wave Oscillators," *IEEE Trans. Plasma Sci.*, vol. 44, no. 6, pp. 911–917, 2016.

[27] A. Figotin and I. Vitebskiy, "Electromagnetic unidirectionality in magnetic photonic crystals," *Phys. Rev. B*, vol. 67, no. 16, p. 165210, 2003.

[28] M. B. Stephanson, K. Sertel, and J. L. Volakis, "Frozen Modes in Coupled Microstrip Lines Printed on Ferromagnetic Substrates," *IEEE Microw. Wirel. Compon. Lett.*, vol. 18, no. 5, pp. 305–307, May 2008.

[29] N. Apaydin, L. Zhang, K. Sertel, and J. L. Volakis, "Experimental Validation of Frozen Modes Guided on Printed Coupled Transmission Lines," *IEEE Trans. Microw. Theory Tech.*, vol. 60, no. 6, pp. 1513–1519, Jun. 2012.

[30] H. Ramezani, S. Kalish, I. Vitebskiy, and T. Kottos, "Unidirectional Lasing Emerging from Frozen Light in Nonreciprocal Cavities," *Phys. Rev. Lett.*, vol. 112, no. 4, p. 043904, 2014.

[31] M. Othman, V. A. Tamma, and F. Capolino, "Theory and New Amplification Regime in Periodic Multi Modal Slow Wave Structures with Degeneracy Interacting with an Electron Beam," *IEEE Trans Plasma Sci*, vol. 44, no. 4, pp. 594–611, 2016.

[32] M. A. Othman, M. Veysi, A. Figotin, and F. Capolino, "Giant Amplification in Degenerate Band Edge Slow-Wave Structures Interacting with an Electron Beam," *Phys. Plasmas 1994-Present*, vol. 23, no. 3, p. 033112, 2016.

[33] M. A. Othman, M. Veysi, A. Figotin, and F. Capolino, "Low Starting Electron Beam Current in Degenerate Band Edge Oscillators," *IEEE Trans Plasma Sci*, vol. 44, no. 6, pp. 918–929, 2016.

[34] A. Figotin and I. Vitebskiy, "Slow light in photonic crystals," *Waves Random Complex Media*, vol. 16, no. 3, pp. 293–382, 2006.

[35] M. Othman and F. Capolino, "Demonstration of a Degenerate Band Edge in Periodically-Loaded Circular Waveguides," *IEEE Microw. Wirel. Compon. Lett.*, vol. 25, no. 11, pp. 700–702, 2015.

[36] J. Sloan, M. Othman, and F. Capolino, "Theory of Double Ladder Lumped Circuits with Degenerate Band Edge," *IEEE Trans. Circuits Syst. Regul. Pap.*, vol. 65, no. 1, pp. 3–13, Jan. 2018, doi: 10.1109/TCSI.2017.2690971.

[37] M. Y. Nada, M. A. K. Othman, O. Boyraz, and F. Capolino, "Giant Resonance and Anomalous Quality Factor Scaling in Degenerate Band Edge Coupled Resonator Optical Waveguides," *J. Light. Technol.*, vol. 36, no. 14, pp. 3030–3039, Jul. 2018, doi: 10.1109/JLT.2018.2822600.

[38] M. Veysi, M. A. K. Othman, A. Figotin, and F. Capolino, "Degenerate band edge laser," *Phys. Rev. B*, vol. 97, no. 19, p. 195107, May 2018, doi: 10.1103/PhysRevB.97.195107.

[39] M. A. K. Othman, F. Yazdi, A. Figotin, and F. Capolino, "Giant gain enhancement in photonic crystals with a degenerate band edge," *Phys. Rev. B*, vol. 93, no. 2, p. 024301, Jan. 2016.

[40] A. Figotin and I. Vitebskiy, "Slow wave phenomena in photonic crystals," *Laser Photonics Rev.*, vol. 5, no. 2, pp. 201–213, Mar. 2011.

[41] G. Mumcu, K. Sertel, and J. L. Volakis, "Lumped circuit models for degenerate band edge and magnetic photonic crystals," *Microw. Wirel. Compon. Lett. IEEE*, vol. 20, no. 1, pp. 4–6, 2010.

[42] R. F. Harrington, *Time-harmonic electromagnetic fields*. Piscataway, NJ: McGraw-Hill, 1961.

[43] A. Figotin and G. Reyes, “Multi-transmission-line-beam interactive system,” *J. Math. Phys.*, vol. 54, no. 11, p. 111901, 2013.

[44] J. R. Pierce, “Theory of the beam-type traveling-wave tube,” *Proc. IRE*, vol. 35, no. 2, pp. 111–123, 1947.

[45] V. A. Tamma, A. Figotin, and F. Capolino, “Concept for Pulse Compression Device Using Structured Spatial Energy Distribution,” *IEEE Trans. Microw. Theory Tech.*, vol. 64, no. 3, pp. 742–755, 2016.

[46] D. M. H. Hung *et al.*, “Absolute Instability near the Band Edge of Traveling-Wave Amplifiers,” *Phys. Rev. Lett.*, vol. 115, no. 12, p. 124801, 2015.

[47] P. A. Sturrock, “Kinematics of growing waves,” *Phys. Rev.*, vol. 112, no. 5, p. 1488, 1958.

[48] P. Huerre and P. A. Monkewitz, “Local and global instabilities in spatially developing flows,” *Annu. Rev. Fluid Mech.*, vol. 22, no. 1, pp. 473–537, 1990.

[49] R. J. Briggs, *Electron-stream interaction with plasmas*. Cambridge, MA: MIT Press, 1964.

[50] A. Bers, *Handbook of Plasma Physics*. New York: North-Holland, 1983.

[51] M. A. K. Othman, X. Pan, Y. Atmatzakis, and C. G. Christodoulou, “Experimental Demonstration of Degenerate Band Edge in Metallic Periodically-Loaded Circular Waveguide,” *IEEE Microw. Theory Tech.*, vol. 1611, no. 8, p. 9, 2017.

[52] M. A. Othman, F. Yazdi, and F. Capolino, “Exceptional points of degeneracy in coupled-mode periodic structures,” in *Electromagnetic Theory (EMTS), 2016 URSI International Symposium on*, 2, pp. 38–41.

[53] M. A. K. Othman and F. Capolino, “Theory of Exceptional Points of Degeneracy in Uniform Coupled-Waveguides and Balance of Loss and Gain,” *IEEE Trans. Antennas Propag.*, vol. 65, no. 10, pp. 1–15, 2017.

[54] C. R. Paul, *Analysis of Multiconductor Transmission Lines*, 2 edition. Hoboken, N.J: Wiley-IEEE Press, 2007.

CHAPTER 3

Third Order Modal Exceptional Degeneracy in *Parity-Time* Glide Symmetric Three-Way Microstrip Waveguide

Sec. 3.1 Motivation

The dispersion characteristics of microstrip structures can be engineered to exhibit exceptional modal characteristics, which can be exploited to design novel devices with improved features and enhanced performance for a wide variety of applications. Two coupled waveguides with *PT*-symmetry were known to exhibit second order exceptional point of degeneracy (EPD). In this work we introduce and investigate a particular class of EPD whereby three coupled waveguides satisfy *PT*-glide symmetry to exhibit a third order degeneracy in the dispersion relation. The proposed periodic structure is comprised of three microstrip coupled transmission lines (3CTLs) with periodically-spaced lumped loss/gain elements. The *PT*-glide symmetry condition allows three Floquet–Bloch

eigenmodes of the structure to coalesce at a given frequency. We show the novel design of such three-way microstrip device utilizing *PT*-glide symmetry and investigate the remarkable characteristics of the designs featuring third order EPDs. The proposed scheme may have diverse applications including but not limited to distributed amplifiers, radiating arrays, and sensors.

In this work we propose and investigate a novel periodic three-way waveguide design exploiting a *PT*-glide symmetric topology that exhibits a distinguished class of degeneracy condition based on three degenerate electromagnetic modes in the periodic microstrip structure. Degeneracies of eigenmodes in periodic structures were first investigated by Figotin and Vitebskiy in [1]–[6], demonstrating the existence of unique features associated with modal degeneracies. The EPDs associated to the coalescence of the modes is a relatively recent concept in the study of active devices. The interest in this class of degeneracies is mainly motivated by their relevance in the study of *Parity-Time-* (*PT-*) symmetric systems in physics [7]–[18]. The presented concept in this study exploits *PT*-glide symmetry in the design of novel devices which have enhanced properties. A periodic waveguide is said to possess glide-symmetry if it remains invariant under the glide operation, *G*, consisting of a translation by half of the geometrical period, *d*, followed by a reflection in the so-called glide plane [19], [20]. The occurrence of different exceptional points of degeneracies is not limited to lossless structures such as the ones in [1], [2], [14], [21]–[23] and, by proper balancing of the loss/gain, different EPDs can be achieved as well. Particularly, the balance of gain/loss can occur in coupled mode structures obeying the *PT*-symmetry [10], [11], [24].

The general subject of this chapter is the investigation of such modal degeneracy of a third order dictating the coalescence of three modes in periodic multimodal waveguides, typically referred to as *three-mode synchronization*, which has potential to demonstrate unique features compared to conventional devices [25]. In the vicinity of third-order EPDs in our dispersion diagram we observe that $(\omega - \omega_e) \propto (k - k_e)^3$, where ω_e is the angular frequency at which three modes coalesce and k_e is the Bloch wavenumber at the degeneracy point (note that $k_e \neq \pi/d$, meaning that the EPD does not occur at the band edge of the Brillouin zone). An illustration of an ideal dispersion relation exhibiting a third order EPD is shown in Fig. 3.1 (a) for a normalized case in which the real branches of an $\omega - k$ dispersion diagram (where k is the Bloch-wavenumber and ω is the angular frequency) is plotted and the coalescence of the modes is shown.

To realize a third order modal degeneracy in any periodic structure, three of the six modes must be periodically coupled in the structure. In [26], a multi-ladder lumped circuit model was shown to emulate dispersion diagram of third-order $\omega - k$ curve exhibiting a stationary inflection point (SIP). Our design of the periodic device, to achieve the third order modal degeneracy, is based on the serpentine structure introduced in [27] with three-way microstrip coupled transmission lines (3CTLs). In our study, we have modified the structure design by adding balanced gain and loss using a series of periodic line-to-ground admittances on the first (top) microstrip with conductance of $-G$ and another series of periodic line-to-ground admittances in the third (bottom) microstrip with the conductance of $+G$ to achieve a *PT*-glide symmetric design for the three-way microstrip structure as shown if Fig 3.1(b). The two line-to-ground admittances in each period are located at the uncoupled sections of the 3CTLs and are distanced by half a period from each

other, repeating with the same periodicity as the microstrip structure. The dimensions and other physical parameters of the device are then tuned and designed such that a third order EPD in its k-ω dispersion diagram is achieved.

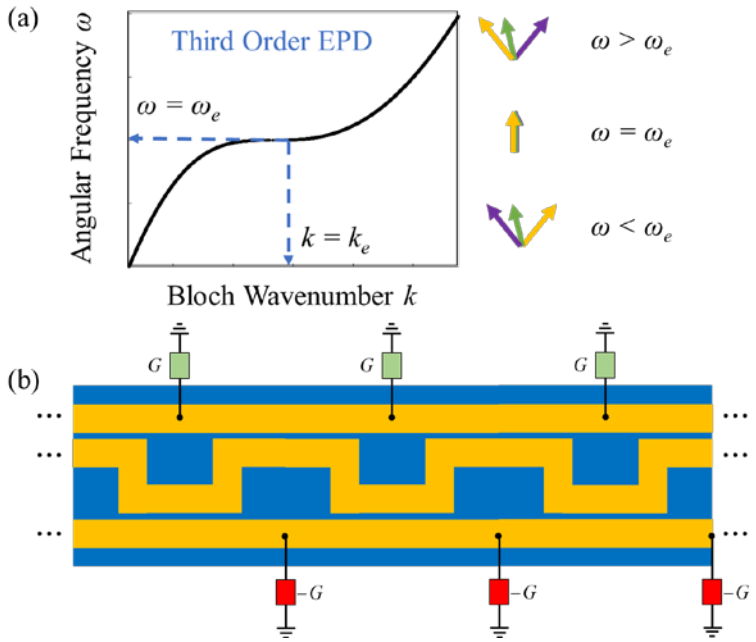

Fig. 3.1 (a) An example of the dispersion relation of an infinitely long periodic structure with three CTLs exhibiting third order modal degeneracy at angular frequency ω_e and the coalescence of the modes at the exceptional point of degeneracy where all three modes coalesce at the same point with $k = k_e$. (b) Proposed 3-way periodic microstrip structure featuring a third order EPD. The structure can be viewed as two transmission lines coupled through a third serpentine transmission line. The 3-way periodic structure supports three modes in each longitudinal direction; hence, it can be made to exhibit an EPD by properly designing and tuning the dimensions and values of the parameters.

The fundamental concept offered here is not limited to only one design or application. It can be potentially applied to a variety of periodic waveguide structures such as metallic waveguides [28] for high power microwaves [29]–[31], loaded transmission lines [32], and optical waveguides [33], [34].

The chapter is organized as follows: in Section 3.2 we introduce and discuss the unit cell structure and design of the three-way waveguide modeled with CTLs and the transfer matrix model of the unit cell. The modal dispersion of the periodic structure is investigated where we demonstrate the existence of third order EPDs in the dispersion diagram for a few different designs. We also provide a thorough analysis of the power distribution for the semi-infinite structure as well the engineering of the dispersion diagram to have different characteristics by tuning the design parameters of the unit cell. Section 3.3 is dedicated to the finite length studies of the periodic structure with proper terminations where we study the resonance behavior and stability through the *S*-parameters of the three-way waveguide. We also investigate the power performance of the finite-length structure for a distributed radiating amplifier application and its important characteristic aspects such as stability analysis and radiating and load power gains. Throughout this chapter we assume that the time-dependence is explicit in the form of $e^{j\omega t}$ and is suppressed thereafter.

Sec. 3.2 Periodic Three-way Coupled Waveguide

A. Unit Cell Design of the Coupled Serpentine Waveguide

We consider a periodic design in microstrip technology based on the three-way coupled transmission lines with the unit cell as shown in Fig. 3.2(a). The proposed design is modeled by two uniform transmission lines that are coupled through a third serpentine-shaped transmission line in the middle similar to [27]. The two top and bottom straight transmission lines are periodically loaded with two line-to-ground admittances, Y_1 and Y_2, with $Y_1 = -Y_2 = G$ to provide a *PT*-glide symmetric implementation as shown in the periodic structure of Fig 3.1(b) as well as the unit cell design of Fig 3.2(a), where *G* has a pure real

value representing loss and gain in the structure. The three-way structure supports three modes in each longitudinal direction. Thus, the structure is capable of exhibiting a third order EPD by tuning the microstrip geometry and admittances. In designing the unit cell to attain the EPD, for the sake of simplicity, it is assumed that all the transmission lines have the same width w, same separation distance between the coupled lines, s, and the length of each unit cell is set to d. We used a substrate with a relative dielectric constant of 2.2, no loss tangent ($\tan(\delta)=0$), and height of h_s = 1.575 mm. Also, the microstrip and ground plane metal layers were assumed to be lossless.

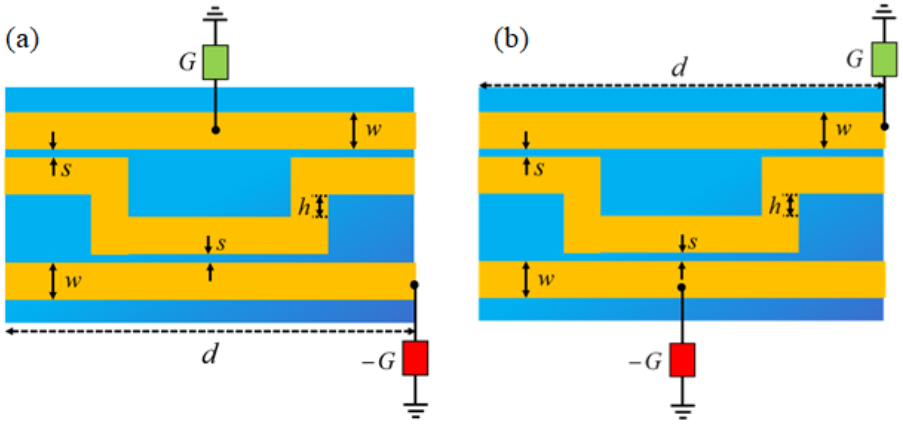

Fig. 3.2 Unit cell of the 3-way periodic microstrip structure that exhibits a third order degeneracy for Case *A* (used also in Secs. 3.3 and 3.4). The structure is composed of two uniform transmission lines coupled through a third serpentine transmission line in the middle, and two shunt conductances, gain and passive (e.g., a radiation resistance) added to the uncoupled sections with real positive and negative values as shown. (b) Unit cell of an alternative design (Case *B* and Case *C*) of the 3-way periodic microstrip structure where the shunt conductances (gain and loss) are added to the coupled sections instead.

To achieve the degeneracy condition at the desired frequency (f_e = 2 GHz), we fixed values for some of the dimensions including w = 5 mm for the lines' widths (corresponding to lines with 50 Ohm) and s = 0.5 mm for the distancing between the lines. We then tune

other dimensions such as the length of the unit cell, d, the height of the serpentine section, h, and the value of the conductance, G, to search for the third order degeneracy at the desired frequency. The optimization we have done to find SIP is based on tuning the prementioned parameters to minimize the coalescence parameter associated with three eigenmodes in the system as discussed later.

B. Transfer Matrix Formalism

In our analysis, we will use the 3CTLs 1-D transfer matrix formalism to construct the total transfer matrix for a single unit-cell. We will also use this transfer matrix in our analysis of the finite-length periodic structure composed of cascaded unit cells in order to model and investigate the various aspects of the modal degeneracy under study. The details of the transfer matrix formalism are provided in Appendix B.

In the investigation of the EPDs' properties through transfer matrix and eigenvalues for a 6-port system, it is usually convenient to define the position-dependent state-vector in the form:

$$\boldsymbol{\Psi}(z) = [V_1(z), I_1(z), V_2(z), I_2(z), V_3(z), I_3(z)]^T, \tag{3.1}$$

including the voltage and current vectors at any point, z, on the three TLs which describe the evolution of the eigenmodes as they propagate through the structure. A *transfer matrix*, $\underline{\mathbf{T}}(z_2, z_1)$, is defined which uniquely relates the state vector $\boldsymbol{\Psi}(z)$ between two points in the structure such that:

$$\boldsymbol{\Psi}(z_2) = \underline{\mathbf{T}}(z_2, z_1)\boldsymbol{\Psi}(z_1), \tag{3.2}$$

where we use the forward transfer matrix notation with $z_2 > z_1$ along the z axis. The transfer matrix $\underline{\mathbf{T}}_U$ of a unit cell shown in Fig. 3.2(a), is then defined as $\boldsymbol{\Psi}(z + d) = \underline{\mathbf{T}}_U\boldsymbol{\Psi}(z)$

and is expressed and calculated in terms of the geometric and electrical parameters of the unit cell using formulas found in Appendix B. Accordingly, the unit cell transfer matrix for the waveguide in Fig. 3.2(a) is obtained by cascading the transfer matrices of each segment of the unit cell:

$$\underline{\mathbf{T}}_U = \underline{\mathbf{T}}_{-G}\underline{\mathbf{T}}_{A3}\underline{\mathbf{T}}_{cor}\underline{\mathbf{T}}_{B3}\underline{\mathbf{T}}_{+G}\underline{\mathbf{T}}_{B3}\underline{\mathbf{T}}_{cor}\underline{\mathbf{T}}_{A3}. \tag{3.3}$$

The expression for unit cell transfer matrix for Fig. 3.2(b) is presented in Appendix A. For an infinitely long stack of CTL unit cells, a periodic solution for the state vector $\boldsymbol{\Psi}(z)$ exists in the Bloch form and the transfer matrix $\underline{\mathbf{T}}_U$ translates the state vector across a unit cell as the eigenvalue equation of

$$\underline{\mathbf{T}}_U\boldsymbol{\Psi}(z) = e^{-jkd}\boldsymbol{\Psi}(z), \tag{3.4}$$

where k is the complex-valued Bloch wavenumber. The eigenvalues of the transfer matrix and hence the Bloch wavenumber are obtained as solutions of the characteristic equation

$$\mathrm{Det}(\underline{\mathbf{T}}_U - \zeta\underline{\mathbf{I}}) = 0, \tag{3.5}$$

in which we define $\underline{\mathbf{I}}$ to be the 6×6 identity matrix. For the CTL with three lines (6×6 transfer matrix) discussed in this study, six eigenvalues $\zeta_i = e^{-jk_i d}$, $i = 1, 2, \ldots, 6$, of the $\underline{\mathbf{T}}_U$ matrix is calculated from equation (3.5).

C. Dispersion Relation Featuring Third Order EPD

The periodic three-way microstrips in Fig. 3.2 are able to support a third order degeneracy. We design three different CTLs (Cases *A*, *B*, *C*) where the EPD occurs at an operating frequency of 2 GHz. Our unit cell designs have been determined by using the fixed parameters provided in Appendix A, such as the microstrip width, spacing between coupled microstrips, substrate dielectric properties, and substrate thickness. We then

tuned the other parameters such as the length of the unit cell d, the "height" h of the serpentine sections, and the choice of lumped gain and loss conductances G and $-G$, respectively, to obtain EPDs at a desired frequency. Both the EPD frequency and the flatness of the dispersion curve in the vicinity of the degeneracy condition can be altered by tuning the dimensional and electrical parameters of the unit cell.

An EPD is represented by the coalescence of the eigenvalues (i.e., wavenumbers) and by the coalescence of the eigenvectors (i.e., polarization states). The coalescence of the eigenvalues is necessary to have an EPD, however, the coalescence of the eigenvector guarantees the existence of an EPD. In the following we assess the occurrence of a third order EPD by observing the coalescence of three eigenvectors. Accordingly, we defined a figure of merit to measure how close the system is to an ideal third order degeneracy condition at the frequency of interest, called *Coalescence Parameter* (C_{EPD}). This concept was developed in [35] for a fourth order degeneracy, and used also in [27] for a third order degeneracy called stationary inflection point (SIP); it is here analogously defined for a third-order EPD as:

$$C_{EPD} = \frac{1}{3}\sum_{\substack{m=1,n=2 \\ n>m}}^{3} |\sin(\theta_{mn})|\,, \cos(\theta_{mn}) = \frac{\mathrm{Re}|(\boldsymbol{\Psi}_m, \boldsymbol{\Psi}_n)|}{\|\boldsymbol{\Psi}_m\|\|\boldsymbol{\Psi}_n\|}, \tag{3.6}$$

where θ_{mn} represents the angle between two eigenvectors $\boldsymbol{\Psi}_m$ and $\boldsymbol{\Psi}_n$ in a six-dimensional complex vector space, with norms $\|\boldsymbol{\Psi}_m\|$ and $\|\boldsymbol{\Psi}_n\|$, and $(\boldsymbol{\Psi}_m, \boldsymbol{\Psi}_n)$ is their inner product. The coalescence parameter defined in equation (3.6) is always positive, with small values indicating how well the eigenvectors of the structure are close to each other in the frequency range of interest. EPDs of third order occur when $C_{\mathrm{EPD}} = 0$. Using this coalescence parameter as the error function to be minimized at the EPD frequency of interest, an

optimization algorithm in MATLAB was used to select the conductance of the lumped elements, serpentine height h, and period of our unit cell d in order to make it exhibit an EPD of third order.

We provide three examples of EPDs that occur in three-way microstrip waveguides as in Fig. 3.2, denoted as Cases *A*, *B* and *C*. These cases were each found using the optimization method discussed above.

Case A: In this example, the tuned unit-cell parameters were found to have a conductance value of G = 0.1398 S (or equivalently R =1/G= 7.15 Ω), serpentine height of h = 5.35 mm, and period of d = 54.15 mm. The active (gain) and passive conductances in this case are located on the unit cell as illustrated in Fig. 3.2(a). Fig 3.3 shows the existence of third order degeneracy in the dispersion diagram and the coalescence parameter. The Imaginary part of the dispersion diagram is plotted versus the Real part in Fig. 3.3(a) where it shows the existence of third order degeneracy condition and the coalescence of the three modes at two different locations in the fundamental Brillouin zone, at k_e and $-k_e + 2\pi/d$ because of reciprocity. In other words, we show an EPD in the region $0 < kd < \pi$, in the dispersion diagram of Fig 3.3(c). There are three coalescing branches, one (in solid black) has a purely real wavenumber with positive group velocity for frequencies around the EPD frequency as can be seen by the black curve on the left side of Fig 3.3(c). The second EPD is in the region $\pi < -kd + 2\pi < 2\pi$, where there are three coalescing branches. One branch (solid black) has a purely real wavenumber with negative group velocity for frequencies around the EPD. Through the rest of the chapter we consider the mode in the region $0 < kd < \pi$ as our EPD of the interest associated with forward waves in our dispersion diagram.

In Fig. 3.3 (b) the Coalescence Parameter is plotted versus normalized frequency around ω_e, to demonstrate how close we are to the third order degeneracy condition in our design. And finally, in Fig. 3.3(c) and (d) we plot the conventional modal dispersion diagram of the infinite structure, showing both the real and imaginary parts of the normalized complex Floquet–Bloch wavenumber k versus normalized angular frequency around the designed frequency ω_e where the third order behavior is observed. We used dashed lines in Fig. 3.3(c) and (d) for wavenumbers that are complex-valued in order to show different overlapping curves of real and imaginary parts. In other words, the curves with dashed lines of different colors represents two overlapping branches. We follow the same way in Fig. 3.4 and Fig. 3.5.

It is worth noting that the normalized dispersion relation around the desired third order EPD can be approximated using the normalized third order equation of:

$$(\omega/\omega_e - 1) \approx \zeta(kd/\pi - k_e d/\pi)^3 \tag{3.7}$$

where ω_e is the angular frequency at which three modes coalesce and k_e is the Floquet-Bloch wavenumber at the degeneracy point. The nondimensional parameter ζ determines the flatness of the normalized dispersion at the EPD which is the third derivative of $d^3\omega \,/\, dk^3$ around the degeneracy point and based on the normalization is unit-less. Lower values of the flatness factor ζ means flatter dispersion relations at the EPD which is an important factor in designing for different applications based on the desired characteristics and properties. For the Case *A* shown in Fig. 3.3 the flatness factor is calculated as: $\zeta_A \approx 2.1$.

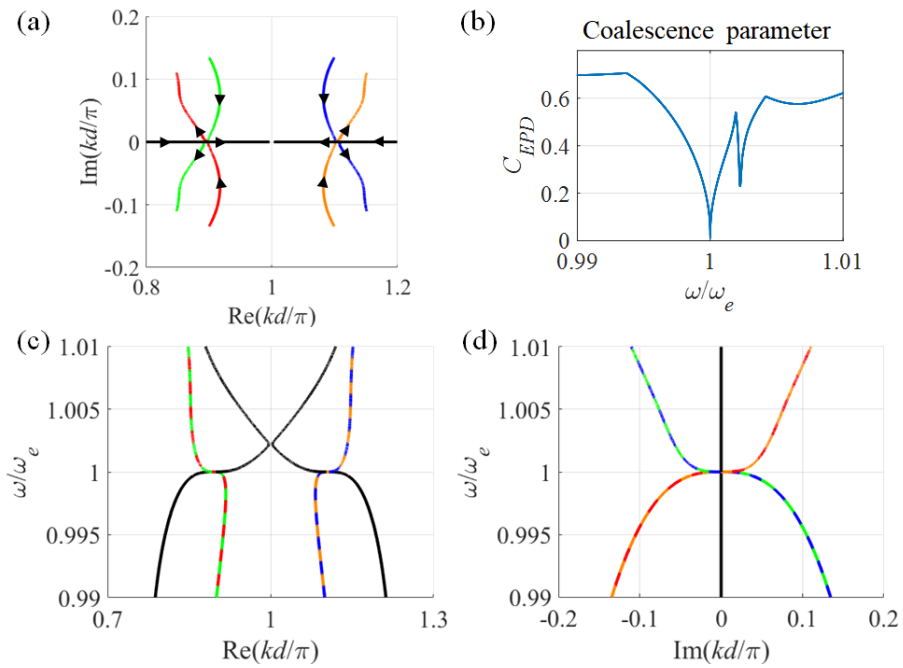

Fig. 3.3 (a) Case *A*: complex wavenumber plotted in the complex k plane varying frequency. This plot shows the existence of the third order modal degeneracy condition and coalescence of the three modes at two different EPD wavenumbers, k_e and $-k_e + 2\pi/d$. (b) Coalescence parameter plotted versus normalized frequency in the vicinity of the EPD. (c) and (d) Typical modal dispersion diagram of the eigenmodes, showing both the real and imaginary parts of the normalized complex Floquet–Bloch wavenumber k versus normalized angular frequency around the EPD frequency ω_e. The purely real branches of the dispersion diagram are shown in solid black. Dashed-line dispersion branches represent the modes with complex wavenumber, using the same colors as in (a). Besides the lumped elements, the structure is lossless for all the graphs shown in this figure. This Result is obtained by T. Mealy and F. Yazdi.

Case B: Using the same optimization method, we find additional solutions which exhibit third order modal degeneracy. The unit cell design of Case *B* differs from that of Case *A* in that the lumped elements are positioned in the center of the coupled sections of transmission line, as is illustrated in Fig. 3.2(b). For this second solution, the tuned unit-cell was found to have the conductance value of G = 0.105 S (or equivalently R =1/G= 9.5 Ω), serpentine height of h = 6.36 mm, and period of d = 46.3 mm. Similar to the previous case,

the dispersion diagrams and coalescence parameter are plotted in Fig. 3.4, where we show the existence of the EPD for the new values and discuss its modal behavior. For the Case *B* shown in Fig. 3.4, the flatness factor is calculated as $\zeta_B \approx 7.2$ which is higher than Case *A*, meaning a narrower dispersion diagram compared to the previous case (i.e., less flat).

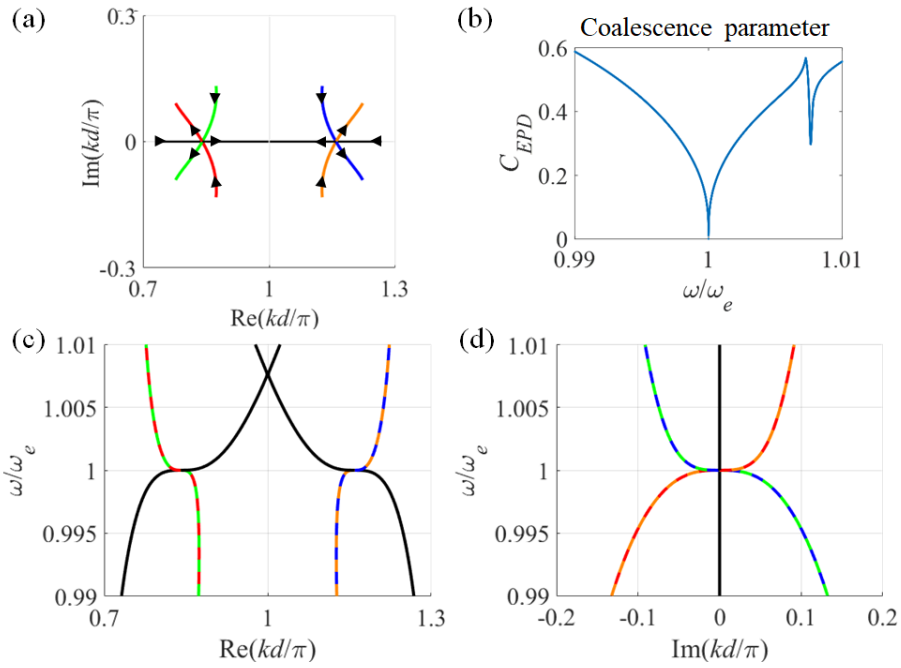

Fig. 3.4 (a) Case *B*: complex wavenumber plotted in the complex k plane varying frequency. This plot shows the existence of the third order modal degeneracy condition and coalescence of the three modes at two different EPD wavenumbers, k_e and $-k_e + 2\pi/d$. (b) Coalescence parameter plotted versus normalized frequency in the vicinity of the EPD. (c) and (d) Typical modal dispersion diagram of the eigenmodes, showing both the real and imaginary parts of the normalized complex Floquet–Bloch wavenumber k versus normalized angular frequency around the EPD frequency ω_e. The purely real branches of the dispersion diagram are shown in solid black. The circles represent branches with two modes (curves). Dashed-line dispersion branches represent the modes with complex wavenumber, using the same colors as in (a). Besides the lumped elements, the structure is lossless for all the graphs shown in this figure. This Result is obtained by T. Mealy and R. Marosi.

Case C: To show the flexibility of our design we have provided a third solution that exhibits third order modal degeneracy in its dispersion diagram by again tuning the

dimensions around initial values which seem appropriate for a practical design and search for a new set of parameters to achieve the third order EPD.

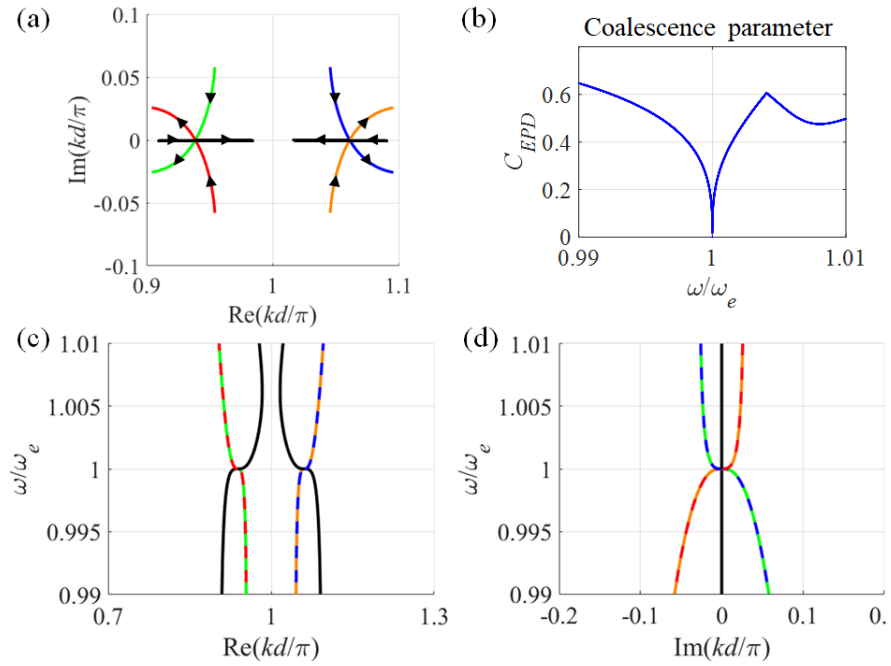

Fig. 3.5 (a) Case *C*: complex wavenumber plotted in the complex k plane varying frequency. This plot shows the existence of the third order modal degeneracy condition and coalescence of the three modes at two different EPD wavenumbers, k_e and $-k_e + 2\pi/d$. (b) Coalescence parameter plotted versus normalized frequency in the vicinity of the EPD. (c) and (d) Typical modal dispersion diagram of the eigenmodes, showing both the real and imaginary parts of the normalized complex Floquet–Bloch wavenumber k versus normalized angular frequency around the EPD frequency ω_e. The purely real branches of the dispersion diagram are shown in solid black. Dashed-line dispersion branches represent the modes with complex wavenumber, using the same colors as in (a). Besides the lumped elements, we have assumed the structure to be lossless for all the graphs shown in this figure. This Result is obtained by T. Mealy and R. Marosi.

The tuned unit-cell parameters were found to be a conductance value of G = 0.0099 S (or equivalently R =1/G= 100.55 Ω), serpentine height of h = 1.07 mm, and period of d = 48.08 mm. As in Case *B*, the lumped elements are centered in the CTL sections, as illustrated in Fig. 3.2(b). The existence of the third order EPD for this case is shown in the results of the

Fig. 3.5, where we have plotted the dispersion diagram and the coalescence parameter in a fashion similar to the previous cases. For the Case C shown in Fig. 3.5, the flatness factor is calculated as $\zeta_C \approx 188$ which is much higher than the two previous Cases A and B indicating a more-narrow EPD in the dispersion diagram, as can be seen from the results in Fig. 3.5.

These three different solutions show that our design to achieve the third order modal degeneracy in the 3CTL is flexible and the parameters of interest can be tuned around some initial practical values and based on the application.

D. Engineering of the Dispersion Diagram

One of the interesting features of the designs that we propose, which exhibit having third order modal degeneracy around the desired frequency, is that the slope of the dispersion diagram can be tuned easily by altering one or more the design parameters of the unit cell to have slightly positive slopes (small positive group velocity) or slightly negative slopes (small negative group velocity) rather than the ideal case of zero slope at the ideal third order EPD. In Fig. 3.6(a) we show how the slope of the dispersion diagram for Case A, can be engineered to have positive/negative slopes in the vicinity of the EPD by adjusting the value of the $R = 1/G$. We observe a slightly positive slope for slightly lower values of R (R = 5.27 Ω) shown in solid blue, and a slightly negative slope for slightly higher values of R (R = 9.11 Ω) shown in solid red, as compared to the ideal third order EPD design for Case B with zero slope and R = 7.15 Ω , shown in solid black in Fig 3.6(a). In this figure we only show the branches with purely real wavenumber, i.e., those with complex-valued k are not shown for simplicity.

Another method to alter the slope of the dispersion diagram in the vicinity of the third order degeneracy is by tuning the height of the serpentine microstrip (h) as shown in Fig. 3.6(b). Note that by just altering h, the structure remains PT-glide symmetric. As observed from the results of Fig. 3.6(b), by slightly lowering the height (h = 4.748 mm) we achieve slightly positive slope (shown in solid blue) and by slightly increasing the height (h = 5.948 mm) we achieve slightly negative slope (shown in solid red) for the dispersion diagram of the Case A where the ideal EPD with zero slope occurs for h = 5.348 mm. Instead, by slightly increasing the height (h = 5.948 mm) we achieve slightly negative slope (shown in solid red).

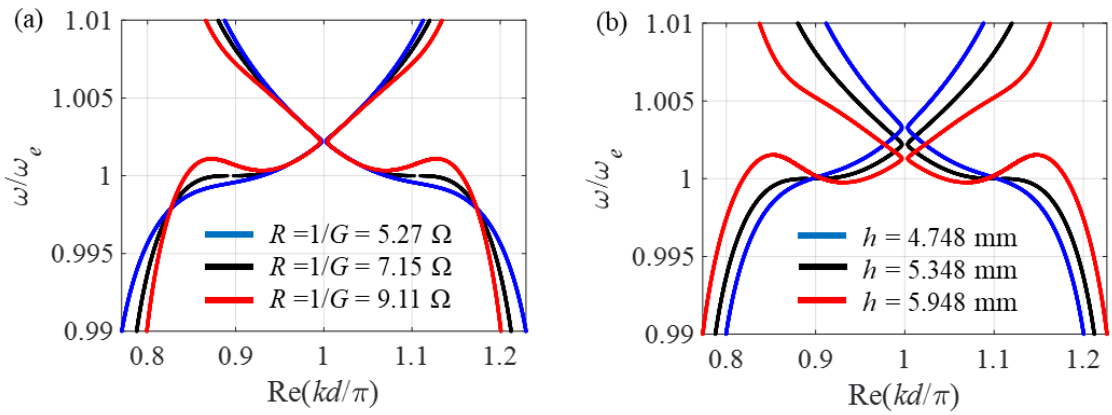

Fig. 3.6 Engineering of the dispersion diagram to exhibit different group velocities (different slopes) around ideal EPD.

(a) By tuning the value of the R (or G) elements for Case A where we observe a slightly positive slope for R = 5.27Ω and a slightly negative slope for R = 9.11Ω where the ideal case with zero slope has R = 7.15Ω.
(b) By tuning the value of the h (serpentine height) for Case A where we observe a slightly positive slope for h = 4.748 mm and a slightly negative slope for h = 5.948 mm where the ideal case with zero slope has h = 5.948 mm. For all the graphs shown above only the purely real branches of the dispersion diagram are plotted and we have assumed the structure to be lossless. This result is obtained by F. Yazdi.

The results of the dispersion engineering example demonstrate the flexibility of the proposed design for specific applications where the group velocity can be tuned by varying the design parameters about their nominal values. Increasing the slope of the dispersion diagram around the EPD frequency to reach a positive group velocity, will potentially increase the bandwidth of the resonance peak associated to EPD, which will be desirable for reaching higher bandwidths in wide-band amplifier applications. Alternatively, decreasing the slope to negative values in the dispersion diagram around EPD results in higher Q-factors for the EPD resonance peak [25], which may be beneficial for backward wave oscillator applications.

E. Power Analysis based on Modes around EPD

Exactly at EPD ($\omega = \omega_e$), where three modes coalesce in their wavenumber $k_1 = k_2 = k_3 = k_e$, with k_e purely real (Im(k_e)=0), there is no exponentially growing or decaying behavior in the eigenwaves propagating through the unit cells. We checked this by using the single degenerate eigenvector as input state-vector in a semi-infinite structure i.e., $\mathbf{\Psi}(z = 0) = \mathbf{\Psi}_e$. This investigation of the power flow in the semi-infinite long periodic structure shows that the power over G and $-G$ is balanced, meaning they both have equal powers that cancel one another (i.e. $P_{-G} = -P_G$).

By perturbing the frequency to be slightly lower or higher than the EPD frequency, the three modes are slightly perturbed from the EPD and they are no more coalescing. When the frequency is higher or lower than the EPD one, one mode has a purely real wavenumber (black curves in Fig. 3.3, 3.4 and 3.5), k_1, but the other two modes are

complex conjugates of each other (k_2, and $k_3 = k_2^*$ in the very close neighborhood of the EPD, red and green curves in Fig. 3.3, 3.4 and 3.5). One (red curve) of those two modal complex wavenumbers has Im(k_2) < 0 for $\omega < \omega_e$ whereas it has Im(k_2) > 0 for $\omega > \omega_e$. The other mode has $k_3 = k_2^*$ in the frequency range very close to the EPD. For the purely real mode, k_1, there is no growing/decaying behavior in the signal and the power is balanced. The mode with Im (k_2) > 0 has a growing behavior in the signal over the unit cells moving from left to right. For this case there is more power provided by $-G$ (gain) than the one consumed by $+G$ (loss). On the other hand, the mode with negative imaginary part (k_3), has a decaying behavior in the signal and in this case, there is more power consumed by $+G$ (loss) than the one provided by $-G$ (gain). A graphical summary of this investigation is presented in Fig. 3.7(a) where for each of the three modes associated to a perturbed third order EPD, the propagating, growing, and decaying modes are shown. At the EPD the three aforementioned modes coalesce together to form one degenerate mode with a purely real $k = k_e$.

In order to better understand the power distribution inside the unit cells, we consider Case A in Fig. 3.7(b) the power over the three lines of the semi-infinite long periodic structure is plotted versus normalized z, evaluated exactly at EPD frequency and wavenumber such that $0 < kd < \pi$. The plot was obtained by assuming an input state vector at z = 0 equal to be the EPD degenerate eigenvector, $\mathbf{\Psi}(z = 0) = \mathbf{\Psi}_e$, associated with positive value of $k < \pi/d$. In Fig. 3.7(c) the total power (summation of the powers for three lines of the circuit, top, middle, and bottom) is plotted versus frequency where we observe two different jumps in the power in each period that are associated to the power dissipation and contribution of the $+G$ and $-G$ elements to the circuit, respectively. Since

the powers are evaluated exactly at EPD condition with purely real modes, the power over $+G$ and $-G$ is balanced with $P_{-G} = -P_G$. The conservation of the power is also verified in our numerical simulations.

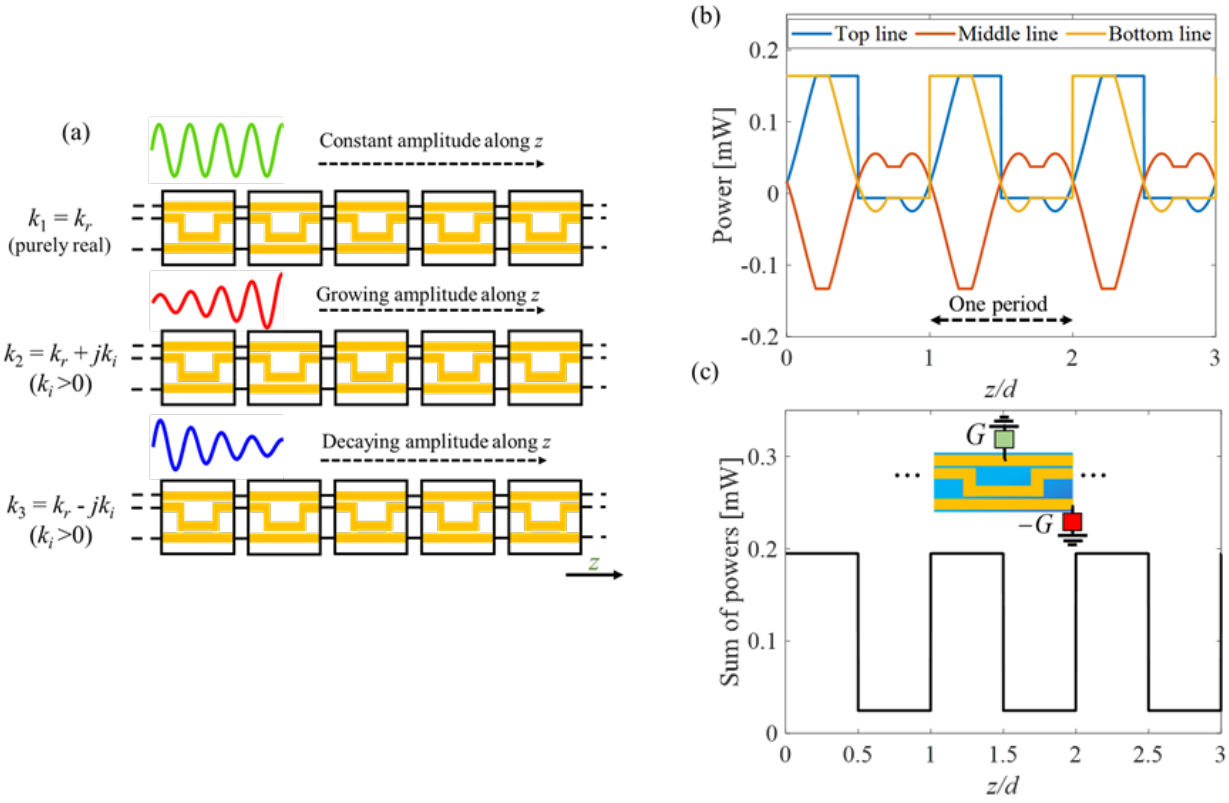

Fig. 3.7 (a) Graphical representation of how the signal/power propagates inside the periodic structure moving along $+z$ for three different cases of: (i) purely real (k_1), (ii) complex wavenumber with positive imaginary part (k_2), and (iii) complex wavenumber with negative imaginary part (k_3). The propagating, growing and decaying cases are shown as discussed (b) Power (in mW) over the three lines of the infinitely long periodic structure plotted versus z evaluated exactly at EPD frequency for the design of Case A for the EPD is in the region $0 < kd < \pi$. This plot exhibits how the power moves over the structure for any specific mode and for each line of the three-way waveguide. (c) Summation of the powers (in mW) of the three lines shown in part (b) plotted versus z for the infinitely long periodic circuit. The jumps in the power are associated to the $+G$ and $-G$ contributions. This Result is obtained by F. Yazdi and T. Mealy.

We have selected case *A* for demonstration purposes in Fig. 3.7(b) and Fig. 3.7(c), but the general concept of the power analysis provided here is the same for our other cases featuring third order EPDs. This study provides us with some insight on how different modes behave and how the signal/power is moving throughout the structure. In the following section we will provide more investigation of the powers and gain for the finite-length and terminated periodic structure.

Sec. 3.3 Finite-Length Structure: Properties and Performance

As discussed earlier, devices featuring EPD may exhibit extraordinary properties and enhanced characteristics which makes them potential candidates for various applications. To provide an example application of the regime presented in this chapter, we consider the finite-length three-way waveguide constructed by cascading the proposed *PT*-glide symmetric unit cells and adding proper excitation and terminations to make a distributed amplifier, with the $-G$ as distributed gain and with the $+G$ elements as radiative loads (modeling antennas). In this section, we first provide an investigation of the resonance behavior and stability analysis of such finite three-way waveguides and then show the amplification at the EPD frequency.

A. Resonance Behavior and Stability Analysis

We consider the three-way waveguide structure of Case *A* in Fig. 3.2(a), consisting of N cascaded unit cells as depicted in Fig. 3.8(a). We have omitted the right-most $-G$ element, as shown, to make the terminated structure symmetric and also help to improve stability. As shown in Fig. 3.8(a), we excite the middle line of the 3CTLS with terminations of $Z_s = Z_L = 50$ Ω. For the terminals of the bottom line, we are assuming $Z_y = 50$ Ω, and for the top line we

are assuming short circuit terminations ($Z_x = 0\ \Omega$) as shown in Fig. 3.8(a). We have selected this loading scenario based on the stability and gain performance of the three-way structure.

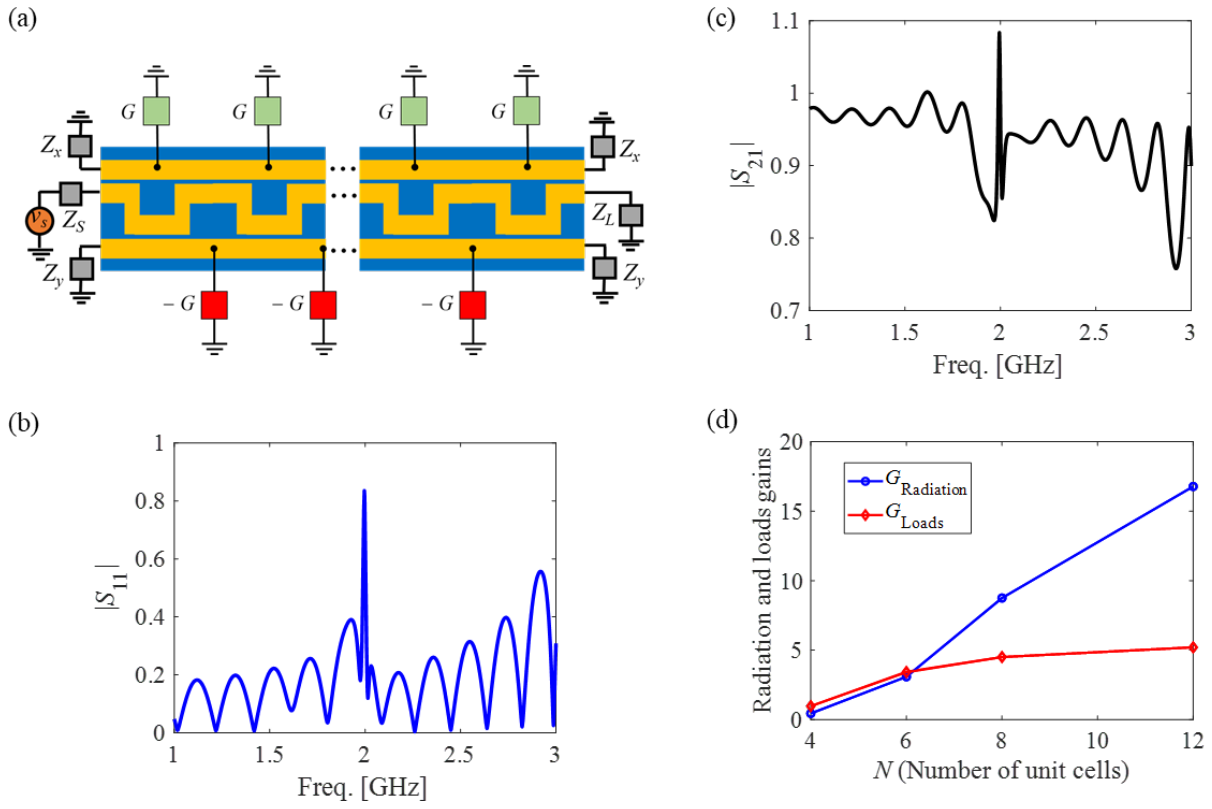

Fig. 3.8 (a) Finite-length three-way structure with period d made by cascading the unit cells treated as a 6-port network that models wave propagation in the waveguide discussed in Section II with the total length of $L = Nd$, including loading and excitation. (b) $|S_{11}|$ and (c) $|S_{21}|$ for the finite length structure of Case A with N=8 unit cells and $\tan(\delta)$=0 plotted versus frequency around EPD frequency, where we could achieve $|S_{11}|<1$ and the stability is confirmed. (d) The radiation gain and loads gain (both linear scale) versus the length of the finite structure (N) evaluated at the peak frequency nearest to the EPD for the finite structure of Case A with $\tan(\delta)$=0. For all results shown above we have assumed $Z_y = Z_s = Z_L = 50\Omega$ for the bottom and middle lines, and short circuit for the top lines ($Z_x = 0\ \Omega$). The result is obtained by A. Nikzamir and F. Yazdi.

First to check the stability and the resonance behavior, we check the S parameters. Based on [36], for two port networks, oscillations are possible when either the input or output port present a negative resistance, which occurs when $|S_{11}|>1$ or $|S_{22}|>1$ in our structure setup, treated as a two port network (because of symmetry, $S_{11} = S_{22}$). To check the stability, we need to evaluate the S_{11} and S_{22} for the waveguide. For the design of Case *A*, the results for S_{11} and S_{21} parameters, assuming $N = 8$ unit cells and lossless structure (besides the lumped elements), is provided in Fig. 3.8(b) and (c) over a wide frequency range. The structure is stable based on the S_{11} response shown in Fig. 3.8(b). For other configurations or loading scenarios, the stability can also be reached by using impedance matching circuits (filters).

The S_{21} parameter plotted in Fig 3.8(c) for the finite-length structure versus frequency shows a sharp resonance peak denoted by ω_r associated to the designed third order EPD frequency of 2 GHz. By increasing the number of unit cells (N), the resonance peak nearest to EPD becomes sharper.

B. Gain Evaluation

To evaluate of the behavior of the proposed distributed amplifier, we consider the power delivered to the loads (Z_L and Z_y) as well as the power delivered to all N passive elements ($+G$) for different structure lengths. We calculate the load power gain (G_{Loads}) and radiation power gain ($G_{Radiation}$). In our analysis, the load gain is defined as $G_{Loads} = P_{Loads\text{-}total} / P_{in}$ in which $P_{Loads\text{-}total}$ is summation of the power over Z_L and the two Z_y and P_{in} is the input power at the second (middle) line input. The radiation gain is defined as $G_{Radiation} = P_{Radiation\text{-}total} / P_{in}$, in which $P_{Radiation\text{-}total}$ is the summation of the powers delivered to the $+G$ elements

and P_{in} is the input power at the second (middle) line input. All the other parameters are the same as previously discussed for Case *A*.

In Fig 3.8(d), the radiation gain and load gain are plotted versus the length of the finite-length structure (N) at the strong-peak resonance frequency nearest to the third order EPD in Case *A*, still assuming lossless structure (the substrate has tan(δ)=0 and neglecting losses in the metals). We observe high values for radiation gain, significantly larger than the load gain. These results are based upon the terminations of $Z_y = Z_s = Z_L = 50\ \Omega$ for the bottom and middle lines and short circuit for the top lines ($Z_x = 0\ \Omega$), similar to previous section. The results of Fig. 3.8(d) shows that, while being stable, for the case of $N = 8$, we reached the radiation gain of $G_{\text{Radiation}} = 8.75$ for the passive radiating elements with $+G$, while the load gain has a lower value of $G_L = 4.5$ at the EPD resonance frequency. By increasing the radiator's length, the radiation gain increases significantly, which makes the proposed structure a good scheme for distributed amplifier applications.

Sec. 3.4 Conclusion

We have reported the existence of third order EPDs in three-way waveguides modeled using three coupled microstrip transmission lines (3CTLs) with a *PT*-glide symmetric topology to achieve the coalescence of the modes at desired frequency. We have explored different features and properties of such novel design in which a third order EPD, i.e. a third order modal degeneracy, is manifested. We have provided different designs, where we demonstrated how the group velocity of the mode with purely real wavenumber can be slightly altered by tuning the physical parameters which may be beneficial for various applications. A potential scheme using the third order EPD could be in novel high gain

distributed amplifiers with novel characteristics and improved performances. We have briefly discussed such application and provided the radiation gain analysis for the finite-length terminated structure. The fundamental idea presented here is not limited to the specific design shown in this chapter but can be potentially applied to a variety of periodic waveguide structures implemented in different technologies.

This chapter is reproduced in part based on the material in manuscript [F. Yazdi, T. Mealy, A. Nikzamir, R. Marosi, and F. Capolino, "Third Order Modal Exceptional Degeneracy in Parity-Time Glide Symmetric Three-Way Microstrip Waveguide", in submission to a peer-reviewed journal]

Appendix A Parameters Used in Simulations

In our simulations, we considered a periodic coupled three-way waveguide composed of unit cells each made of three coupled TLs as in Fig. 3.2. For all the designs discussed in this chapter, the microstrip line widths are fixed to have w = 5 mm (i.e., with 50 Ω characteristic impedance) and s = 0.5 mm for the distancing between the lines. The substrate is assumed to have a relative dielectric constant of 2.2, loss tangent of 0 (lossless dielectric), and thickness of h_s = 1.575 mm. Metal layers are assumed to be lossless as well.

Case *A*: The tuned unit-cell parameters that led to an EPD were found to have conductance values of G = 0.1398 S (or equivalently $R = 1/G$ = 7.15 Ω), serpentine height of h = 5.35 mm, and period of d = 54.15 mm.

Case *B*: For this case, the tuned unit-cell parameters have a conductance values of G = 0.105 S (or equivalently $R = 1/G$ = 9.5 Ω), serpentine height of h = 6.36 mm, and period of d = 46.3 mm.

Case C: For this case, the tuned parameters have a conductance values of G = 0.0099 S (or equivalently R =1/G = 100.55 Ω), serpentine height of h = 1.07 mm, and period of d = 48.08 mm.

Appendix B Transfer Matrix Formalism

A. Transfer Matrices for CTLs

In order to construct the transfer matrix and tune the physical unit cell dimensions to acquire a third order EPD, we have divided the unit cell of the three-way microstrip structure into smaller sections as shown in Fig. 3.1 and modeled each section to obtain the unit-cell transfer matrix. We built the T-matrix of each section using TL analytic formulas based on quasistatic models in [37], [38].

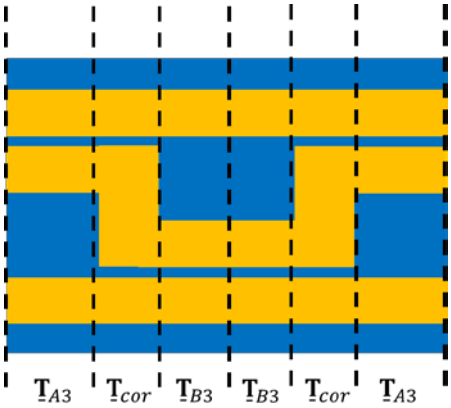

Fig. A1. Unit cell of the 3-way periodic microstrip structure used to obtain the EPD divided into smaller segments to construct the corresponding transfer function for each segment in terms of the physical parameters of the unit cell. The total transfer matrix of the unit cell is then derived by multiplying these smaller transfer matrices.

The transfer matrices of each smaller section of the unit cell shown in Fig. 1A, is expressed and calculated in terms of the parameters of the unit cell of the system (length, width, height, separation), and finally the transfer matrix for the whole unit cell (without

the added conductances) is obtained by the product of the transfer matrices for each smaller segment of 3CTL inside the unit cell as:

$$\underline{\mathbf{T}}_U = \underline{\mathbf{T}}_{A3}\underline{\mathbf{T}}_{cor}\underline{\mathbf{T}}_{B3}\underline{\mathbf{T}}_{B3}\underline{\mathbf{T}}_{cor}\underline{\mathbf{T}}_{A3}. \tag{A1}$$

B. Transfer Matrices for Lumped Conductances

We find the transfer matrices for the added conductance and gain lumped elements in each unit cell. For the first admittance added on the top line with the value of *+G* (passive device) we have

$$\underline{\mathbf{T}}_{+G} = \begin{pmatrix} 1 & 0 & 0 & \\ G & 1 & 0 & \underline{\mathbf{0}}_{3\times3} \\ 0 & 0 & 1 & \\ & \underline{\mathbf{0}}_{3\times3} & & \underline{\mathbf{I}}_{3\times3} \end{pmatrix}, \tag{A2}$$

where G is the conductance value (assumed positive) of the active gain device. For the second admittance added on the bottom line with the value of *-G* (active device) we have

$$\underline{\mathbf{T}}_{-G} = \begin{pmatrix} \underline{\mathbf{I}}_{3\times3} & & \underline{\mathbf{0}}_{3\times3} & \\ & 1 & 0 & 0 \\ \underline{\mathbf{0}}_{3\times3} & 0 & 1 & 0 \\ & 0 & -G & 1 \end{pmatrix}. \tag{A3}$$

Therefore, the total transfer matrix for the unit cell shown in Fig. 3.2(a) including the added lumped radiation conductance and gain device is calculated as:

$$\underline{\mathbf{T}}_U = \underline{\mathbf{T}}_{-G}\underline{\mathbf{T}}_{A3}\underline{\mathbf{T}}_{cor}\underline{\mathbf{T}}_{B3}\underline{\mathbf{T}}_{+G}\underline{\mathbf{T}}_{B3}\underline{\mathbf{T}}_{cor}\underline{\mathbf{T}}_{A3}. \tag{A4}$$

Whereas, the total transfer matrix for the unit cell shown in Fig. 3.2(b), including the added lumped radiation conductance and gain device, is calculated as

$$\underline{\mathbf{T}}_U = \underline{\mathbf{T}}_{G}\underline{\mathbf{T}}_{A3}\underline{\mathbf{T}}_{cor}\underline{\mathbf{T}}_{B3}\underline{\mathbf{T}}_{-G}\underline{\mathbf{T}}_{B3}\underline{\mathbf{T}}_{cor}\underline{\mathbf{T}}_{A3}. \tag{A5}$$

References

[1] A. Figotin and I. Vitebskiy, "Electromagnetic unidirectionality in magnetic photonic crystals," *Phys. Rev. B*, vol. 67, no. 16, p. 165210, Apr. 2003, doi: 10.1103/PhysRevB.67.165210.

[2] A. Figotin and I. Vitebskiy, "Gigantic transmission band-edge resonance in periodic stacks of anisotropic layers," *Phys. Rev. E*, vol. 72, no. 3, p. 036619, Sep. 2005, doi: 10.1103/PhysRevE.72.036619.

[3] A. Figotin and I. Vitebskiy, "Frozen light in photonic crystals with degenerate band edge," *Phys. Rev. E*, vol. 74, no. 6, p. 066613, Dec. 2006, doi: 10.1103/PhysRevE.74.066613.

[4] A. Figotin and I. Vitebskiy, "Slow-wave resonance in periodic stacks of anisotropic layers," *Phys. Rev. A*, vol. 76, no. 5, p. 053839, Nov. 2007, doi: 10.1103/PhysRevA.76.053839.

[5] A. Figotin and I. Vitebskiy, "Slow light in photonic crystals," *Waves Random Complex Media*, vol. 16, no. 3, pp. 293–382, 2006, doi: 10.1080/17455030600836507.

[6] A. Figotin and I. Vitebskiy, "Slow wave phenomena in photonic crystals," *Laser Photonics Rev.*, vol. 5, no. 2, pp. 201–213, Mar. 2011, doi: 10.1002/lpor.200900049.

[7] C. M. Bender and S. Boettcher, "Real spectra in non-Hermitian Hamiltonians having P T symmetry," *Phys. Rev. Lett.*, vol. 80, no. 24, p. 5243, Jun. 1998, doi: 10.1103/PhysRevLett.80.5243.

[8] W. D. Heiss, M. Müller, and I. Rotter, "Collectivity, phase transitions, and exceptional points in open quantum systems," *Phys. Rev. E*, vol. 58, no. 3, p. 2894, Sep. 1998, doi: 10.1103/PhysRevE.58.2894.

[9] T. Stehmann, W. D. Heiss, and F. G. Scholtz, "Observation of exceptional points in electronic circuits," *J. Phys. Math. Gen.*, vol. 37, no. 31, p. 7813, Jul. 2004, doi: 10.1088/0305-4470/37/31/012.

[10] R. El-Ganainy, K. G. Makris, D. N. Christodoulides, and Z. H. Musslimani, "Theory of coupled optical PT-symmetric structures," *Opt. Lett.*, vol. 32, no. 17, pp. 2632–2634, 2007, doi: 10.1364/OL.32.002632.

[11] C. E. Rüter, K. G. Makris, R. El-Ganainy, D. N. Christodoulides, M. Segev, and D. Kip, "Observation of parity–time symmetry in optics," *Nat. Phys.*, vol. 6, no. 3, pp. 192–195, Jan. 2010, doi:10.1038/nphys1515.

[12] J. Schindler, A. Li, M. C. Zheng, F. M. Ellis, and T. Kottos, "Experimental study of active LRC circuits with PT symmetries," *Phys. Rev. A*, vol. 84, no. 4, p. 040101, Oct. 2011, doi: 10.1103/PhysRevA.84.040101.

[13] S. Bittner *et al.*, "P T Symmetry and Spontaneous Symmetry Breaking in a Microwave Billiard," *Phys. Rev. Lett.*, vol. 108, no. 2, p. 024101, Jan. 2012, doi: 10.1103/PhysRevLett.108.024101.

[14] H. Ramezani, S. Kalish, I. Vitebskiy, and T. Kottos, "Unidirectional Lasing Emerging from Frozen Light in Nonreciprocal Cavities," *Phys. Rev. Lett.*, vol. 112, no. 4, p. 043904, Jan. 2014, doi: 10.1103/PhysRevLett.112.043904.

[15] H. Hodaei, M.-A. Miri, M. Heinrich, D. N. Christodoulides, and M. Khajavikhan, "Parity-time–symmetric microring lasers," *Science*, vol. 346, no. 6212, pp. 975–978, Nov. 2014, doi: 10.1126/science.1258480.

[16] L. Feng, Z. J. Wong, R.-M. Ma, Y. Wang, and X. Zhang, "Single-mode laser by parity-time symmetry breaking," *Science*, vol. 346, no. 6212, pp. 972–975, Nov. 2014, doi: 10.1126/science.1258479.

[17] Z. Liu, Q. Zhang, X. Liu, Y. Yao, and J.-J. Xiao, "Absence of Exceptional Points in Square Waveguide Arrays with Apparently Balanced Gain and Loss," *Sci. Rep.*, vol. 6, no. 1, Art. no. 1, Mar. 2016, doi: 10.1038/srep22711.

[18] J. Wiersig, "Sensors operating at exceptional points: General theory," *Phys. Rev. A*, vol. 93, no. 3, p. 033809, Mar. 2016, doi: 10.1103/PhysRevA.93.033809.

[19] M. Bagheriasl, O. Quevedo-Teruel, and G. Valerio, "Bloch Analysis of Artificial Lines and Surfaces Exhibiting Glide Symmetry," *IEEE Trans. Microw. Theory Tech.*, vol. 67, no. 7, pp. 2618–2628, Jul. 2019, doi: 10.1109/TMTT.2019.2916821.

[20] F. Ghasemifard, M. Norgren, O. Quevedo-Teruel, and G. Valerio, "Analyzing Glide-Symmetric Holey Metasurfaces Using a Generalized Floquet Theorem," *IEEE Access*, vol. 6, pp. 71743–71750, 2018, doi: 10.1109/ACCESS.2018.2882056.

[21] M. B. Stephanson, K. Sertel, and J. L. Volakis, "Frozen Modes in Coupled Microstrip Lines Printed on Ferromagnetic Substrates," *IEEE Microw. Wirel. Compon. Lett.*, vol. 18, no. 5, pp. 305–307, May 2008, doi: 10.1109/LMWC.2008.922107.

[22] M. A. K. Othman, F. Yazdi, A. Figotin, and F. Capolino, "Giant gain enhancement in photonic crystals with a degenerate band edge," *Phys. Rev. B*, vol. 93, no. 2, p. 024301, Jan. 2016, doi: PhysRevB.93.024301.

[23] H. Kazemi, M. Y. Nada, A. Nikzamir, F. Maddaleno, and F. Capolino, "Experimental Demonstration of Exceptional Points of Degeneracy in Linear Time Periodic Systems and Exceptional Sensitivity," *ArXiv190808516 Phys.*, Sep. 2020, Accessed: Mar. 09, 2021. [Online]. Available: http://arxiv.org/abs/1908.08516.

[24] G. Castaldi, S. Savoia, V. Galdi, A. Alù, and N. Engheta, "P T Metamaterials via Complex-Coordinate Transformation Optics," *Phys. Rev. Lett.*, vol. 110, no. 17, p. 173901, Apr. 2013, doi:10.1103/PhysRevLett.110.173901.

[25] F. Yazdi, M. A. K. Othman, M. Veysi, A. Figotin, and F. Capolino, "A New Amplification Regime for Traveling Wave Tubes With Third-Order Modal Degeneracy," *IEEE Trans. Plasma Sci.*, vol. 46, pp. 43–56, Jan. 2018, doi: 10.1109/TPS.2017.2781245.

[26] G. Mumcu, K. Sertel, and J. L. Volakis, "Lumped circuit models for degenerate band edge and magnetic photonic crystals," *Microw. Wirel. Compon. Lett. IEEE*, vol. 20, no. 1, pp. 4–6, Nov. 2010, doi: LMWC.2009.2035943.

[27] M. Y. Nada, T. Mealy, and F. Capolino, "Frozen Mode in Three-Way Periodic Microstrip Coupled Waveguide," *IEEE Microw. Wirel. Compon. Lett.*, vol. 31, no. 3, pp. 229–232, Dec. 2020, doi: 10.1109/LMWC.2020.3042205.

[28] M. Othman and F. Capolino, "Demonstration of a Degenerate Band Edge in Periodically-Loaded Circular Waveguides," *IEEE Microw. Wirel. Compon. Lett.*, vol. 25, no. 11, Oct. 2015, doi: LMWC.2015.2479845.

[29] M. Othman, V. A. Tamma, and F. Capolino, "Theory and New Amplification Regime in Periodic Multi Modal Slow Wave Structures with Degeneracy Interacting with an Electron Beam," *IEEE Trans Plasma Sci*, vol. 44, no. 4, Apr. 2016, doi: TPS.2016.2538786.

[30] M. A. Othman, M. Veysi, A. Figotin, and F. Capolino, "Giant Amplification in Degenerate Band Edge Slow-Wave Structures Interacting with an Electron Beam," *Phys. Plasmas 1994-Present*, vol. 23, no. 3, p. 033112, 2016.

[31] M. A. Othman, M. Veysi, A. Figotin, and F. Capolino, "Low Starting Electron Beam Current in Degenerate Band Edge Oscillators," *IEEE Trans. Plasma Sci.*, vol. 44, no. 6, pp. 918–929, May 2016, doi: 10.1109/TPS.2016.2558586.

[32] C. Löcker, K. Sertel, and J. L. Volakis, "Emulation of propagation in layered anisotropic media with equivalent coupled microstrip lines," *Microw. Wirel. Compon. Lett. IEEE*, vol. 16, no. 12, pp. 642–644, Dec. 2006, doi: LMWC.2006.885586.

[33] J. R. Burr, N. Gutman, C. Martijn de Sterke, I. Vitebskiy, and R. M. Reano, "Degenerate band edge resonances in coupled periodic silicon optical waveguides," *Opt. Express*, vol. 21, no. 7, pp. 8736–8745, Apr. 2013, doi: 10.1364/OE.21.008736.

[34] N. Gutman, A. A. Sukhorukov, F. Eilenberger, and C. M. de Sterke, "Bistability suppression and low threshold switching using frozen light at a degenerate band edge waveguide," *Opt. Express*, vol. 20, no. 24, pp. 27363–27368, 2012, doi:10.1364/OE.20.027363.

[35] A. F. Abdelshafy, M. A. K. Othman, D. Oshmarin, A. T. Almutawa, and F. Capolino, "Exceptional Points of Degeneracy in Periodic Coupled Waveguides and the Interplay of Gain and Radiation Loss: Theoretical and Experimental Demonstration," *IEEE Trans. Antennas Propag.*, vol. 67, no. 11, pp. 6909–6923, Nov. 2019, doi: 10.1109/TAP.2019.2922778.

[36] G. Gonzalez, *Microwave Transistor Amplifiers: Analysis and Design*. Englewood Cliffs, N.J.: Prentice-Hall, 1984.

[37] E. Hammerstad and O. Jensen, "Accurate Models for Microstrip Computer-Aided Design," in *1980 IEEE MTT-S International Microwave symposium Digest*, May 1980, pp. 407–409, doi: 10.1109/MWSYM.1980.1124303.

[38] M. Kirschning and R. H. Jansen, "Accurate Wide-Range Design Equations for the Frequency-Dependent Characteristics of Parallel Coupled Microstrip Lines (Corrections)," *IEEE Trans. Microw. Theory Tech.*, vol. 33, no. 3, pp. 288–288, Mar. 1985, doi: 10.1109/TMTT.1985.1133005.

CHAPTER 4

Wigner Time and LDOS Enhancement in Photonic Crystals with a Degenerate Band Edge

Sec. 4.1 Motivation

The main goal of this chapter is to report that slow-wave resonance associated with a degenerate band edge (DBE) in the dispersion diagram of photonic crystals can substantially increase the local density of states (LDOS) and Wigner time in a Fabry-Perot cavity (FPC). The enormous enhancement of the local density of states and therefore the density of states (DOS) at frequencies close to the DBE can be interpreted as a giant gain enhancement in the FPC. We provide analytic steps and calculations in order to find the transfer matrix and complex transmission coefficients of an *N*-period, one-dimensional structure made by stacking anisotropic tri-layers, to be able to exhibit DBE characteristics, in the simplest form possible. These findings then will be used to calculate Wigner time and LDOS of the cavity under investigation. The asymptotic analysis provides valuable insight into this new scheme operating at the degenerate band edge condition of photonic crystals.

Optical Fabry-Perot Cavities (FPCs) formed by photonic crystals (PhCs) have large quality factors, a property needed for a wide range of optical applications including lasers and sensors. Typically, PhC lasers work in the vicinity of near the regular photonic band edge (RBE) of the wavenumber-frequency dispersion diagram (for example see [1], and [2]). This is because Bloch waves have an intrinsic feedback mechanism near the band edge due to substantial mismatch of the Bloch wave and the surrounding media, leading to enhancing quality and Purcell factors. An important aspect in relation to lasers is that when an optical gain is introduced into a defect-free PhC, it can also operate as a laser without extrinsic mirrors.

A very promising way to further enhance the quality and Purcell factors of resonators for laser applications is by utilizing a special band edge condition associated to a degeneracy condition of the structural eigenmodes of a PhC: the degenerate band edge (DBE) condition introduced in [3]–[9]. In RBE PhCs [1], and [2], the operation is based on a single mode operating near the RBE point, whereas in the DBE PhCs operates with two modes that are both degenerate at the edge of the Brillouin zone of the dispersion diagram. We demonstrate in this thesis that a Fabry-Perot cavity (FPC) composed of repeating a cascade of unit cells capable of supporting a DBE, allows substantial enhancement in group delay (or Wigner time) and local density of states for laser applications. We also provide analytical results that provide insight into the design of photonic crystal lasers utilizing the DBE, relative to an FPC working near the RBE. The results in this chapter are general to any periodic structure working near the band edge.

The two different kind of FPCs studied in this chapter are shown in Fig. 4.1 as periodic structures made up of dielectric layers. The first FPC, shown in Fig. 4.1(a), is made by stacking isotropic dielectric bi-layers (FPC with RBE) and the second one shown in Fig. 4.1(b) is made by stacking anisotropic tri-layers (FPC with DBE). Each period of this FPC is made by one isotropic

layer and two anisotropic layers with equal thickness. It must be noticed that inside the anisotropic layers, the *x* and *y* polarizations are coupled. These two periodic structures have the same unit cell thickness *d,* and the FPC length is $L = Nd$. We assume that the FPC with RBE is constructed from alternating lossless dielectric layers with real refractive indices $n_1 = 3.2$ and $n_2 = 1.5$ with equal thickness designed to have a band edge at $\omega_g = \omega_d$ for the sake of comparison.

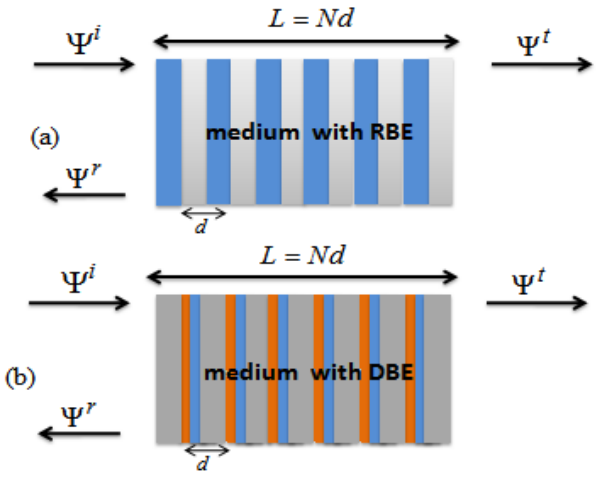

Fig. 4.1 Two topologies of an FPC (a) PhC exhibiting RBE with alternative layers having refractive indices n_1 = 3.2 and n_2 = 1.5. (b) PhC exhibiting DBE composed of three layers, one isotopic and two anisotropic layers with misalignment angle of 45^0.

The anisotropic layers of the unit cells of the PhC exhibiting DBE, shown in Fig. 4.1(b), have the parameters of $\varepsilon_{xx} = 16.31$, $\varepsilon_{yy} = 5.79$, and $\varepsilon_{zz} = 1$. The first anisotropic layer has an orientation α of its optical axes with respect to the reference system and has $\varepsilon_{xy} = 5.26$, while the second anisotropic layer has an orientation $-\alpha$, thus it has $\varepsilon_{xy} = -5.26$. This corresponds to a misalignment of $2\alpha = 45^o$ in the *x*-*y* plane, between the two adjacent anisotropic layers. The third layer is isotropic with $n = \varepsilon_{xx} = \varepsilon_{yy} = \varepsilon_{zz} = 1$.

In Fig. 4.2 the Brillouin zone dispersion diagram for the two topologies of FPCs made of periodic structures, shown in Fig. 4.1, is depicted where the real branches of the eigenmode Bloch wavenumber k are plotted in which for symmetry reasons, both k and $-k$ are modal solutions. As can be seen from the plot of Fig. 4.2, the solid blue line plot represents the dispersion diagram of the cavity with pairs of isotropic layers shown in Fig. 4.1(a) that supports only one propagating mode in the each direction below the RBE and the solid red line plot represents the cavity with anisotropic layers shown in Fig. 4.1(b) which is able to support two modes simultaneously propagating in the each direction below the RBE and only one propagating mode (the other is evanescent) below the DBE at $\omega = \omega_d$. Just below ω_d, there exists only one propagating mode for the RBE and DBE cases, as can be seen from Fig. 4.2.

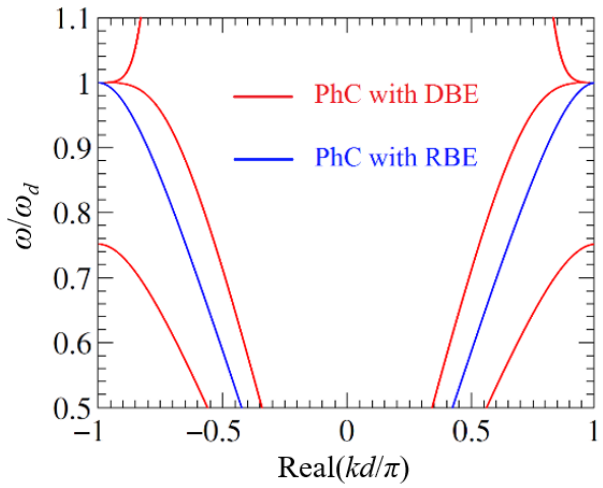

Fig. 4.2 Real parts of the k-ω dispersion relations where k is the Bloch complex wavenumber, for two photonic crystals (PhCs): one only exhibiting RBE and the other featuring also a DBE. This result is obtained by M. Othman and F. Yazdi.

The problem of finding an analytical expression for the density of states based on the complex transmission coefficients of a finite periodic structure (that exhibits RBE) is investigated in [10] in which they have developed a formula that expresses the density of states of an N-period, one

dimensional structure in terms of the transmission coefficients of one unit cell. In our investigation in this chapter we are considering the problem of finding the local density of states and Wigner time for a one dimensional *N*-period structure that exhibits DBE based on the complex transmission coefficient values derived from the transfer matrix of one unit cell of the periodic structure and its lower powers. Therefore, one of the main concerns that we will deal with it in this chapter is to find the transfer matrix of the a periodic structure consisting of *N* identical unit cells in terms of the transfer matrix of one unit cell and its powers up to three. We have shown that we can find a closed formula in this case. From the transfer matrix found in this way, we are able to find the transmission/reflection coefficients of the periodic medium that can be used later to calculate some of the important quantities of the cavity such as Wigner time. The density of states (DOS) is a convenient measure in finding some of the macroscopic quantities of the periodic structures, which is defined in different ways and in general is an average over time domains and the space occupied by the system. In [10] the most conventional ways to calculate DOS in literature is being reviewed. The first approach is using the concept of the local density of states (LDOS) [11]–[14] based on the Green's function of a source located inside the structure. Then the density of states would be the average of LDOS over the volume of the cavity [10]. We have gone over the calculation of the LDOS in length in ref. [15], where we show an remarkable enhancement of the LDOS in the cavity with DBE compared to the one with RBE of the same length due to unconventional resonance inside the FPC. The second important approach to find DOS is through the calculations of the phase of the transmission functions and the concept of Wigner time. This approach first emerged in [16]. Wigner time which is also called phase time, tunneling time, or group delay in the literature is derived from the principle phase of the transmission coefficient and is a measure of the effective group velocity of photons passing through the FPC [15]. The DOS

through Wigner time would be the average of this parameter over the volume and over the polarizations. In the current chapter we focus on the first and third approaches to find the density of states our presented structure with DBE characteristics in details. In [15] we have shown also advantage of the Wigner time in FPC that exhibits DBE and in this chapter we elaborate more on this concept and present an analytical method to calculate it rather than numerical approach done before.

In section 4.2 of this chapter we go over electromagnetic waves and Maxwell equations inside a periodic layered media that can support DBE. The state vector which is the solution of transverse fields along the propagation direction is defined is this section. The transfer matrix of a unit cell of the periodic structure under investigation is studied in section 4.3. By knowing the transfer matrix of each layer in one period we can construct the unit cell's transfer matrix and it has been shown in this section that by having this transfer matrix and choosing the right selection vectors we can find transmission coefficients for different polarizations. In section 4.4 we derive an expression for the total transfer matrix of a periodic structure consisting of N unit cells based on the transfer matrix of one unit cell found in section 4.3 and its second and third powers. The rest of the section is dedicated to finding the transmission coefficients of the periodic structure in terms of the parameters of one unit cell.

In section 4.5, we will exploit the information in the transmission and reflection coefficients found previously, to obtain two interesting parameters of the structure under study: Wigner time which is related to the phase of the respective transmission coefficient and local density of states. The Wigner time and local density of states are calculated and plotted in this section. We have also provided the formulas for calculation of DOS through the Wigner time and local density of states. These findings will potentially be a used to calculate and evaluate the DOS and gain enhancement

in our future research on this topic.

Sec. 4.2 Electromagnetic Waves in Stratified Media

In this section the electrodynamic properties of periodic layered media composed of anisotropic layers that can support a DBE is briefly described. We consider time-harmonic Maxwell equations in heterogeneous media [4], [6]:

$$\nabla \times \vec{\mathbf{E}} = i\omega\mu_0 \vec{\mathbf{H}}, \nabla \times \vec{\mathbf{H}} = -i\omega\varepsilon_0 \vec{\vec{\boldsymbol{\varepsilon}}} \vec{\mathbf{E}}, \tag{4.1}$$

where the time harmonic convention $\exp(i\omega t)$ is assumed and suppressed in the rest of the chapter. The relative electric permittivity tensor describing each layer has the general properties of birefringent media and represented in the Cartesian coordinates as a 3x3 matrix in the following form [4], [5]

$$\vec{\vec{\boldsymbol{\varepsilon}}} = \begin{bmatrix} \varepsilon_{xx} & \varepsilon_{xy} & 0 \\ \varepsilon_{xy} & \varepsilon_{yy} & 0 \\ 0 & 0 & \varepsilon_{zz} \end{bmatrix}. \tag{4.2}$$

The structure is one-dimensional composed of layers each of which has a constant relative permittivity tensor with respect the z coordinate. We focus our analysis on structures with a piecewise homogenous permittivity profile along the z-direction, i.e., the structures are composed of cascaded homogenous layers, each of which is described by their individual permittivity tensors. Moreover, fields within the structure are only dependent on the single Cartesian coordinate z, i.e., the wavevector is directed along z. Assuming the above conditions, the normal field components E_z and $H_z$of electromagnetic wave vanish, and the system of six time-harmonic, coupled scalar Maxwell equations reduces to the following system of four ordinary linear differential equations for the transverse field components only [7]:

$$\frac{\partial}{\partial z}\boldsymbol{\Psi}(z) = ik_0\underline{\mathbf{M}}(z)\boldsymbol{\Psi}(z), \tag{4.3}$$

where $\boldsymbol{\Psi}(z) = [E_x(z) \quad E_y(z) \quad H_x(z) \quad H_y(z)]^T$ is the *state vector* that describes the evolution of the transverse fields in the z-direction, and $k_0 = \omega/c$, where c is the speed of light. This yields the following explicit expression for the Maxwell operator $\underline{\mathbf{M}}(z)$ in equation (4.3), within each homogenous region [17]:

$$\underline{\mathbf{M}}(z) = \begin{bmatrix} 0 & 0 & 0 & \eta_0 \\ 0 & 0 & -\eta_0 & 0 \\ -\varepsilon_{xy}/\eta_0 & -\varepsilon_{yy}/\eta_0 & 0 & 0 \\ \varepsilon_{xx}/\eta_0 & \varepsilon_{xy}/\eta_0 & 0 & 0 \end{bmatrix}, \tag{4.4}$$

where $\eta_0 = \sqrt{\mu_0/\varepsilon_0}$, is the free space impedance.

The solution of equation (4.3) can be developed assuming a known boundary condition $\boldsymbol{\Psi}(z_0)$ at z_0, and this solution allows us to obtain the state vector at an arbitrary point z_1. The relation between $\boldsymbol{\Psi}(z_0)$ and $\boldsymbol{\Psi}(z_0)$ is obtained by solving the differential equation (4.3):

$$\boldsymbol{\Psi}(z_1) = \underline{\mathbf{T}}(z_1, z_0)\,\boldsymbol{\Psi}(z_0), \tag{4.5}$$

where $\underline{\mathbf{T}}(z_1, z_0)$ is the transfer matrix given by $\underline{\mathbf{T}}(z_1, z_0) = \exp\big(i\underline{\mathbf{M}}(z_1 - z_0)\big)$, with $\underline{\mathbf{T}}(z_1, z_0) = \underline{\mathbf{T}}^{-1}(z_0, z_1)$ [6]. Since our structures is composed of many layers, we define the transfer matrix of a certain layer m with thickness d_m by $\underline{\mathbf{T}}_m = \exp\big(i\underline{\mathbf{M}}_m d_m\big)$ [4]. To solve the scattering problem, i.e., evaluating fields due to an impinging electromagnetic plane wave on the stack of layers in Fig. 4.1, we define the forward-backward state vector $\widehat{\boldsymbol{\Psi}}(z) = (E_x^+ \quad E_y^+ \quad E_x^- \quad E_y^-)^T$, which is composed of the electric fields incident and reflected amplitudes along the z-direction, associated to the x and y polarizations. This is an alternate description of the state vector defined in (4.3), more suitable to

describe the scattering properties of the structure. By analogy, one can also write an equivalent representation of (4.5) using the forward-backward state vector as:

$$\widehat{\mathbf{\Psi}}(z_1) = \underline{\widehat{\mathbf{T}}}(z_1, z_0)\, \widehat{\mathbf{\Psi}}(z_0). \tag{4.6}$$

Both $\widehat{\mathbf{\Psi}}(z)$ and $\mathbf{\Psi}(z)$ are intimately related to each other thorough a unitary similarity transformation $\underline{\mathbf{U}}$ (see Appendix A). Even though each layer is bounded by other layers, it is customary to define and refer reflection and transmission using a nominal reference impedance that is here chosen to be equal to η_0. As shown in Appendix A, assuming same termination in terms of characteristic impedance η_0 for the left and right side of the structure being studied, the following matrix equation can be used to transform $\underline{\mathbf{T}}$ to $\underline{\widehat{\mathbf{T}}}$

$$\underline{\widehat{\mathbf{T}}} = \underline{\mathbf{U}}^{-1}\underline{\mathbf{T}}\underline{\mathbf{U}}, \tag{4.7}$$

in which the matrix $\underline{\mathbf{U}}$ is defined as

$$\underline{\mathbf{U}} = \begin{pmatrix} 1 & 0 & 1 & 0 \\ 0 & 1 & 0 & 1 \\ 1/\eta_0 & 0 & -1/\eta_0 & 0 \\ 0 & -1/\eta_0 & 0 & 1/\eta_0 \end{pmatrix}. \tag{4.8}$$

Note that the choice of the reference impedance is arbitrary, since layers are not terminated on that impedance, and it is used only to define $\widehat{\mathbf{\Psi}}(z)$ when $\mathbf{\Psi}(z)$ is known.

Sec. 4.3 Transfer Matrix for One Unit Cell

A unit cell with length d is shown in Fig. 4.3, which includes three layers: two birefringent layers A and B with different orientations φ_1 and φ_2 of the respective anisotropy axes in the x-y plane, and one isotropic C layer. Behavior of each layer in the unit cell can be represented by the corresponding transfer matrix $\underline{\mathbf{T}}_m$ of that layers. Knowing the termination impedance of the

layers, one may obtain $\underline{\hat{\mathbf{T}}}_m$ of that layer. Therefore, the total transfer matrix of a unit cell can be derived by multiplication of these individual $\underline{\hat{\mathbf{T}}}_i$s as stated below

$$\underline{\hat{\mathbf{T}}} = \underline{\hat{\mathbf{T}}}_A \underline{\hat{\mathbf{T}}}_B \underline{\hat{\mathbf{T}}}_C. \tag{4.9}$$

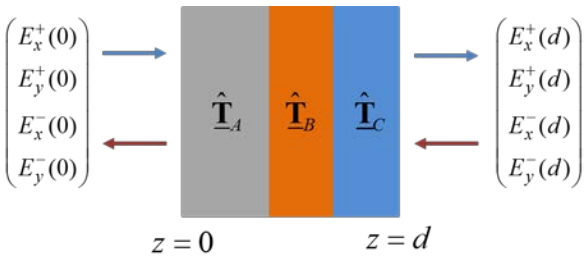

Fig. 4.3 A unit cell with length of d consisting three layers that can support DBE and relative electric permittivity tensor of $\vec{\vec{\boldsymbol{\varepsilon}}}(z)$.

Thus, if the transfer matrix of each layer is known, one way to find the unit cell's transfer matrix is the multiplication in equation (4.9). Using this approach to find $\underline{\hat{\mathbf{T}}}$ of one unit cell and then derivation of the transfer matrix of the periodic cavity may complicate the calculations and be pointless. Since we are interested in more general parameters like transmission coefficients of cavity, a simpler method is presented here to find the unit cell's transfer function in which the three layers are assumed be an integrated unit cell with $\underline{\hat{\mathbf{T}}}$ and then this matrix can be found using the solution of Helmholtz equation and boundary conditions.

In the interval $[0, d]$, the general solution to the Helmholtz equation can be written as the superposition of forward and backward waves labeled as plus and minus respectively. Written in column vector form we will have $\hat{\mathbf{\Psi}}$ introduced above as our state vector. In order to be able to find the desired characteristics of structure under study we need to start with finding the transfer matrix $\underline{\hat{\mathbf{T}}}$ for one unit cell defined as

$$\begin{pmatrix} E_x^+(0) \\ E_y^+(0) \\ E_x^-(0) \\ E_y^-(0) \end{pmatrix} = \underline{\hat{\mathbf{T}}} \begin{pmatrix} E_x^+(d) \\ E_y^+(d) \\ E_x^-(d) \\ E_y^-(d) \end{pmatrix} \tag{4.10}$$

If we only have the *x*-polarized wave incident from the left to the unit cell we have the following boundary condition

$$\begin{pmatrix} 1 \\ 0 \\ r_{xx} \\ r_{yx} \end{pmatrix} = \underline{\hat{\mathbf{T}}} \begin{pmatrix} t_{xx} \\ t_{yx} \\ 0 \\ 0 \end{pmatrix}, \tag{4.11}$$

where t_{pq} and r_{pq} are the transmission and reflection coefficients of waves polarized along p due to an incident wave polarized along q. Similarly, if we have only the incident *y*-polarized wave we have

$$\begin{pmatrix} 0 \\ 1 \\ r_{xy} \\ r_{yy} \end{pmatrix} = \underline{\hat{\mathbf{T}}} \begin{pmatrix} t_{xy} \\ t_{yy} \\ 0 \\ 0 \end{pmatrix}. \tag{4.12}$$

By applying the incident waves from right to left and having in mind that the scattering process is invariant under time reversal, we have two other boundary conditions. By implying all these boundary conditions, we can see that the transfer matrix $\underline{\hat{\mathbf{T}}}$ has the general block form of

$$\underline{\hat{\mathbf{T}}} = \begin{pmatrix} \underline{\hat{\mathbf{T}}}_{11} & \underline{\hat{\mathbf{T}}}_{12} \\ \underline{\hat{\mathbf{T}}}_{21} & \underline{\hat{\mathbf{T}}}_{22} \end{pmatrix}, \tag{4.13}$$

where for example t_{xx} is the transmission coefficient for an *x*-polarized incident wave in the absence of any incident *y*-polarized plane wave and calculated as

$$t_{xx} = \vec{\boldsymbol{u}}_x^T \frac{\underline{\hat{\boldsymbol{T}}}_{11}}{det[\underline{\hat{\boldsymbol{T}}}_{11}]} \cdot \vec{\boldsymbol{v}}_x, \tag{4.14}$$

where $\vec{\boldsymbol{u}}$ and $\vec{\boldsymbol{v}}$ denote unit polarization selection vectors such as $\vec{\boldsymbol{u}}_x = [0 \quad 1]^T$ and $\vec{\boldsymbol{v}}_x = [0 \quad 1]^T$. Similar reasoning applies to a *y*-polarized incident wave and its reflection and transmission coefficients.

Sec. 4.4 Periodic Structure with *N* Cascaded Unit Cells

For a periodic structure consisting of *N* identical unit cells as shown in Fig. 4.4, the total transfer matrix is calculated by multiplying the transfer matrix of each unit cell N times which is the N^{th} power of $\hat{\underline{\mathbf{T}}}$. In another word we have a transfer matrix $\hat{\underline{\mathbf{T}}}^N$, which satisfies the following equation:

$$\begin{pmatrix} E_x^+(0) \\ E_y^+(0) \\ E_x^-(0) \\ E_y^-(0) \end{pmatrix} = \hat{\underline{\mathbf{T}}}^N \begin{pmatrix} E_x^+(Nd) \\ E_y^+(Nd) \\ E_x^-(Nd) \\ E_y^-(Nd) \end{pmatrix}. \tag{4.15}$$

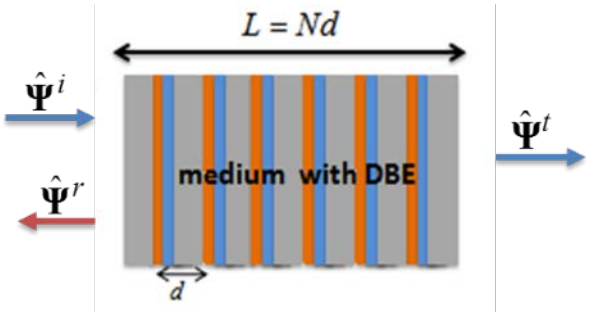

Fig. 4.4 Periodic structure consisting of *N* unit cells featuring DBE.

In this section we will try to find the total periodic structure transfer matrix $\hat{\underline{\mathbf{T}}}^N$ in terms of lower powers of $\hat{\underline{\mathbf{T}}}$ to facilitate the calculations of Wigner time and density of states. Suppose, for the sake of discussion, we were to impose the periodic boundary condition $\vec{\vec{\boldsymbol{\varepsilon}}}(z) = \vec{\vec{\boldsymbol{\varepsilon}}}(z+d)$ for $z \in (-\infty, \infty)$, where $\vec{\vec{\boldsymbol{\varepsilon}}}(z)$ is the relative electric permittivity tensor which is a periodic function of z. Then for the corresponding Bloch eigen-functions $\hat{\boldsymbol{\Psi}}$, appropriate for an infinite-period structure with unit cell $\vec{\vec{\boldsymbol{\varepsilon}}}(z), z \in (0, d]$, we have from the definition of eigenvector:

$$\hat{\underline{\mathbf{T}}}\hat{\mathbf{\Psi}} = \lambda_i \hat{\mathbf{\Psi}}, \tag{4.16}$$

with $\lambda_i = e^{ik_i d}$. We know that the Bloch functions change only in phase -and not in amplitude- from cell to cell in the infinite periodic potential. This phase per unit cell is called the Bloch phase, associated with the infinite periodic structure [18]. In the above equation λ_i is the eigenvalue of the transfer matrix $\hat{\underline{\mathbf{T}}}$ and $k_i d$ is the phase per unit cell or the Bloch phase, associated with the infinite periodic structure. In our structure we know that we have four eigenvalues which have the following $k_i = \pm k_1, \pm k_2$. The Cayley-Hamilton theorem that every matrix obeys its own characteristic equation [19]. Following Appendix B, we shall find $\hat{\underline{\mathbf{T}}}^N$ in terms of the lower powers of $\hat{\underline{\mathbf{T}}}$ as

$$\hat{\underline{\mathbf{T}}}^N = a_3\hat{\underline{\mathbf{T}}}^3 + a_2\hat{\underline{\mathbf{T}}}^2 + a_1\hat{\underline{\mathbf{T}}} + a_0\underline{\mathbf{I}}\,, \tag{4.17}$$

in whicha_0, a_1, a_2,a_3 are the unknown coefficients to be found. As stated in Appendix B in details, these coefficients are found by imposing that the eigenvalues must also satisfy (4.17)

$$\lambda_m^N = a_3\lambda_m^3 + a_2\lambda_m^2 + a_1\lambda_m + a_0, m = 1, 2, 3, 4. \tag{4.18}$$

A linear matrix equation can be formed by inserting each eigenvalue into the equation (18), and then the unknown coefficientsa_i are found by solving the following equation.

$$\begin{pmatrix} \lambda_1^3 & \lambda_1^2 & \lambda_1 & 1 \\ \lambda_2^3 & \lambda_2^2 & \lambda_2 & 1 \\ \lambda_3^3 & \lambda_3^2 & \lambda_3 & 1 \\ \lambda_4^3 & \lambda_4^2 & \lambda_4 & 1 \end{pmatrix} \begin{pmatrix} a_3 \\ a_2 \\ a_1 \\ a_0 \end{pmatrix} = \begin{pmatrix} \lambda_1^N \\ \lambda_2^N \\ \lambda_3^N \\ \lambda_4^N \end{pmatrix}, \tag{4.19}$$

in which $\lambda_i = e^{ik_i d}$ are the eigenvalues. Details of the above formulation along with the analytical expressions of the coefficients is provided in appendix B.

It is now important to investigate what happens when the frequency is close to DBE one, i.e., when $|\omega - \omega_d|/\omega_d << 1$ for any structure that exhibits a DBE, such as the one in Fig. 4.4 without loss of generality. This simplification will help to have a better understanding of the behavior of the FPC near DBE and provide a physical insight into that enhancement of quality factor as well as other factors that will be quantified later. For both the propagating and evanescent modes in the layered medium the following approximation well describes the Bloch wavenumbers near DBE $(\omega - \omega_d) \approx \alpha(k - k_d)^4$ and α is a problem dependent constant. By defining a small phase perturbation δ and relaying on the symmetry of the dispersion diagram for k around the edge of the BZ k_d, the four branches neat the DBE are well approximated as:

$$k_{1,3} \approx k_d \pm \delta, \ and \ k_{2,4} \approx k_d \mp i\delta, \tag{4.20}$$

where $\delta = |\alpha|^{1/4}(\omega - \omega_d)^{1/4}$ and α is a constant. The four roots have been explicated in (4.20) therefore the choice of the root for δ is such that we have two propagating modes and two evanescent modes and δ is a positive real value.

We use the above formulas to calculate the coefficients needed to derive $\underline{\widehat{\mathbf{T}}}^N$ in equation (4.17). After taking the two lowest order terms in the Taylor series expansion for the coefficients a_i we find that

$$a_i \approx f_i + g_i(\delta d)^4, \tag{4.21}$$

where the coefficients f_i and g_i for $i = \{1,2,3,4\}$ are provided in Appendix B.

Till here we have shown that the transfer matrix of an FPC made of N unit cells can be calculated using lower powers of the transfer matrix of a unit cell, as well as providing a first order approximation thereof. Our objective in the rest of this section is to find the transmission coefficients of the periodic structure in terms of the transmission coefficients of one unit cell,

presented in section 4.3. For the total transfer matrix of the *N*-periodic cavity, similar to the case of an arbitrary unit cell with known refractive index, we can write

$$\hat{\underline{\mathbf{T}}}^N = \begin{pmatrix} \underline{\mathbf{T}}_{11} & \underline{\mathbf{T}}_{12} \\ \underline{\mathbf{T}}_{21} & \underline{\mathbf{T}}_{22} \end{pmatrix}^N = \begin{pmatrix} \underline{\mathbf{T}}_{11N} & \underline{\mathbf{T}}_{12N} \\ \underline{\mathbf{T}}_{21N} & \underline{\mathbf{T}}_{22N} \end{pmatrix}. \tag{4.22}$$

In general, the transmission coefficient for a certain polarization can be evaluated as follows: assume we have a plane wave polarized along a unit vector $\vec{\boldsymbol{p}}$, strictly directed in the *x*-*y* plane since we limit our analysis to transverse plane waves, such that $\vec{\boldsymbol{p}} = [p_x \quad p_y]^T$. It follows that the matrix operation $\vec{\boldsymbol{p}} \cdot \hat{\underline{\mathbf{T}}}^N \cdot \vec{\boldsymbol{p}}$ results in the element of an arbitrary power *N* of transfer matrix $\hat{\underline{\mathbf{T}}}$ in the first row and first column. Therefore, we define a polarization dependent transmission coefficient as

$$t_{\boldsymbol{pp}} = \vec{\boldsymbol{u}}_{\boldsymbol{p}}^T \left(\frac{\underline{\mathbf{T}}_{11N}}{\det[\underline{\boldsymbol{T}}_{11N}]} \right) \vec{\boldsymbol{v}}_{\boldsymbol{p}}, \tag{4.23}$$

with

$$\begin{aligned} \underline{\underline{\mathbf{T}}}_{11N} = a_0 \underline{\underline{\mathbf{I}}} + a_1 \underline{\underline{\mathbf{T}}}_{11} + a_2 \left(\underline{\underline{\mathbf{T}}}_{11}^2 + \underline{\underline{\mathbf{T}}}_{12} \underline{\underline{\mathbf{T}}}_{21} \right) + \\ + a_3 \left(\underline{\underline{\mathbf{T}}}_{11}^3 + \underline{\underline{\mathbf{T}}}_{11} \underline{\underline{\mathbf{T}}}_{12} \underline{\underline{\mathbf{T}}}_{21} + \underline{\underline{\mathbf{T}}}_{12} \underline{\underline{\mathbf{T}}}_{21} \underline{\underline{\mathbf{T}}}_{11}^2 + \underline{\underline{\mathbf{T}}}_{12} \underline{\underline{\mathbf{T}}}_{22} \underline{\underline{\mathbf{T}}}_{21} \right) \end{aligned} \tag{4.24}$$

This transmission coefficient (transfer function) provides significant information about the characteristics of the cavity as well as assessing the performance when a gain is introduced. A particular interesting feature of such coefficients in the form derived in (4.23) is that it is written as a rational function in frequency, which allows us to easily compute the transfer function properties such as poles and zeros, and therefore the time domain response of the system.

The transmission coefficients $t_{\boldsymbol{pp}}$ and also reflection coefficients $r_{\boldsymbol{pp}}$ for the periodic FPC consisting *N* = 32 unit cells, shown in Fig. 4.4, are calculated, and plotted in Fig. 4.5. This coefficient

is polarization dependent as it is obvious from the plot and this is due to the anisotropy of some layers in the FPC with DBE.

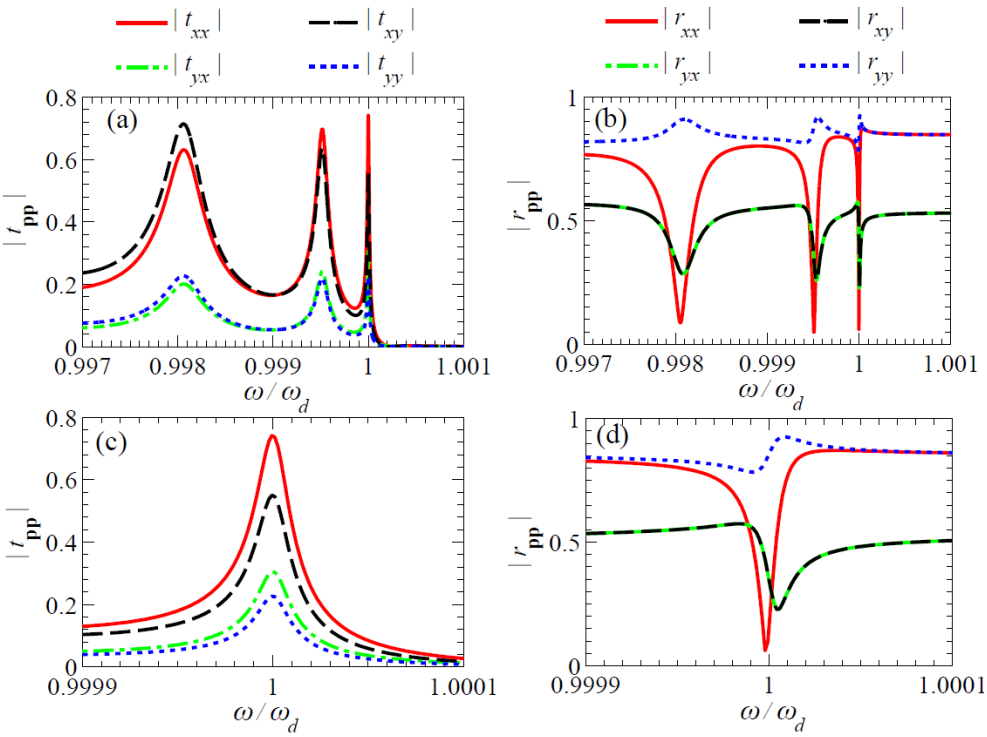

Fig. 4.5 Magnitude of the transmission (a) and reflection (b) coefficients versus radian frequency for FPC formed by a periodic structures that exhibit a DBE at ω_d for four different polarizations (N = 32). (c-d) Zoomed region near the DBE radian frequency ω_d. This result is obtained by M. Othman and F. Yazdi.

Sec. 4.5 Wigner Time and Local Density of States

A. Wigner Time

As mentioned earlier, several interesting parameters can be derived from the transmission coefficient. Wigner time which was first introduced in [16], represents the time that the transmitted part of an incident, quasi-monochromatic pulse takes to traverse a one dimensional

structure [16]. Here we first consider the concept of Wigner time (group delay) τ_{pp} which is related to the phase of transmission coefficient $t_{\mathbf{pp}}$ as

$$\tau_{pp} = \frac{d}{d\omega}\arg[t_{pp}], \tag{4.25}$$

where $\arg[t_{pp}]$ is the principle phase of the transmission coefficient, i.e., the total phase accumulated in the transmitted signal. After writing the complex valued transmission coefficient as $t_{pp} = t'_{pp} + it''_{pp}$ then the Wigner time is calculated by

$$\tau_{pp}(\omega) = \frac{(\partial_\omega t''_p)t'_p - (\partial_\omega t'_p)t''_p}{t'^2_p + t''^2_p}. \tag{4.26}$$

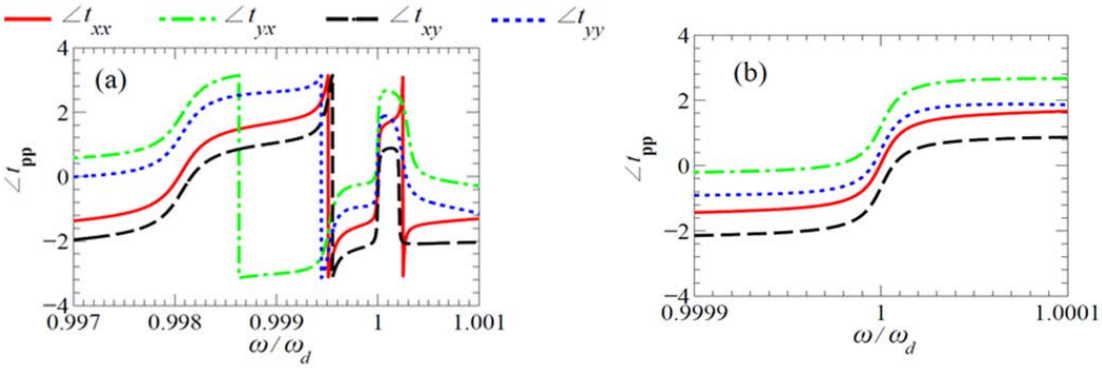

Fig. 4.6 (a) Phase of the transmission coefficients for N = 32 (b) Zoomed in version of the phase transition near the DBE for different polarizations. This result is obtained by M. Othman.

Fig. 4.6(a) and (b) show the phase variation of the transmission coefficients for four different polarizations very close to the DBE frequency. The normalized Wigner time for the FPC under study with a DBE, near ω_d is also shown in Fig. 4.7. This quantity is a measure of the effective group velocity of photons passing through the FPC.

The density of states (DOS) which is a useful quantity in finding some macroscopic quantities of the periodic structures can then be defined and calculated through the Wigner time as follows [10]

$$\rho_{\boldsymbol{pp}}(\omega) = \frac{\tau_{\boldsymbol{pp}}(\omega)}{L} \tag{4.27}$$

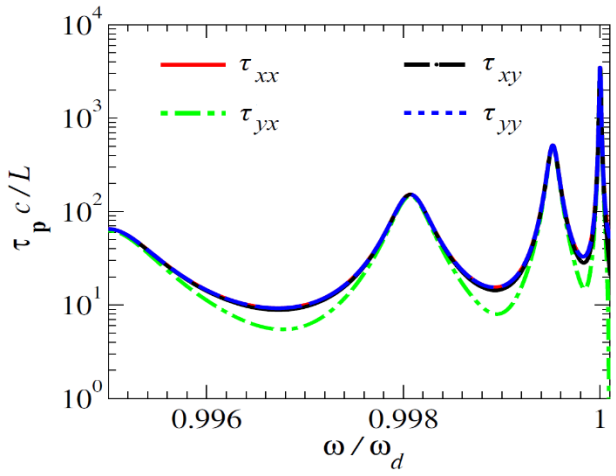

Fig. 4.7 Wigner time for FPC formed by a periodic structure with N = 32, that exhibit a DBE at ω_d for four different polarizations. This result is obtained by M. Othman and F. Yazdi.

B. Local Density of States (LDOS)

The LDOS is usually derived from the imaginary part of the trace of the structure's Green's dyadic. As shown in [14], [20] by using the definition of local density of electromagnetic energy at a given point in space and a given frequency, and by applying the fluctuation-dissipation theorem, the LDOS can be derived in terms of the system's Green's function [21] as follow [15] :

$$\rho(z,\omega) = -\frac{k_0}{\pi c}\,\mathrm{Im}\big(\mathrm{Tr}\big[\underline{\mathbf{G}}(z,z)\big]\big), \tag{4.28}$$

in which Im and Tr are imaginary part and matrix trace, respectively. It is noticeable that the above formula gives the correct value for LDOS of the case where we have a free space instead of the cavity. Another interesting fact is that the LDOS can be defined as the following multiplication [10]:

$$\rho(z,\omega) = \rho_{\mathrm{fs}}(\omega)\,\frac{\langle P_{\boldsymbol{p}}(z,\omega)\rangle_{\boldsymbol{p}}}{P_{\mathrm{fs}}}, \tag{4.29}$$

in which $\rho_{\text{fs}}(\omega)$ is the density of states in free space and has the value of $1/(\pi c)$ for one-dimensional periodic structures. $P_{\boldsymbol{p}}(z,\omega)$ is the time-average electromagnetic power at point z, emitted by the electric source polarized along an arbitrary polarization unit vector $\vec{\boldsymbol{p}}$ at the same point z inside the FPC, and P_{fs} denotes power emitted by the same source positioned in free space. The brackets $\langle\cdot\rangle_{\boldsymbol{p}}$ denote the average over all polarizations. It has be shown in [15] that

$$\frac{\rho(z,\omega)}{\rho_{\text{fs}}} = \frac{\langle P_{\boldsymbol{p}}(z,\omega)\rangle_L}{P_{\text{fs}}} = -k_0\,\text{Im}\big(\text{Tr}\big[\underline{\mathbf{G}}(z,z)\big]\big) \tag{4.30}$$

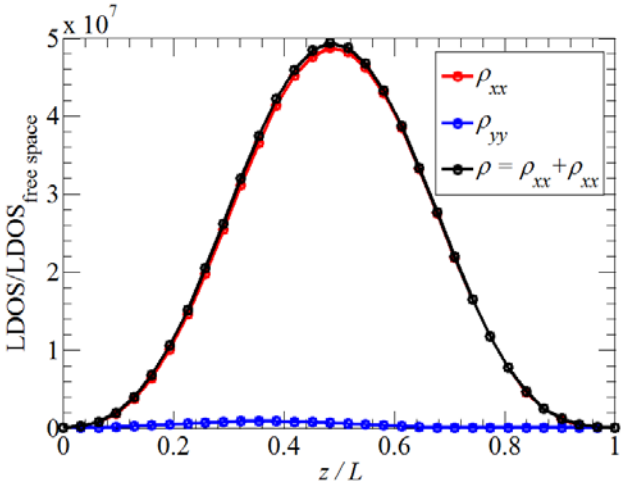

Fig. 4.8 Sampled local density of states (LDOS) normalized by the LDOS in free space inside FPC with DBE sampled at points $z = md, m = 0,1,2,\ldots,N$ with N = 32 for two polarizations. This result is obtained by M. Othman.

The LDOS normalized by the LDOS in free space for the FPC supporting DBE studied in this chapter is shown in Fig. 4.8, which is sampled in each unit cell in the periodic structure for simplicity. But it must be stated that it varies also within each unit cell. From the plot it be observed that the LDOS for the FPC with DBE has the maximum value around the cavity center unlike the uniform FPC that has a uniform LDOS envelope across the length. The density of states can also be defined as the average of LDOS over the volume of the cavity.

The calculation and evaluation of the DOS based on the two different methods introduced in this section will be considered as a possible future research on this topic.

Sec. 4.6 Conclusion

In conclusion for this chapter, we have shown the advantage of the proposed FPC consisting of periodic unit cells made up of anisotropic layers in terms of two of the most significant parameters of the cavity: local density of states and Wigner time. The extremely large Wigner time and the high local density of states for DBE structures will result in giant amplification in the gain medium which is of orders of magnitude larger than the same obtained for FPCs with RBE. Here we are more concentrated on finding and evaluating these two parameters (interpreted as a measure of gain) using asymptotic analytical results rather than numerical simulations. Also, one of the significant parts of this work is dedicated to finding the exact analytic formulation of the transfer matrix and transmission coefficients of the FPC under investigation. We have derived and presented the simplest possible form of expressing for these parameters of the cavity which will be used as a generalized method in any FPC with coupled waves.

Appendix A Transformation of $\underline{\hat{\mathbf{T}}}$ Matrix into $\underline{\mathbf{T}}$ Matrix Formalism

In section 4.2 the transfer matrix $\underline{\hat{\mathbf{T}}}$ formalism was shown which is based on the vector $\hat{\boldsymbol{\Psi}}$ that includes forward and backward electric waves for two polarizations. It is also necessary to show how to transform this formalism to the $\underline{\mathbf{T}}$ matrix formulation which is based on the vector $\boldsymbol{\Psi}$ instead. Let the wave vector $\boldsymbol{\Psi}$ be expressed in terms of the wave vector $\hat{\boldsymbol{\Psi}}$ by a non-singular linear transformation $\underline{\mathbf{U}}$

$$\boldsymbol{\Psi} = \underline{\mathbf{U}}\hat{\boldsymbol{\Psi}} \tag{A1}$$

This transformation can be applied to one unit cell as well as the periodic structure where we have more than one unit cell. Here we consider the case where we have same termination in terms of characteristic impedance for the left and right side of the structure being studied and assume the length L for the configuration. By substituting $\boldsymbol{\Psi} = \underline{\mathbf{U}}\widehat{\boldsymbol{\Psi}}$ into $\underline{\mathbf{T}}\boldsymbol{\Psi}(L) = \boldsymbol{\Psi}(0)$ we will get

$$\underline{\mathbf{T}}\underline{\mathbf{U}}\boldsymbol{\Psi}(L) = \underline{\mathbf{U}}\widehat{\boldsymbol{\Psi}}(0) \tag{A2}$$

Therefore, from the $\underline{\widehat{\mathbf{T}}}\widehat{\boldsymbol{\Psi}}(L) = \widehat{\boldsymbol{\Psi}}(0)$ we will have the following transformation.

$$\underline{\widehat{\mathbf{T}}} = \underline{\mathbf{U}}^{-1}\underline{\mathbf{T}}\underline{\mathbf{U}} \tag{A3}$$

The elements of wave vectors $\boldsymbol{\Psi}$ and $\widehat{\boldsymbol{\Psi}}$ are linearly related to each other. These linear relations will result in the following transformation.

$$\boldsymbol{\Psi} = \underline{\mathbf{U}}\widehat{\boldsymbol{\Psi}} = \begin{pmatrix} 1 & 0 & 1 & 0 \\ 0 & 1 & 0 & 1 \\ \frac{1}{\eta} & 0 & \frac{-1}{\eta} & 0 \\ 0 & \frac{-1}{\eta} & 0 & \frac{1}{\eta} \end{pmatrix} \widehat{\boldsymbol{\Psi}} \tag{A4}$$

Yet again, here we assumed $Z(0) = Z(L) = \eta$. Therefore, from equation (A4) $\underline{\mathbf{U}}$ is found and will result in the following transformation between $\underline{\widehat{\mathbf{T}}}$ and $\underline{\mathbf{T}}$ formalisms.

$$\underline{\widehat{\mathbf{T}}} = \frac{1}{2}\begin{pmatrix} 1 & 0 & \eta & 0 \\ 0 & 1 & 0 & -\eta \\ 1 & 0 & -\eta & 0 \\ 0 & 1 & 0 & \eta \end{pmatrix} \underline{\mathbf{T}} \begin{pmatrix} 1 & 0 & 1 & 0 \\ 0 & 1 & 0 & 1 \\ \frac{1}{\eta} & 0 & \frac{-1}{\eta} & 0 \\ 0 & \frac{-1}{\eta} & 0 & \frac{1}{\eta} \end{pmatrix} \tag{A5}$$

Appendix B Proof of Formula for $\underline{\widehat{\mathbf{T}}}^N$ in Terms of $\underline{\widehat{\mathbf{T}}}$

Here, using the Cayley-Hamilton theorem, we prove the equation (4.17) and calculate the required coefficients. In linear algebra, the Cayley–Hamilton theorem states that every square

matrix over a commutative ring (such as the real or complex field) satisfies its own characteristic equation. In our case we want to calculate its higher powers in terms of the lowest possible powers. By substituting the matrix $\underline{\hat{\mathbf{T}}}$ into its 4×4 characteristic polynomial we will have

$$\underline{\hat{\mathbf{T}}}^4 - \mathrm{tr}\left[\underline{\hat{\mathbf{T}}}\right]\underline{\hat{\mathbf{T}}}^3 + \frac{1}{2}\left(\mathrm{tr}^2\left[\underline{\hat{\mathbf{T}}}\right] - \mathrm{tr}\left[\underline{\hat{\mathbf{T}}}^2\right]\right)\underline{\hat{\mathbf{T}}}^2 + \dots$$

$$-\frac{1}{6}\left(\mathrm{tr}^3\left[\underline{\hat{\mathbf{T}}}\right] - 3\mathrm{tr}\left[\underline{\hat{\mathbf{T}}}^2\right]\mathrm{tr}\left(\underline{\hat{\mathbf{T}}}\right) + 2\mathrm{tr}\left[\underline{\hat{\mathbf{T}}}^3\right]\right)\underline{\hat{\mathbf{T}}} + \det\left[\underline{\hat{\mathbf{T}}}\right]\underline{\mathbf{1}} = 0 \qquad \text{(B1)}$$

in which $\mathrm{tr}\left[\underline{\hat{\mathbf{T}}}\right]$ is the trace of matrix $\underline{\hat{\mathbf{T}}}$. It is seen from the above equation that $\underline{\hat{\mathbf{T}}}^4$ can be calculated in terms of lower powers of $\underline{\hat{\mathbf{T}}}$ as follow.

$$\underline{\hat{\mathbf{T}}}^4 = a_3^{'}\underline{\hat{\mathbf{T}}}^3 + a_2^{'}\underline{\hat{\mathbf{T}}}^2 + a_1^{'}\underline{\hat{\mathbf{T}}} + a_0^{'}\underline{\mathbf{1}} \qquad \text{(B2)}$$

The trace properties can be written in terms of their corresponding matrix as eigenvalues

$$\mathrm{tr}\left[\underline{\hat{\mathbf{T}}}\right] = \sum_m \lambda_m \,,\ \mathrm{tr}\left[\underline{\hat{\mathbf{T}}}^N\right] = \sum_m \lambda_m^N \,,\ \det\left[\underline{\hat{\mathbf{T}}}\right] = \prod_m \lambda_m \qquad \text{(B3)}$$

where $m = \{1,2,34\}$ in our case. Using Matrix trace properties and applying it to our transfer matrix with eigenvalues of the form $\lambda_i = e^{ik_i d}$ we would have

$$\mathrm{tr}\left[\underline{\hat{\mathbf{T}}}\right] = 2\cos(k_1 d) + 2\cos(k_2 d)$$

$$\mathrm{tr}\left[\underline{\hat{\mathbf{T}}}^N\right] = 2\cos(Nk_1 d) + 2\cos(Nk_2 d)$$

$$\det(\underline{\hat{\mathbf{T}}}) = 1 \qquad \text{(B4)}$$

By inserting the above values in the Cayley-Hamilton equation for $\underline{\hat{\mathbf{T}}}^4$ and after simplification we will get the following results for the coefficients of the equation:

$$a_0^{'} = -1$$

$$a_1^{'} = a_3^{'} = 2[\cos(k_1 d) + \cos(k_2 d)]$$

$$a_2^{'} = -2\left[1 + \cos\left((k_1 - k_2)d\right) + \cos\left((k_1 + k_2)d\right)\right] \qquad \text{(B5)}$$

It should be noted that exactly at DBE the above values will reduce to the following

$$a_0 = -1,\ a_1 = a_3 = -2,\ a_2 = -6$$

The equation (B2) shows that $\underline{\widehat{\mathbf{T}}}^{\mathrm{N}}$ can also be found in terms of $\underline{\widehat{\mathbf{T}}}$, $\underline{\widehat{\mathbf{T}}}^2$, and $\underline{\widehat{\mathbf{T}}}^3$ by using the formula for $\underline{\widehat{\mathbf{T}}}^4$ recursively. Therefore, we would have

$$\underline{\widehat{\mathbf{T}}}^{\mathrm{N}} = a_3\underline{\widehat{\mathbf{T}}}^3 + a_2\underline{\widehat{\mathbf{T}}}^2 + a_1\underline{\widehat{\mathbf{T}}} + a_0\underline{\mathbf{I}} \tag{B6}$$

in which a_0, a_1, a_2,a_3 are the coefficients to be found. These coefficients are found by imposing that the eigenvalues also satisfy (B6).

$$\lambda_m^N = a_3\lambda_m^3 + a_2\lambda_m^2 + a_1\lambda_m + a_0, m = 1,2,3,4 \tag{B7}$$

By inserting each eigenvalue into the above equation, we solve the following linear matrix equation to find the unknown coefficients a_i.

$$\begin{pmatrix} \lambda_1^3 & \lambda_1^2 & \lambda_1 & 1 \\ \lambda_2^3 & \lambda_2^2 & \lambda_2 & 1 \\ \lambda_3^3 & \lambda_3^2 & \lambda_3 & 1 \\ \lambda_4^3 & \lambda_4^2 & \lambda_4 & 1 \end{pmatrix} \begin{pmatrix} a_3 \\ a_2 \\ a_1 \\ a_0 \end{pmatrix} = \begin{pmatrix} \lambda_1^N \\ \lambda_2^N \\ \lambda_3^N \\ \lambda_4^N \end{pmatrix} \tag{B8}$$

We have $\lambda_i = e^{ik_i d}$ and also we know that $\lambda_3 = 1/\lambda_1$ and $\lambda_4 = 1/\lambda_2$. From the system of linear equations in (B8), the exact values for a_i coefficients are found in terms of the eigenvalues of the matrix $\underline{\widehat{\mathbf{T}}}$ as stated below.

$$a_0 = \frac{(\lambda_2^N - \lambda_2^{4-N})\lambda_1}{(\lambda_1-\lambda_2)(\lambda_1\lambda_2-1)({\lambda_2}^2-1)} - \frac{(\lambda_1^N - \lambda_1^{4-N})\lambda_2}{(\lambda_1-\lambda_2)(\lambda_1\lambda_2-1)({\lambda_1}^2-1)} \tag{B9}$$

$$a_1 = \frac{(\lambda_2^{3-N}(\lambda_1+\lambda_2+\lambda_1^2\lambda_2) - \lambda_2^N(1+\lambda_2\lambda_1+\lambda_1^2))}{(\lambda_1-\lambda_2)(\lambda_1\lambda_2-1)({\lambda_2}^2-1)} + \frac{(-\lambda_1^{3-N}(\lambda_1+\lambda_2+\lambda_2^2\lambda_1) + \lambda_1^N(1+\lambda_2\lambda_1+\lambda_2^2))}{(\lambda_1-\lambda_2)(\lambda_1\lambda_2-1)({\lambda_1}^2-1)} \tag{B10}$$

$$a_2 = \frac{\left(\lambda_2^N(\lambda_1+\lambda_2+\lambda_1^2\lambda_2)-\lambda_2^{3-N}(1+\lambda_2\lambda_1+\lambda_1^2)\right)}{(\lambda_1-\lambda_2)(\lambda_1\lambda_2-1)({\lambda_2}^2-1)} + \frac{\left(-\lambda_1^N(\lambda_1+\lambda_2+\lambda_2^2\lambda_1)+\lambda_1^{3-N}(1+\lambda_2\lambda_1+\lambda_2^2)\right)}{(\lambda_1-\lambda_2)(\lambda_1\lambda_2-1)({\lambda_1}^2-1)} \quad \text{(B11)}$$

$$a_3 = \frac{\lambda_1\lambda_2\left(({\lambda_1}^N-{\lambda_2}^{2-N})\right)}{(\lambda_1-\lambda_2)(\lambda_1\lambda_2-1)({\lambda_2}^2-1)} + \frac{\lambda_1\lambda_2\left(({\lambda_1}^{2-N}-{\lambda_2}^N)\right)}{(\lambda_1-\lambda_2)(\lambda_1\lambda_2-1)({\lambda_1}^2-1)} \quad \text{(B12)}$$

For the propagating and evanescent modes, we have the following Bloch wavenumbers near DBE.

$$k_1 \approx k_d + a(\omega-\omega_d)^{1/4} \quad \text{(B13)}$$

$$k_2 \approx k_d - ia(\omega-\omega_d)^{1/4} \quad \text{(B14)}$$

where a is a constant. We then use the above formulas to calculate the coefficients needed to derive $\underline{\widehat{\mathbf{T}}}^N$ in equation (B6). After taking the two lowest order terms in the Taylor series expansion for the coefficients a_i we find that

$$a_i \approx f_i(a,N) + g_i(a,N)(\omega-\omega_d) \quad \text{(B15)}$$

in which the functions $f_i(a,N)$ and $g_i(a,N)$ for $i=\{1,2,3,4\}$ are found as

$$f_i(a,N) = \begin{cases} -\frac{1}{6}(-1)^N N(2-3N+N^2), i=3 \\ -\frac{1}{2}(-1)^N N(3-4N+N^2), i=2 \\ -\frac{1}{2}(-1)^N N(6-5N+N^2), i=1 \\ -\frac{1}{6}(-1)^N(-6+11N-6N^2+N^3), i=0 \end{cases} \quad \text{(B16)}$$

and

$$g_i(a,N) = \begin{cases} -\frac{(-1)^N N}{5040}(6+7N-21N^2+14N^4-7N^5+N^6), i=3 \\ -\frac{(-1)^N N}{5040}(312-392N+42N^2+63N^4-28N^5+3N^6), i=2 \\ -\frac{(-1)^N N}{5040}(-906+1715N-903N^2+126N^4-35N^5+3N^6), i=1 \\ -\frac{(-1)^N N}{5040}(48-196N+294N^2-210N^3+77N^4-14N^5+N^6), i=0 \end{cases} \quad \text{(B17)}$$

For large N (N > 100) we only consider the higher order powers of N, which reduces the coefficients in (B16) and (B17) to

$$f_{0,3}(a,N) \approx -\frac{1}{6}(-1)^N N^3, f_{1,2}(a,N) \approx -\frac{1}{2}(-1)^N N^3 \tag{B18}$$

with

$$g_{0,3}(a,N) \approx -\frac{(-1)^N N^7}{5040}, g_{1,2}(a,N) \approx -\frac{(-1)^N N^7}{1680} \tag{B19}$$

The transmission coefficient for the x polarization namely t_{xx} can be thus written as

$$\begin{aligned} t_{xx} &= \vec{\mathbf{u}}_x^T \left(\frac{\underline{\underline{\mathbf{T}}}_{11N}}{\det\left[\underline{\underline{\mathbf{T}}}_{11N}\right]} \right) \vec{\mathbf{v}}_x^T \\ &= \frac{a_0 + a_1 t_{xx1} \det\left[\underline{\underline{\mathbf{T}}}_{11}\right] + a_2 t_{xx2} \det\left[\underline{\underline{\mathbf{T}}}_{112}\right] + a_3 t_{xx3} \det\left[\underline{\underline{\mathbf{T}}}_{113}\right]}{\det\left[\underline{\underline{\mathbf{T}}}_{11N}\right]} \end{aligned} \tag{B20}$$

References

[1] N. Marcuvitz and J. Schwinger, "On the Representation of the Electric and Magnetic Fields Produced by Currents and Discontinuities in Wave Guides. I," *J. Appl. Phys.*, vol. 22, no. 6, pp. 806–819, Jun. 1951, doi: 10.1063/1.1700052.

[2] L. B. Felsen and N. Marcuvitz, *Radiation and Scattering of Waves*. Hoboken, NJ: John Wiley & Sons, 1994.

[3] A. Figotin and I. Vitebskiy, "Electromagnetic unidirectionality in magnetic photonic crystals," *Phys. Rev. B*, vol. 67, no. 16, p. 165210, 2003, doi: 10.1103/PhysRevB.67.165210.

[4] A. Figotin and I. Vitebskiy, "Gigantic transmission band-edge resonance in periodic stacks of anisotropic layers," *Phys. Rev. E*, vol. 72, no. 3, p. 036619, Sep. 2005, doi: 10.1103/PhysRevE.72.036619.

[5] A. Figotin and I. Vitebskiy, "Frozen light in photonic crystals with degenerate band edge," *Phys. Rev. E*, vol. 74, no. 6, p. 066613, Dec. 2006, doi: 10.1103/PhysRevE.74.066613.

[6] A. Figotin and I. Vitebskiy, "Slow-wave resonance in periodic stacks of anisotropic layers," *Phys. Rev. A*, vol. 76, no. 5, p. 053839, Nov. 2007, doi: 10.1103/PhysRevA.76.053839.

[7] A. Figotin and I. Vitebskiy, "Slow light in photonic crystals," *Waves Random Complex Media*, vol. 16, no. 3, pp. 293–382, 2006, doi: 10.1080/17455030600836507.

[8] A. Figotin and I. Vitebskiy, "Slow wave phenomena in photonic crystals," *Laser Photonics Rev.*, vol. 5, no. 2, pp. 201–213, Mar. 2011, doi: 10.1002/lpor.200900049.

[9] J. Ballato, A. Ballato, A. Figotin, and I. Vitebskiy, "Frozen light in periodic stacks of anisotropic layers," *Phys. Rev. E Stat. Nonlin. Soft Matter Phys.*, vol. 71, no. 3 Pt 2B, p. 036612, Mar. 2005, doi: 10.1103/PhysRevE.71.036612.

[10] G. D'Aguanno, N. Mattiucci, M. Scalora, M. J. Bloemer, and A. M. Zheltikov, "Density of modes and tunneling times in finite one-dimensional photonic crystals: A comprehensive analysis," *Phys. Rev. E*, vol. 70, no. 1, p. 016612, Jul. 2004, doi: 10.1103/PhysRevE.70.016612.

[11] L. Novotny and B. Hecht, *Principles of Nano-Optics*. Cambridge: Cambridge University Press, 2006. doi: 10.1017/CBO9780511813535.

[12] A. A. Asatryan, K. Busch, R. C. McPhedran, L. C. Botten, C. Martijn de Sterke, and N. A. Nicorovici, "Two-dimensional Green's function and local density of states in photonic crystals consisting of a finite number of cylinders of infinite length," *Phys. Rev. E*, vol. 63, no. 4, p. 046612, Mar. 2001, doi: 10.1103/PhysRevE.63.046612.

[13] D. P. Fussell, R. C. McPhedran, C. M. Sterke, and A. A. Asatryan, "Three-dimensional local density of states in a finite two-dimensional photonic crystal composed of

cylinders.," *Phys. Rev. E Stat. Nonlin. Soft Matter Phys.*, vol. 67, no. 4 Pt 2, pp. 045601–045601, Apr. 2003, doi: 10.1103/physreve.67.045601.

[14] K. Joulain, R. Carminati, J.-P. Mulet, and J.-J. Greffet, "Definition and measurement of the local density of electromagnetic states close to an interface," *Phys. Rev. B*, vol. 68, no. 24, Dec. 2003, doi: 10.1103/PhysRevB.68.245405.

[15] M. A. K. Othman, F. Yazdi, A. Figotin, and F. Capolino, "Giant gain enhancement in photonic crystals with a degenerate band edge," *Phys. Rev. B*, vol. 93, no. 2, p. 024301, Jan. 2016, doi: 10.1103/PhysRevB.93.024301.

[16] E. P. Wigner, "Lower Limit for the Energy Derivative of the Scattering Phase Shift," *Phys. Rev.*, vol. 98, no. 1, pp. 145–147, Apr. 1955, doi: 10.1103/PhysRev.98.145.

[17] N. V. Bloch, K. Shemer, A. Shapira, R. Shiloh, I. Juwiler, and A. Arie, "Twisting Light by Nonlinear Photonic Crystals," *Phys. Rev. Lett.*, vol. 108, no. 23, p. 233902, Jun. 2012, doi: 10.1103/PhysRevLett.108.233902.

[18] A. Figotin and I. Vitebskiy, "Frozen light in photonic crystals with degenerate band edge," *Phys. Rev. E Stat. Nonlin. Soft Matter Phys.*, vol. 74, no. 6 Pt 2, p. 066613, Dec. 2006, doi: 10.1103/PhysRevE.74.066613.

[19] T. Katō, *Perturbation theory for linear operators*. Berlin: Springer, 1995.

[20] G. D'Aguanno, N. Mattiucci, M. Centini, M. Scalora, and M. J. Bloemer, "Electromagnetic density of modes for a finite-size three-dimensional structure," *Phys. Rev. E*, vol. 69, no. 5, p. 057601, May 2004, doi: 10.1103/PhysRevE.69.057601.

[21] P. Dennery and A. Krzywicki, *Mathematics for Physicists*, New York, NY: Courier Dover Publications, 1996.

CHAPTER 5

Triple Ladder Lumped Circuit with Sixth Order Modal Exceptional Degeneracy

Sec. 5.1 Motivation

We introduce a circuit topology based on a simple triple-ladder circuit realized with lumped reactive components that provides a sixth order degenerate band-edge (6DBE). The 6DBE is a special kind of sixth order exceptional point of degeneracy in a lossless and gainless ladder. This degeneracy provides a very flat band edge in the phase – frequency dispersion diagram. The proposed topology exhibits unique structured resonance features associated with a high loaded *Q*-factor. We investigate the Floquet-Bloch modes, and dispersion relation of an infinite length periodic triple-ladder using the transfer matrix formalism and we also provide the approximate analytic expressions of the eigenmodes and dispersion relation around the degenerate point based on Puiseux series expansion. We also investigate the filtering characteristics of a finite structure terminated with loads

to highlight the extraordinary properties of the 6DBE compared to the regular band edge (RBE) and the fourth order degenerate band edge (DBE). The circuit framework introduced here with a 6DBE can be exploited in designing novel high Q-factor oscillators, filters, and pulse shaping networks.

We show the theory of a periodic circuit that exhibits a sixth order degenerate band edge (6DBE) in the dispersion relation and explore the associated unique characteristics. The 6DBE is a point in the system parameter space at which six eigenmodes coalesce in both the eigenvalues and eigenvectors. We demonstrate a simple realization and design procedure to have a 6DBE, which can be easily applied to other technologies such as periodic microstrip transmission lines. Degeneracy in electromagnetic waveguides means that independent eigenmodes coalesce at a certain angular frequency, denoted by ω_h, and form a single degenerate mode. Mathematically, this special degeneracy is manifested when the system matrix describing propagation is defective and a complete basis of eigenvectors cannot be obtained [1], [2].

A special and well-known category of degeneracies in periodic structures is recognized as the fourth order degenerate band edge (DBE) where four periodic eigenstates coincide at the center or edge of the Brillouin zone [3]–[7]. The existence and characteristics of the fourth order DBE have been exhibited in various periodic structures including transmission lines and striplines [7]–[9], as well as metallic [10] and optical waveguides [11]–[14]. Experimental demonstrations of the DBE at microwave frequencies are in [7], [10]. In [15], a double ladder periodic lumped circuit is introduced to exhibit a DBE, explaining also the

advantages associated to it such as high quality factor and stability to load changes. In this chapter, we introduce a periodic lumped circuit based on a triple-ladder design that develops a sixth order degeneracy. This condition happens when six Floquet-Bloch modes (eigenstates) coalesce at the edge of the Brillouin zone. At this condition the dispersion relation around the degeneracy point is approximated by $(\omega_h - \omega) \propto (\varphi - \pi)^6$ in which φ is the shift in the phase from one unit cell of the periodic structure to its adjacent one, ω is the angular frequency, and ω_h is the frequency that features the sixth order degeneracy. We have shown in [16] that a novel oscillator design featuring DBE will lead to lower oscillation threshold and more robustness to the effects of loss and loading as opposed to devices featuring only regular band edge [6], [17] based on the enhanced quality factor associated to the DBE condition. Remarkable characteristics of the degeneracy condition in periodic structure including the significant decrease in the group velocity and sharp increase of the quality factor and local density of states [6], [16], will make this class of cavities with degeneracy suitable for a variety of applications ranging from sensors and filters to oscillator and pulse shaping circuits [18]–[22].

The occurrence of the sixth order degeneracy is demonstrated in a realistic optical photonic structure in [23]. In this chapter we focus on a simple circuit design with lumped elements which can support a 6DBE in its phase-frequency dispersion relation. We also focus on some important properties related to the loaded quality factor as discussed next. The unit cell design of the periodic structure proposed here comprises a six-port network composed of reactive components (capacitors and inductors) and has coupling between the branches as shown in Fig. 5.1(a). Due to the simplicity of the proposed unit cell, we are

able to offer the analytic formulation of the eigenvalues (hence the modes) based on the Puiseux fractional power series expansion around the degeneracy condition [24]. The general framework developed here is not limited to one specific design or application and can be potentially applied to various configurations featuring degenerate band edge phenomena.

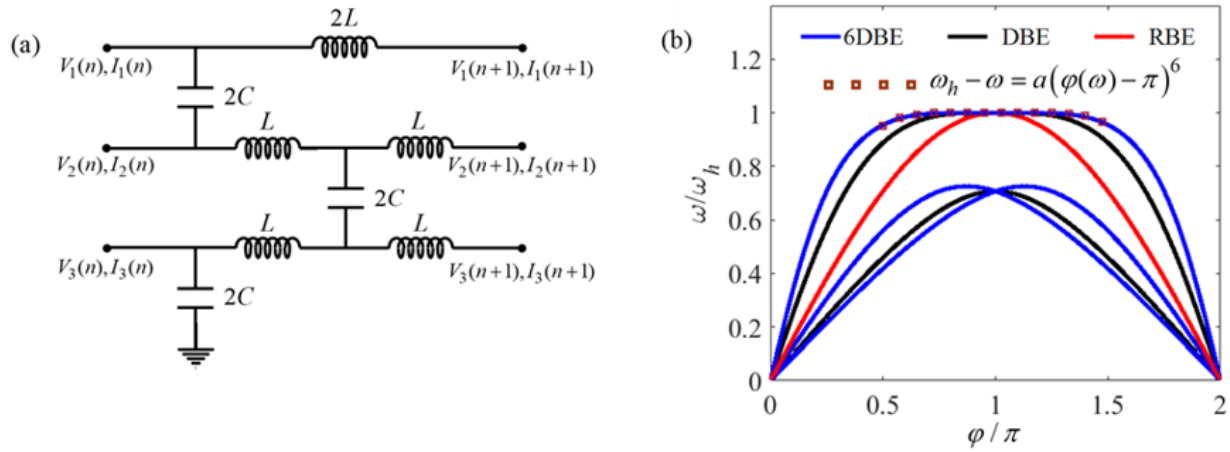

Fig. 5.1 (a) Unit cell of a periodic triple-ladder lumped circuit comprised of reactive lumped elements that develops a sixth order degeneracy at an angular frequency $\omega_h = 1/\sqrt{LC}$ (b) Dispersion diagram of the infinitely long periodic triple-ladder circuit exhibiting a 6DBE at angular frequency ω_h. The fitting curve shows analytically the flatness of the dispersion around the 6DBE. The 6DBE is flatter than the DBE and RBE. The result is obtained by F. Yazdi in Matlab.

In Section 5.2 we introduce the triple-ladder circuit and provide a detailed investigation of the modes and dispersion relation around the degeneracy condition for the infinitely long periodic circuit. An approximation of the system's eigenvalues based on the Puiseux series expansion is also provided. In Section 5.3 we investigate the finite-length structure's properties including the transfer function of the system and its resonance behavior around the 6DBE. We also account for the effects of losses as well as Q-factor scaling with the

length of the resonator, including loss/loading effects, analogously to what was done for the 4th order DBE in [15].

Sec. 5.2 Triple Ladder Circuit Theory

The proposed design for the unit cell of a periodic circuit that can support a sixth order degeneracy is presented in Fig. 5.1(a), composed of eight reactive components (five inductors and three capacitors) that comprises a six-port network. As shown in Fig. 5.1(a) the coupling between the three ladders is provided by the capacitors and this design will develop a 6DBE at angular frequency of $\omega_h = 1/\sqrt{LC}$. After designing the unit cell featuring 6DBE at the desired frequency with practical values for inductors and capacitors, we will study the modal characteristics and dispersion relation of the triple ladder circuit in the following subsection where we also provide the mathematical analysis of the system's behavior in the vicinity of the degeneracy condition. For all the numerical results provided in this chapter, we are assuming the values of C = 56 pF and L = 45 nH in our unit cell design featuring a 6DBE at the frequency of f_h = 100.26 MHz.

A. State Vector and Dispersion Relation

To investigate the modal characteristics (namely, eigenvalues and eigenvectors) of the periodic structure, we exploit the transfer matrix formalism which relates the voltages and current from one unit cell to the next. In order to do so, we have defined the state vector $\boldsymbol{\Psi}(n)$ as a 6×1 vector comprising of the voltages and current phasors at the three input ports of the arbitrary *n*-th unit cell shown in Fig. 5.1(a). Thus, the state vector $\boldsymbol{\Psi}(n)$ can be represented as:

$$\boldsymbol{\Psi}(n) = [V_1(n) \quad V_2(n) \quad V_3(n) \quad I_1(n) \quad I_2(n) \quad I_3(n)]^T \tag{5.1}$$

The state vector defined in (5.1), is then translated across the unit cell by the 6×6 transfer matrix $\underline{\mathbf{T}}$, which describes the evolution of the state vector over the unit cell following the equation

$$\boldsymbol{\Psi}(n+1) = \underline{\mathbf{T}}\boldsymbol{\Psi}(n) \tag{5.2}$$

The detailed calculation of the transfer matrix for the triple ladder circuit proposed in Fig. 5.1(a) is provided in Appendix where we construct the total transfer matrix of the unit cell based on the transfer function derived for each element.

As discussed in [15] for infinitely long periodic circuits, we have periodic solutions for the eigenstates where the transformation of the state vector $\boldsymbol{\Psi}(n)$ from location n (or at n-th unit cell) to the state vector $\boldsymbol{\Psi}(n+1)$ at location n+1 (or at (n+1)-th unit cell), is described by $\boldsymbol{\Psi}(n+1) = e^{-j\varphi(\omega)}\boldsymbol{\Psi}(n)$, in which $\varphi(\omega)$ for the lossless structure is simply the Floquet- Bloch phase shift between two consecutive unit cells [15]. In general, for the triple ladder network we get six different solutions for $\varphi(\omega)$ at each frequency, each of which is associated with a Floquet-Bloch mode of the system. For an infinitely long periodic circuit, those periodic solutions and hence the dispersion relation (between the phase shift and the frequency) can be obtained by solving the eigenvalue equation

$$\left[\underline{\mathbf{T}} - e^{-j\varphi(\omega)}\underline{\mathbf{I}}\right]\boldsymbol{\Psi}(n) = 0 \tag{5.3}$$

in which $\underline{\mathbf{I}}$ is the 6×6 identity matrix. The dispersion diagram of the circuit made of an infinite number of unit cells, shown in Fig. 5.1(a), is plotted in Fig. 5.1(b). This plot shows

only the eigenstates with purely real phase shift $\varphi(\omega)$ normalized to π versus normalized angular frequency. The proposed unit cell exhibits a 6DBE at the angular frequency $\omega_h = 1/\sqrt{LC}$ and phase shift of $\varphi(\omega_h) = \pi$. The 6DBE is observed by the flatness of the blue lines in Fig. 5.1(b); six Floquet-Bloch modes (eigenstates) coalesce at the edge of the Brillouin zone. To see the full coalescence at $\varphi(\omega_h) = \pi$, we would need to plot also the branches with complex $\varphi(\omega)$ that are omitted in this figure for simplicity. Around the 6DBE condition, the dispersion relation is well approximated by $(\omega_h - \omega) \propto (\varphi - \pi)^6$ as shown in the results of the Fig. 5.1(b) as expected by the order of the degeneracy. To better perceive the flatness associated to the 6DBE condition in comparison to lower orders of degeneracy, the dispersion diagrams for the circuits exhibiting DBE and RBE are also depicted in Fig. 5.1(b) where we consider the double-ladder and single-ladder circuits designs provided in and we use the same values as in our 6DBE design for the components to get DBE and RBE respectively.

B. Analysis of the System's Behavior Around 6DBE

We provide an analytical approach to approximate the perturbed eigenvalues of the system and hence the dispersion relation when moving away from the ideal degeneracy condition due to the frequency perturbation, although the analytical framework provided here can be applied to other types of perturbations such as losses introduced to the circuit's elements as well. For the sake of our frequency perturbation analysis, we consider a lossless circuit and assume a change of the frequency of operation slightly away from the 6DBE angular frequency ω_{h}, described by $\delta_\omega = (\omega - \omega_h)/\omega_h$. The eigenstates of the

system (eigenvalues $\lambda = \exp(-j\varphi)$ of the of the transfer matrix $\underline{\mathbf{T}}$) are then be approximated using the Puiseux fractional power series expansion around the ideal (unperturbed) degenerate eigenvalue $\lambda_h = -1$, following the equation [2], [24]:

$$\lambda_p(\delta_\omega) = \lambda_h + \sum_{k=1}^{\infty} \alpha_k \left(\zeta^p \delta_\omega^{1/6}\right)^k \tag{5.4}$$

Here, $p = 1,2,\ldots,6$ and $\zeta = exp(j\pi/3)$ provide six different solutions for the perturbed eigenvalues. The Puiseux series coefficients, α_k, are calculated using the general recursive formulas provided in [24]. The first two series coefficients are obtained using the following formulas

$$\alpha_1 = \left(-\frac{\frac{\partial D}{\partial \delta_\omega}(0,\lambda_h)}{\frac{1}{6!}\frac{\partial^6 D}{\partial \lambda^6}(0,\lambda_h)}\right)^{1/6} \neq 0,$$

$$\alpha_2 = \frac{-\left(\alpha_1^7 \frac{1}{7!}\frac{\partial^7 D}{\partial \lambda^7}(0,\lambda_h) + \alpha_1 \frac{\partial^2 D}{\partial \lambda \partial \delta_\omega}(0,\lambda_h)\right)}{6\alpha_1^5 \left(\frac{1}{6!}\frac{\partial^6 D}{\partial \lambda^6}(0,\lambda_h)\right)}, \tag{5.5}$$

in which $D(\delta_\omega, \lambda)$ is the characteristic equation of the transfer matrix $\underline{\mathbf{T}}$ defined as:

$$D(\delta_\omega, \lambda) = \det(\lambda \underline{\mathbf{I}} - \underline{\mathbf{T}}(\delta_\omega)) \, ; D(\delta_\omega, \lambda) = \sum_{l=0}^{6} b_l \lambda^l \tag{5.6}$$

This is the sixth order polynomial of λ and the coefficients b_l are calculated using the applications of the Cayley-Hamilton theorem [25] stating that every square matrix satisfies its own characteristic equation. Due to reciprocity of the system, if λ_i is a solution, then $1/\lambda_i$ must also be a solution. Exactly at the 6DBE condition, all the eigenvalues λ_i are equal, i.e., $\lambda_i = \lambda_h$, hence the only possible solution is either $\lambda_h = 1$ (i.e., at the edge of the Brillouin zone defined as $[0 \quad 2\pi]$) or $\lambda_h = -1$ (i.e., at the center of the Brillouin zone).

Considering the 6DBE at the center, i.e., $\lambda_h = -1$, the first two Puiseux series coefficients for the periodic triple-ladder circuit design of the unit cell shown in Fig. 5.1(a) are calculated and heavily simplified as

$$\alpha_1 = \sqrt[6]{128}\,, \alpha_2 = -\sqrt[3]{16} \tag{5.7}$$

By substituting the values of the coefficients calculated previously in equation (5.4), the six eigenvalues around the 6DBE can be approximated using:

$$\lambda_p(\delta_\omega) \approx \lambda_h + \alpha_1 \left(\zeta^p {\delta_\omega}^{\frac{1}{6}}\right) + \alpha_2 \left(\zeta^p {\delta_\omega}^{\frac{1}{6}}\right)^2 \tag{5.8}$$

where we only consider the first three terms of the expansion which provides a decent approximation around 6DBE though more terms can be added to achieve more accurate approximations. Exploiting the results of the Puiseux series approximation of the eigenvalues and having $\lambda = \exp(-j\varphi)$, the dispersion relation (φ, ω) of the circuit can also be approximated as Puiseux series in terms of fractional powers of the frequency perturbation. By considering only the first coefficient of the Puiseux series, the dispersion relation can be written as: $(\varphi - \pi) \approx \alpha_1(\omega - \omega_h)^{1/6}$ and by rearranging the derived dispersion relation we will get:

$$(1 - \omega/\,\omega_h) \approx \eta(1 - \varphi/\pi)^6 \tag{5.9}$$

in which η is a dimensionless parameter named "flatness factor" associated to the sixth derivative of ω with respect to φ at ω_h, indicating the flatness of the dispersion diagram at the exceptional point of degeneracy. For the circuit proposed in this chapter, the flatness factor η for the normalized dispersion relation is calculated to be equal to $\pi^6/128$. It is

worth noting that the flatness factor η does not depend on the values of the circuit parameters, namely L and C, thus changing the values of L and C will result in the same "normalized" dispersion relation and flatness factor around ω_h. Fig. 5.2 shows the complex dispersion diagram showing both the real and the imaginary branches of $\varphi(\omega)$, assuming an infinite periodic triple-ladder circuit comprised of the unit cell shown in Fig. 5.1(a). The red curves represent the approximated dispersion diagram derived via the first order Puiseux series approximation of the eigenvalues, while the blue curves represent the exact numerically calculated dispersion relation. The dispersion relation plots of Fig. 5.2 reveal that a very good agreement is attained between the numerical results and analytical approximation provided in this section around the sixth order degeneracy condition by exploiting only the first term of the Puiseux series.

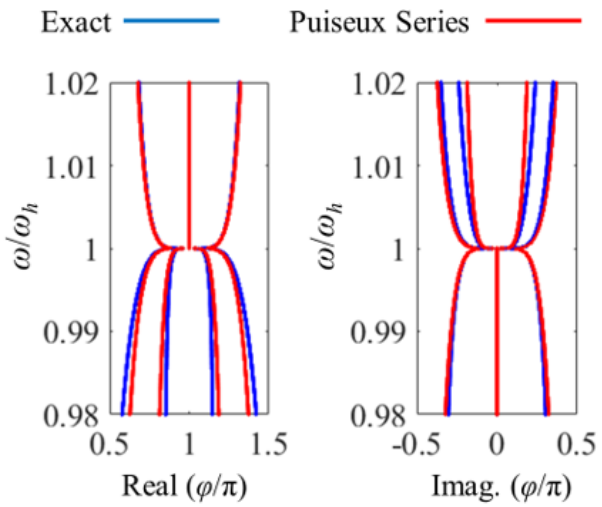

Fig. 5.2 Complex dispersion relation of the infinite periodic circuit based on Puiseux series approximation (shown in solid red) in comparison with exact numerical dispersion relation (shown in solid blue) for the lossless circuit. The propagation phase angle φ is a generally complex number, both the real and imaginary parts are shown. The result are obtained by F. Yazdi.

Sec. 5.3 Resonance Behavior of the Periodic Circuit

To investigate the resonance behavior of the circuit with sixth order modal degeneracy of Fig. 5.1(a), we consider a finite-length structure made by cascading N unit cells as shown in Fig. 5.3. We consider the triple-ladder structure with proper excitations and terminations to analyze some of its important characteristics, which include the voltage transfer function, loaded quality factor, and effect of loss, as discussed in the following section.

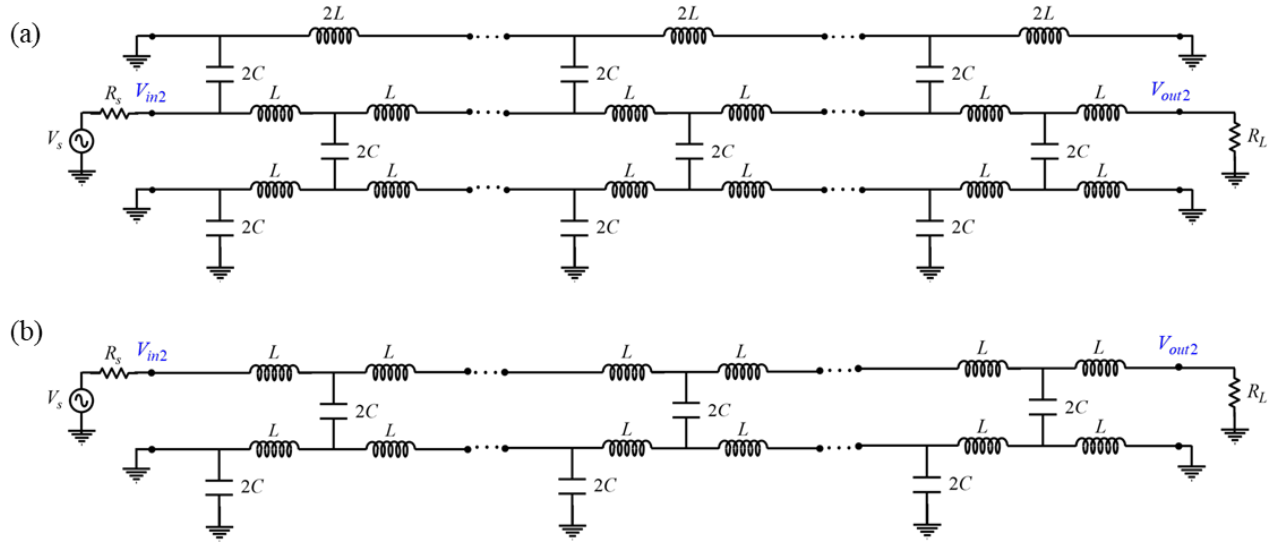

Fig. 5.3 (a) Triple ladder and (b) double ladder periodic LC circuits with finite length made of N unit cells with excitation voltage V_s, source resistance of $R_s = 50\Omega$, and load resistance of R_L at the second (middle) ladder.

The scattering parameter (S_{21}) of the finite circuit relating the output and incident input voltages at the desired ports is obtained from the transfer matrix formalism. In our analysis of the resonance behavior of the 6DBE circuit we consider the middle ladder for our

input/output terminals and the voltage transmission coefficient (or S_{21} parameter) is then defined as

$$S_{21} = \frac{V_{\text{out2}}}{V_{\text{incident2}}} \tag{5.10}$$

where V_{out2} is the voltage at the second ladder's output resistive load Z_{L2} and $V_{\text{incident2}}$ is the incident input voltage of the second ladder as $V_{incident2} = (V_{in} + I_{in2} \times R_s)/2$. Hence, we only excite the second ladder as in Fig. 5.3, and we assume that $Z_{s2} = Z_{\text{L2}} = 50\Omega$, while all the other terminals are short circuited. The magnitude of the S_{21} parameter is plotted versus the normalized angular frequency around the 6DBE frequency for the finite length circuits with different numbers of unit cells (N) in Fig. 5.4(a) where the results are shown for N=8 in dashed blue, N=10 in dotted black, and N=12 in solid red. We observe multiple resonance peaks near the 6DBE angular frequency ω_h, where the sharpest and the closest to ω_h is called the 6DBE resonance denoted by $\omega_{r,h}$ and this resonance features higher loaded quality factor (Q_{tot}) compared to other resonances. As the number of unit cells (N) increases, the 6DBE resonance peak moves closer to ω_h and becomes sharper, resulting in higher quality factors.

Next, we investigate the impact of another sort of perturbation, losses in the system, especially on the S_{21} parameter. The presence of losses impacts the quality factor of the lumped structure due to the high sensitivity to perturbations near the 6DBE. We now study the effect of introducing a finite quality factor of the lumped components, where for simplicity we assume that all the elements have the same quality factor Q_e.

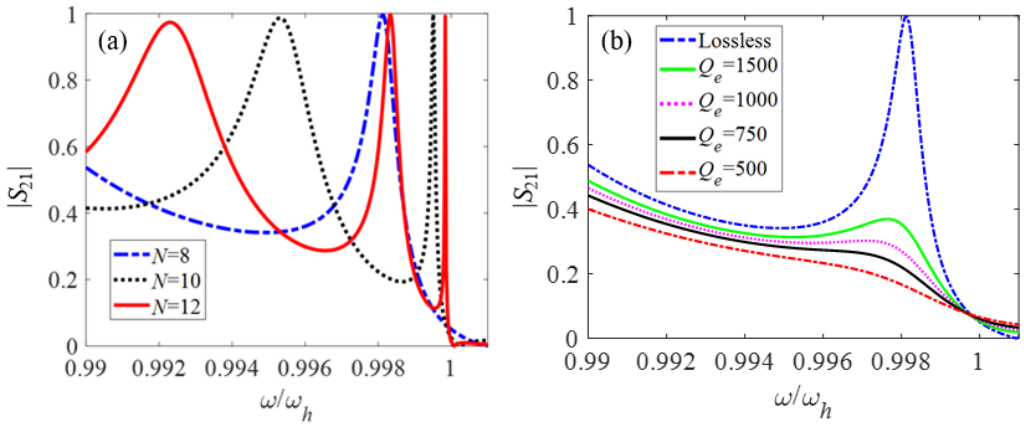

Fig. 5.4 The scattering parameter, S_{21}, of the circuit shown in Fig. 5.3 for (a) different number of unit cells and no loss in the elements and (b) different quality factors for elements in an N = 8 unit cells resonator. The important resonance is the one closest to ω_h, denoted as $\omega_{r,h}$. The Matlab result are obtained by F. Yazdi and A. Nikzamir.

In Fig. 5.4(b) we show the magnitude of S_{21} parameter of the triple ladder made of 8 unit cells, i.e., N = 8, for different Q_e, where we plot the magnitude of S_{21} parameter with and without considering the loss effects. Furthermore, as can be seen from Fig. 5.4(b) when losses are introduced into each L and C in the circuit, the quality factor of the resonance associated to 6DBE significantly declines, compared to other resonances of the circuit. Increasing losses beyond a certain limit deteriorates the 6DBE resonance, and the transfer function's peak will completely vanish for sufficiently low Q_e, as for the case with Q_e = 500 in Fig. 5.4(b). This is still a high quality factor for most of the available lumped components but at the same time it is important to well understand the limiting factors to realize resonances in lumped ladder circuits. Furthermore, high values of high quality factors can be realized in several technologies when using distributed elements, as in wave propagation in waveguides, and the results in this chapter can be helpful to better understand the physics of cavities using waveguides with a 6DBE. Finally, it is also

customary to use lumped elements to approximated realistic waveguide structures when performing time domain simulation using certain commercial software, like Candence etc., further justifying the importance of this study.

B. Quality Factor Analysis

As mentioned earlier, one of the main advantages of the topologies exhibiting higher orders of degeneracy (here of order sixth) is the enhanced quality factor compared to designs in the same technology featuring only RBE or DBE. Therefore, the theoretical investigation of the *Q*-factor is valuable in delivering an inclusive analysis of the performance of the 6DBE triple ladder circuit, where we study the effect of losses as well as the length of the periodic triple ladder resonator circuit in the loaded quality factor Q_{tot}. Here the loaded *Q*-factor is defined for the finite-length circuit with port terminations of 50Ω resistive loads and introduced losses to reactive elements of the circuit. In our *Q*-factor analysis we are interested in the loaded quality factor associated to the 6DBE resonance frequency of $\omega_{r,h}$ defined as [26]:

$$Q_{\text{tot}} = \omega_{r,h} \frac{W_e + W_m}{P_l} \tag{5.11}$$

in which P_l is the power loss defined as the time-average dissipated power due to the elements' losses as well as resistive loads, W_e and W_m are the total stored energy in the capacitors and inductors of the resonator circuit, respectively, and $\omega_{r,h}$ is the finite length resonance angular frequency describing the 6DBE resonance. A thorough study of the loaded quality factor for a double ladder circuit featuring the DBE for the lossless and lossy

[16] cases was provided. Here, we consider the loaded Q-factor of the triple ladder circuit exhibiting 6DBE for both lossless and lossy cases and compare the results to that of the 4DBE structures. First, we explore the limiting effect of losses on the Q-factor. The losses are introduced as finite quality factor Q_e for the L is modeled using the series resistance to element and for the C is modeled using the parallel resistance to element of the circuit in our simulations. In Fig. 5.5(a), the total loaded Q-factor, Q_{tot}, is plotted versus the elements' quality factor, Q_e, for different circuits lengths N where we assume the same Q_e for all the inductors and capacitors. As observed in the results of Fig. 5.5(a), by increasing Q_e, Q_{tot} initially increases linearly, and when increasing Q_e after a certain level (depending on the size of the circuit) the curves slightly decreases because of the effect of the 50Ω resistive loads at the terminals. While as discussed in [15], the Q_{tot} has slight dependency on the load terminations for the resonance associated to the degeneracy condition, by using very low impedance (e.g. short circuit) or very high impedance (e.g. open circuit) terminating loads, the Q_{tot} of the circuit might be enhanced, though this approach will lessen the amount of power available at the load terminals which is the case for our 6DBE triple-ladder circuit as well. Hence, here in our analysis and simulations we are assuming commonly used resistive load values of 50Ω as our terminations.

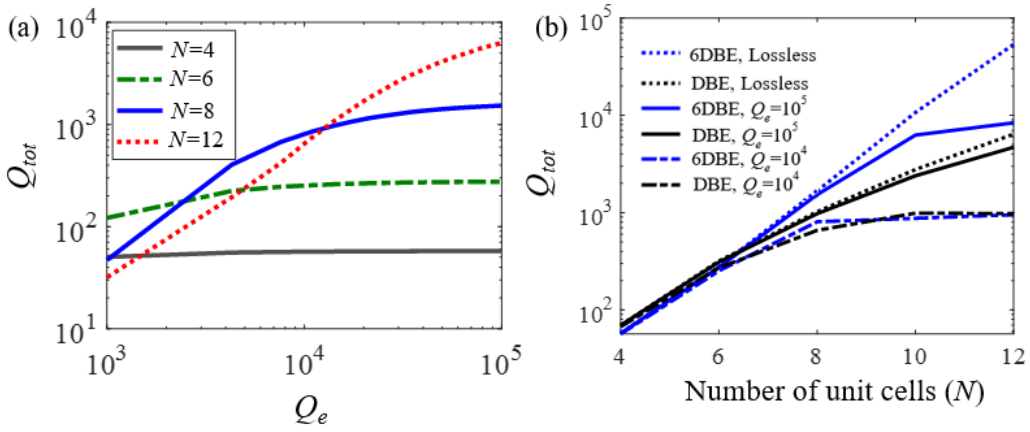

Fig. 5.5 Loaded quality factor, Q_{tot}, versus element quality factor for different number of unit cells (N) (b) Loaded quality factor, Q_{tot}, versus the number of unit cells (N), for different elements' quality factors. The results are obtained by A. Nikzamir and F. Yazdi.

Afterwards, we want to gain a better understanding of how the total Q-factor of the 6DBE circuit is affected by changing the length N and loss of the elements in comparison to the DBE circuit (which has a 4^{th} order degeneracy). In Fig. 5.5(b) we have plotted the Q_{tot} versus the number of unit cells N in the periodic circuit for both the 6DBE triple-ladder and the DBE double-ladder resonator circuits for lossless, as well as for two different lossy cases, with $Q_e = 10^4$ and $Q_e = 10^5$. As shown in [15] for the lossless double ladder circuit with DBE, Q_{tot} is asymptotically proportional to N^5 for large enough lengths N. This was also the case for other structures exhibiting DBE as shown in [10], [27], [28]. Instead, our analysis of the triple ladder 6DBE circuit demonstrates the proportionality of N^7 for Q_{tot}, for large numbers of unit cells in the lossless circuit. Consequently, the advantage of 6DBE scheme is better observed for larger ladder lengths as shown in Fig. 5.5(b) where, for example, for the $N = 12$ unit cells the Q_{tot} of the lossless 6DBE design is almost one order of magnitude higher than that of the DBE scheme providing a substantial improvement.

However, for the cases with lossy reactive elements, the loaded quality factor does not grow indefinitely with N^7 and it is rather limited by the finite quality factor of the elements as shown in Fig 5.5(b) for $Q_e = 10^4$ and $Q_e = 10^5$. Therefore, as observed from the results of our analysis, the quality factor for the lossy cases grows exponentially only for small values of N, then declines and becomes saturated for larger values of N. For $Q_e = 10^4$, Q_{tot} shows little variation with N since it is already very low, however, the advantage of the 6DBE over the 4^{th} order DBE schemes in terms of higher Q-factor is observed even when loss is present. The Q-factor results of both Fig. 5.5 plots are calculated for the case where we only excite the second ladder of the 6DBE triple ladder circuit, with the assumption of $R_s = R_L = 50\Omega$ and short circuit for all the other ports as shown in Fig. 5.3 (b). For the DBE circuit results, the excitation is at the top line with the assumption of $R_s = R_L = 50\Omega$ and short circuit for the bottom line's terminations as shown in Fig. 5.3(a).

Sec. 5.4 Conclusion

We have presented a new resonator concept made by cascading unit cells of a simple triple-ladder circuit periodically. This leads to a degeneracy of order sixth (6DBE) in its phase-frequency dispersion relation. The proposed design exploits the fascinating features and enhancements of higher order degeneracies over previously introduced designs with double ladder (exhibiting DBE) and single ladder (exhibiting only RBE) circuits particularly in terms of Q-factor and sensitivity to perturbations. We have provided an in-depth investigation of the modes and dispersion relation based on the state vector and transfer matrix formalism of the infinitely long periodic circuit. We have also provided the

analytical framework for the Puiseux fractional power series expansion of the system's eigenvalues around the degeneracy condition. The approximation of the dispersion diagram obtained when using the Puiseux series demonstrates a remarkable agreement with the dispersion obtained numerically, for frequencies close to the 6DBE one. The analytical framework established here may be applied to a variety of structure designs and applications featuring degeneracy condition specifically, but not limited to, sixth order and will be a useful tool in designing and evaluating novel designs for high Q-factor, oscillators, sensory and filter applications.

Appendix A Transfer Matrix Formalism and Calculation

In this Appendix the detailed calculation of the transfer matrix formalism is provided. The transfer matrix, $\underline{\mathbf{T}}$, of the unit cell of the triple ladder circuit shown in Fig. 5.1(a) and defined in Section 5.2 is obtained by multiplying the 6×6 transfer matrices of each element calculated based on the state vector definition in the proper order as:

$$\underline{\mathbf{T}} = \underline{\mathbf{T}}_{C1}\underline{\mathbf{T}}_{L1}\underline{\mathbf{T}}_{L2}\underline{\mathbf{T}}_{L3}\underline{\mathbf{T}}_{C2}\underline{\mathbf{T}}_{L4}\underline{\mathbf{T}}_{L5}\underline{\mathbf{T}}_{C3} \tag{A1}$$

The calcuation of $\underline{\mathbf{T}}$ is burdensome and after simplifications it will result in the following matrix:

$$\underline{\mathbf{T}} = \begin{bmatrix} 1-4\Gamma & 4\Gamma & 0 & Z_L & 0 & 0 \\ 4\Gamma(1-\Gamma) & \Gamma(4\Gamma-6)+1 & 2\Gamma & 0 & Z_L(1-\Gamma) & Z_L\Gamma \\ 4\Gamma^2 & \Gamma(2-4\Gamma) & 1-2\Gamma & 0 & Z_L\Gamma & Z_L(1-\Gamma) \\ Y_C & -Y_C & 0 & 1 & 0 & 0 \\ Y_C(2\Gamma-1) & -2Y_C(\Gamma-1) & -Y_C & 0 & 1-2\Gamma & 2\Gamma \\ 8Y_C\Gamma(2\Gamma-1) & -Y_C(1-2\Gamma)^2 & -2Y_C(\Gamma-1) & 0 & \Gamma(2-4\Gamma) & \Gamma(4\Gamma-6)+1 \end{bmatrix} \tag{A2}$$

where $\Gamma = LC\omega^2 = (\omega/\omega_h)^2$, $Z_L = 2j\omega L$, and $Y_C = 2j\omega C$. Using the formulation described above, the transfer matrix of the one unit cell of the lossless circuit evaluated exactly at 6DBE frequency is calculated to be:

$$\underline{\mathbf{T}}_0 = \begin{bmatrix} -3 & 4 & 0 & 2j\sqrt{\frac{L}{C}} & 0 & 0 \\ 0 & -1 & 2 & 0 & 0 & 2j\sqrt{\frac{L}{C}} \\ 4 & -2 & -1 & 0 & 2j\sqrt{\frac{L}{C}} & 0 \\ 2j\sqrt{\frac{C}{L}} & -2j\sqrt{\frac{C}{L}} & 0 & 1 & 0 & 0 \\ 2j\sqrt{\frac{C}{L}} & 0 & -2j\sqrt{\frac{C}{L}} & 0 & -1 & 2 \\ 4j\sqrt{\frac{C}{L}} & -2j\sqrt{\frac{C}{L}} & 0 & 0 & -2 & -1 \end{bmatrix} \tag{A3}$$

The ideal or unperturbed transfer matrix $\underline{\mathbf{T}}_0$ represented above can be written in the Jordan canonical form of $\underline{\mathbf{T}}_0 = \underline{\mathbf{V}}\underline{\mathbf{J}}\underline{\mathbf{V}}^{-1}$ in which $\underline{\mathbf{J}}$ has the form of

$$\underline{\mathbf{J}} = \begin{pmatrix} -1 & 1 & 0 & 0 & 0 & 0 \\ 0 & -1 & 1 & 0 & 0 & 0 \\ 0 & 0 & -1 & 1 & 0 & 0 \\ 0 & 0 & 0 & -1 & 1 & 0 \\ 0 & 0 & 0 & 0 & -1 & 1 \\ 0 & 0 & 0 & 0 & 0 & -1 \end{pmatrix} \tag{A4}$$

References

[1] N. Dunford, J. T. Schwartz, W. G. Bade, and R. G. Bartle, *Linear operators*. New York: Wiley intersciense, 1958.

[2] T. Kato, *Perturbation theory for linear operators*. Verlag, NY: Springer Science & Business Media, 2013.

[3] A. Figotin and I. Vitebskiy, "Slow light in photonic crystals," *Waves Random Complex Media*, vol. 16, no. 3, pp. 293–382, 2006, doi: 10.1080/17455030600836507

[4] A. Figotin and I. Vitebskiy, "Slow wave phenomena in photonic crystals," *Laser Photonics Rev.*, vol. 5, no. 2, pp. 201–213, 2011, doi: 10.1002/lpor.200900049.

[5] M. A. Othman and F. Capolino, "Demonstration of a degenerate band edge in periodically-loaded circular waveguides," *IEEE Microw. Wirel. Compon. Lett.*, vol. 25, no. 11, pp. 700–702, 2015, doi: 10.1109/TMTT.2017.2706271

[6] M. A. K. Othman, F. Yazdi, A. Figotin, and F. Capolino, "Giant gain enhancement in photonic crystals with a degenerate band edge," *Phys. Rev. B*, vol. 93, no. 2, p. 024301, Jan. 2016, doi: 10.1103/PhysRevB.93.024301.

[7] A. F. Abdelshafy, M. A. K. Othman, D. Oshmarin, A. T. Almutawa, and F. Capolino, "Exceptional Points of Degeneracy in Periodic Coupled Waveguides and the Interplay of Gain and Radiation Loss: Theoretical and Experimental Demonstration," *IEEE Trans. Antennas Propag.*, vol. 67, no. 11, pp. 6909–6923, Nov. 2019, doi: 10.1109/TAP.2019.2922778.

[8] C. Löcker, K. Sertel, and J. L. Volakis, "Emulation of propagation in layered anisotropic media with equivalent coupled microstrip lines," *Microw. Wirel. Compon. Lett. IEEE*, vol. 16, no. 12, pp. 642–644, 2006.

[9] J. L. Volakis and K. Sertel, "Narrowband and Wideband Metamaterial Antennas Based on Degenerate Band Edge and Magnetic Photonic Crystals," *Proc. IEEE*, vol. 99, no. 10, pp. 1732–1745, Oct. 2011, doi: 10.1109/JPROC.2011.2115230.

[10] M. A. K. Othman, X. Pan, G. Atmatzakis, C. G. Christodoulou, and F. Capolino, "Experimental Demonstration of Degenerate Band Edge in Metallic Periodically Loaded Circular Waveguide," *IEEE Trans. Microw. Theory Tech.*, vol. 65, no. 11, pp. 4037–4045, Nov. 2017, doi: 10.1109/TMTT.2017.2706271.

[11] N. Gutman, C. Martijn de Sterke, A. A. Sukhorukov, and L. C. Botten, "Slow and frozen light in optical waveguides with multiple gratings: Degenerate band edges and stationary inflection points," *Phys. Rev. A*, vol. 85, no. 3, Mar. 2012, doi: 10.1103/PhysRevA.85.033804.

[12] M. G. Wood, J. R. Burr, and R. M. Reano, "Degenerate band edge resonances in periodic silicon ridge waveguides," *Opt. Lett.*, vol. 40, no. 11, pp. 2493–2496, 2015.

[13] M. Y. Nada, M. A. K. Othman, and F. Capolino, "Theory of coupled resonator optical waveguides exhibiting high-order exceptional points of degeneracy," *Phys. Rev. B*, vol. 96, no. 18, p. 184304, Nov. 2017, doi: 10.1103/PhysRevB.96.184304.

[14] M. Y. Nada, M. A. K. Othman, O. Boyraz, and F. Capolino, "Giant Resonance and Anomalous Quality Factor Scaling in Degenerate Band Edge Coupled Resonator Optical Waveguides," *J. Light. Technol.*, vol. 36, no. 14, pp. 3030–3039, Jul. 2018, doi: 10.1109/JLT.2018.2822600.

[15] J. T. Sloan, M. A. K. Othman, and F. Capolino, "Theory of Double Ladder Lumped Circuits with Degenerate Band Edge," *IEEE Trans. Circuits Syst. Regul. Pap.*, vol. 65, no. 1, pp. 3–13, Jan. 2018, doi: 10.1109/TCSI.2017.2690971.

[16] D. Oshmarin *et al.*, "A New Oscillator Concept Based on Band Edge Degeneracy in Lumped Double-Ladder Circuits," *IET Circuits Devices Amp Syst.*, vol. 13, no. 7, pp. 950–957, 2019, doi: 10.1049/iet-cds.2018.5048.

[17] J. P. Dowling, M. Scalora, M. J. Bloemer, and C. M. Bowden, "The photonic band edge laser: A new approach to gain enhancement," *J. Appl. Phys.*, vol. 75, no. 4, pp. 1896–1899, Feb. 1994, doi: 10.1063/1.356336.

[18] G. L. Matthaei, L. Young, and E. M. Jones, "Design of microwave filters, impedance-matching networks, and coupling structures. Volume 2," DTIC Document, 1963.

[19] E. A. Guillemin, *Synthesis of passive networks: theory and methods appropriate to the realization and approximation problems*. RE Krieger Pub. Co., 1977.

[20] B. Razavi, *Design of Integrated Circuits for Optical Communications*. Hoboken, NJ: Wiley, 2012.

[21] V. A. Tamma, A. Figotin, and F. Capolino, "Concept for Pulse Compression Device Using Structured Spatial Energy Distribution," *IEEE Trans. Microw. Theory Tech.*, vol. 64, no. 3, pp. 742–755, Mar. 2016, doi: 10.1109/TMTT.2016.2518160.

[22] A. F. Abdelshafy, D. Oshmarin, M. A. K. Othman, M. M. Green, and F. Capolino, "Distributed Degenerate Band Edge Oscillator," *IEEE Trans. Antennas Propag.*, vol. 69, no. 3, pp. 1821–1824, Mar. 2021, doi: 10.1109/TAP.2020.3018539.

[23] M. Y. Nada and F. Capolino, "Exceptional point of sixth-order degeneracy in a modified coupled-resonator optical waveguide," *JOSA B*, vol. 37, no. 8, pp. 2319–2328, Aug. 2020, doi: 10.1364/JOSAB.385198.

[24] A. Welters, "On Explicit Recursive Formulas in the Spectral Perturbation Analysis of a Jordan Block," *SIAM J. Matrix Anal. Appl.*, vol. 32, no. 1, pp. 1–22, Jan. 2011, doi: 10.1137/090761215.

[25] F. Zhang, "Quaternions and matrices of quaternions," *Linear Algebra Its Appl.*, vol. 251, pp. 21–57, Jan. 1997, doi: 10.1016/0024-3795(95)00543-9.

[26] Pozar, David, *Microwave Engineering*. Hoboken, NJ: Wiley, 2012.

[27] M. A. K. Othman, F. Yazdi, A. Figotin, and F. Capolino, “Giant gain enhancement in photonic crystals with a degenerate band edge,” *Phys. Rev. B*, vol. 93, no. 2, p. 024301, Jan. 2016, doi: https://doi.org/10.1103/PhysRevB.93.024301

[28] J. R. Burr, N. Gutman, C. Martijn de Sterke, I. Vitebskiy, and R. M. Reano, “Degenerate band edge resonances in coupled periodic silicon optical waveguides,” *Opt. Express*, vol. 21, no. 7, pp. 8736–8745, Apr. 2013, doi: 10.1364/OE.21.008736.

CHAPTER 6

Experimental Demonstration of Sixth Order Degenerate Band Edge in Coupled Microstrip Waveguides

Sec. 6.1 Motivation

In this chapter we show the first physical realization and experimental demonstration of an exceptional point of 6^{th} order in a triple ladder (or three-way) microwave waveguide realized using three coupled microstrips on a grounded dielectric substrate. This three-way waveguide supports six Bloch eigenmodes and all coalesce onto a degenerate single eigenmode at a given frequency. The three-way waveguide is gainless, and this exceptional point is associated to a vanishing group velocity and its multiple derivatives. Indeed the $\omega - k$ dispersion diagram has six coalescing branches that we call the 6^{th} order degenerate band edge (6DBE). We provide the first experimental verification of this kind of 6^{th} order exceptional point by reconstructing the degenerate wavenumber-frequency dispersion

diagram from the measurement of scattering parameters of a six-port unit cell, and also by observing the coalescence of the six system's eigenvectors obtained from measurements. The unique properties of 6DBE can be exploited in designing innovative high-Q resonators, oscillators, filters, and pulse shaping devices.

Degeneracy of order six in electromagnetic waveguides means that six eigenmodes coalesce and form a single degenerate mode. Here, we imply that the degeneracy is in both *wavenumbers* and *polarization states* of the six Bloch eigenmodes in a waveguide, forming the so-called 6DBE.

A particular class of exceptional points of degeneracy (EPD) in periodic structures is known as a degenerate band edge (DBE) where *four* eigenmodes in a periodic passive, lossless, waveguide coincide at the band-edge [1]–[5]. Note that the presence of the DBE and the 6DBE, discussed here, do not require the presence of losses and gain in the system. The fourth-order DBE has been shown in periodic layered media [1], periodic transmission lines [6], [7], metallic [3] and optical waveguides [8]–[10]. Experimental demonstration of the DBE has been shown in microstrip technology [5], a circular metallic waveguide [11], and an optical waveguide [9]. A strong resonance has been shown experimentally in Ref. [12] using a variation of the DBE, called split band edge. In Ref. [6], a double ladder periodic microstrip waveguide was introduced that exhibits a DBE, and in Ref. [5], it was shown that such a structure exhibits higher quality factor and stability advantages associated with DBE resonance. In Ref. [13], implementation of a three-way partially coupled microstrip waveguide using lumped elements was presented, demonstrating a stationary inflection

point (SIP) associated to a real wavenumber, which is a special EPD of order three realizable in lossless waveguides.

Here, we demonstrate theoretically and experimentally the existence of a sixth-order degeneracy (6DBE) in the Bloch wavenumber-frequency dispersion relation for a periodic waveguide implemented by three coupled microstrip lines. This condition happens when six Floquet-Bloch modes (eigenstates) coincide at the center of the Brillouin zone, here intended with the wavenumber interval of $(0,2\pi/d)$ where d is the period of the waveguide. At a 6DBE, the modal Floquet-Bloch dispersion is characterized by $(\omega_d - \omega) \propto (k - k_d)^6$ where k is the Floquet-Bloch wavenumber, ω is the angular frequency, $k_d = \pi/d$ is the 6DBE wavenumber (at the center of the Brillouin zone), and ω_d is the angular frequency at which the 6DBE occurs. The exponent 6 indicates the sixth order degeneracy, implying that not only the group velocity $v_g = \partial\omega/\partial k$ of the Floquet-Bloch mode vanishes at the 6DBE, but also $\partial^n\omega/\partial k^n = 0$ for n = 1 to 5, while $\partial^6\omega/\partial k^6 \neq 0$.

We provide a simple implementation of the 6DBE in a three-way waveguide made of three coupled microstrips over a grounded dielectric substrate. The unit cell of the three-way microstrip is a 6-port network that is an extension of the 4-port unit cell circuit of lumped elements in Ref. [14] and of the 4-port unit cell microstrip line in Ref. [5]. Implementation in other waveguide technologies involving a three-way structure (i.e., three coupled waveguides) is possible as well. Note that in general terms of idealized propagation based on coupled mode theory, a sixth-order degeneracy was already discussed in Ref. [8]. Furthermore, the 6DBE was already shown via transmission line

simulations in a coupled-resonator optical waveguide (CROW), together with a possible application as a low-threshold laser [15]. This paper aims to experimentally demonstrate the occurrence of the 6DBE in a waveguide at microwave frequencies and to show the resonance behavior in a cavity made of a finite-length structure.

In Section 6.2, the geometry of the unit cell of the periodic microstrip waveguide supporting a 6DBE is provided where the degeneracy behavior is shown in the modal dispersion diagram of the infinitely long periodic lossless structure using simulation based on circuit models implemented in well-known commercial software packages. In Section 6.3, the resonance behavior of a periodic waveguide with finite length of cascaded unit cells is investigated. In Section 6.4, the experimental verification of the 6DBE existence in the microstrip waveguide is provided by carrying out scattering parameters measurements on a single periodic unit cell, where both full-wave simulations and measurements are in very good agreement. The occurrence of the 6DBE is also demonstrated by showing the vanishing of the coalescence parameter, i.e., a parameter that measures the hyperdistance among the 6 eigenvectors in the waveguide system.

Sec. 6.2 Exceptional Degeneracy of 6th Order

To obtain a 6DBE in *reciprocal* waveguide structures, at least three coupled waveguides are required that allow six modes to exist, three modes in each direction. These six modes coalesce into a single mode at the 6DBE frequency ω_d, by resorting to proper coupling and symmetry breaking in the three periodic waveguides. In Fig. 6.1(a), the proposed unit cell of such a three-way periodic waveguide is shown. The structure has period of d = 30 mm.

For its characterization, we define six microstrips electromagnetic "ports". We consider first a lossless structure made of microstrip coupled transmission lines that are implemented on a grounded dielectric substrate) with a thickness of 0.508 mm (20 mils), and a dielectric constant of 3.

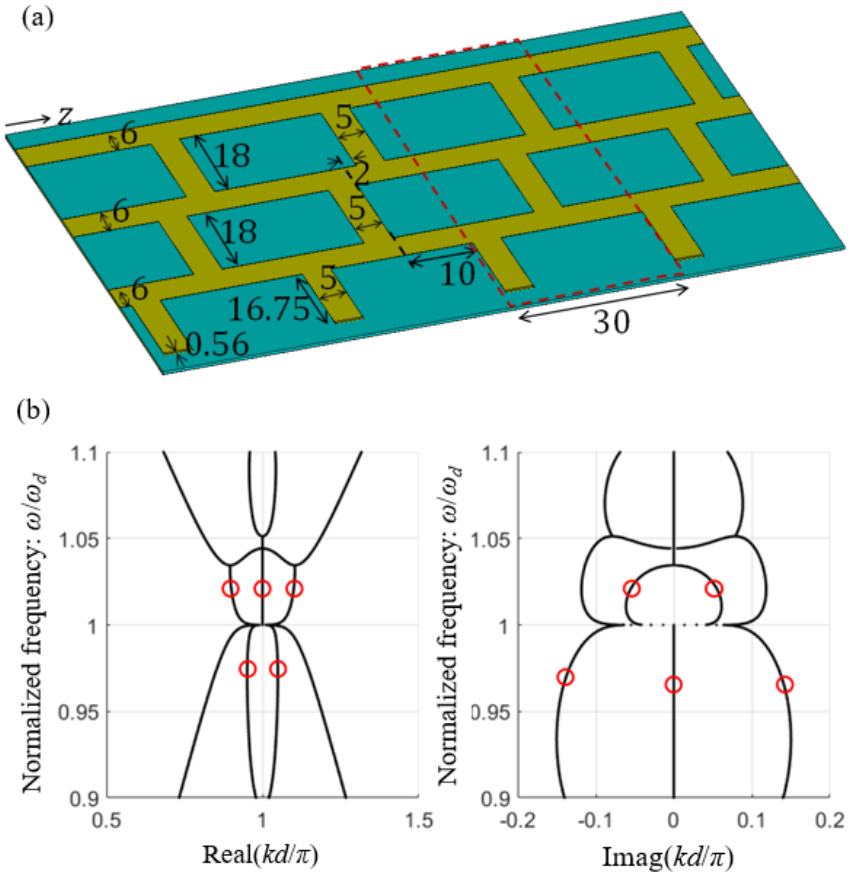

Fig. 6.1 (a) Periodic "three-way" waveguide unit cell, made of three coupled microstrip lines, that exhibits a sixth order DBE. The grounded substrate has a dielectric constant of 3 and the stubs are short circuited at their end. Dimensions shown are in mm. (b) Wavenumber-frequency dispersion diagram of the six Floquet-Bloch eigenmodes in the periodic three-way waveguide showing the 6DBE frequency at f_d = 2.95 GHz, where six dispersion curves coalesce at the single point with wavenumber $k_d = \pi/d$. Branches that represent two modes are denoted by a dashed blue circle. When losses are considered, the dispersion diagram is modified and shown later in Fig. 6.3. The ADS results is obtained by T. Mealy and F. Yazdi.

To analyze and calculate the eigenmodes of the periodic waveguide, we use a transfer matrix formalism, which is discussed in detail in Refs. [16], [17]. We define a six-dimensional state-vector $\mathbf{\Psi}(z) = [\mathbf{V}^T(z) \quad \mathbf{I}^T(z)]^T$ to describe the evolution of the eigenmodes, where T denotes the transpose operation, $\mathbf{V}(z) = [V_1, V_2, V_3]^T$ and $\mathbf{I}(z) = [I_1, I_2, I_3]^T$ are the vectors that represent the voltage (referred to the ground) and current at each of the three microstrips [18]. The evolution of this state vector from a coordinate z_1 to z_2 is then described by $\mathbf{\Psi}(z_2) = \underline{\mathbf{T}}(z_2, z_1)\mathbf{\Psi}(z_1)$, in which $\underline{\mathbf{T}}$ is the 6×6 transfer matrix [16]. In transmission line (TL) circuit simulations, $\underline{\mathbf{T}}$ is obtained by knowing the TL formulas based on the characteristic impedance and the propagation constant of each microstrip segment**.** In full-wave simulations and measurements, the transfer matrix is obtained from the 6×6 S-parameters matrix for the 6-port unit cell. The six Floquet-Bloch eigenmodes satisfying $\mathbf{\Psi}(z + d) = e^{-jkd}\mathbf{\Psi}(z)$ where d is the length of the unit cell shown in Fig. 6.1(a), supported by the periodic triple waveguide are then obtained by solving the eigenvalue problem

$$\det\left[\underline{\mathbf{T}}(z + d, z) - e^{-jkd}\underline{\mathbf{1}}\right] = 0, \tag{6.1}$$

where $\underline{\mathbf{1}}$ is the 6×6 identity matrix, and we have assumed an implicit time convention $\exp(j\omega t)$. The dispersion diagram, which is the relation between the applied frequency and the Bloch wavenumbers in an ideal, i.e., lossless, and infinitely long periodic structure, is depicted in Fig. 6.1(b), calculated using the distributed circuit simulator implemented in Advanced Design System (ADS) by Keysight. The dispersion diagram is obtained by evaluating the eigenvalues $\exp(-jkd)$ derived from the transfer matrix of the three-way

waveguide unit cell at each frequency and then converted to Bloch wavenumbers. At the 6DBE frequency of 2.98 GHz, one observes that six curves coalesce (some curves represent two modes, denoted by a light-blue circle) and the dispersion relation is locally characterized as $(\omega_d - \omega) \approx h(k - k_d)^6$, where h is a parameter that defines the flatness of the dispersion near the degeneracy frequency $f_d = \omega_d/(2\pi)$ = 2.95 GHz. Based on the real and imaginary branches of the dispersion diagram shown in Fig. 6.1(b), no mode can propagate in a frequency range just above ω_d because of a bandgap (indeed Im(k) ≠ 0 for all six modes). In the range $0.9\, f_d < f < f_d$ only two modes can propagate (one in each z-direction), and the four other modes are evanescent since they have Im(k/k_d) ≠ 0; below $f = 0.9\, f_d$ other cutoff conditions occur but are not discussed in this chapter since they do not exhibit a sixth order degeneracy. In the structure composed of the three-way unit cell of Fig. 6.1(a), working at a frequency near the 6DBE frequency, interesting features are observed such as "giant" resonance, enhanced quality factor and the unique energy distribution inside 6DBE cavity, in analogy to what was observed in waveguides with a fourth-order DBE [1], [4], [17], [18].

The 6DBE condition is manifested when the transfer matrix $\underline{\mathbf{T}}$ is "defective," and a complete basis of eigenvectors cannot be found [19], [20]. The 6DBE is obtained by properly choosing the coupling between the three coupled waveguides (TLs), and it can be shown that the six independent eigenvectors coalesce into a single degenerate eigenvector. This degeneracy occurs if, and only if, the transfer matrix $\underline{\mathbf{T}}$ is similar to a 6×6 Jordan canonical matrix form as discussed in Refs. [5], [10]. The coalescence of the six eigenvectors can be demonstrated using the coalescence parameter concept introduced in

Ref. [5] for a fourth order degeneracy, and discussed next for the 6DBE, showing that the distance between the six eigenvectors decreases to a minimum value that depends on the amount of losses and tolerances in the system.

Sec. 6.3 Resonance of Passive Cascaded Circuit

We observe the resonance of a passive waveguide made of a finite number of cascaded unit cells shown in Fig. 6.1(a). The full-wave analysis here accounts for all losses in the dielectric, conductor, and radiation losses. We use the same substrate introduced in Section 6.2 with a loss tangent of $\tan\delta = \varepsilon''/\varepsilon' = 0.001$ (Rogers RO3003) and with conductors (microstrip and ground plane) that are made of copper with a thickness of 35 μm and a conductivity of 5.8×10^7 S/m. The 6DBE analyzed in the previous section assumed an infinitely long periodic waveguide. A resonator made of a finite-length waveguide with unit cells as in Fig. 6.1(a) exhibits its resonance, called 6DBE resonance, at a frequency close to f_d. Such resonance exhibits some interesting and unique properties shown in Ref. [4], such as high-quality factor and its scaling with the resonator length and the distinctive energy distribution inside the finite-length cavity, which are beneficial in an oscillator, sensing and pulse shaping applications [17], [21], [22].

We study the resonance behavior by constructing a finite structure made of 8 unit cells as shown in Fig. 6.2(a) with all terminals connected to a short circuit except the middle TL at the structure's left end, that is connected to an ideal phasor voltage source of 1 V at the input of the resonator and observe the voltage distribution inside the resonator. We perform transmission line simulations based on the scattering parameters obtained from

the full-wave simulation of one-unit-cell. Full-wave simulations are used to evaluate the 6×6 scattering matrix of a unit-cell. Full-wave simulation are based on the finite element frequency domain solver implemented in CST Studio Suite by DS SIMULIA. The short circuit at the of the stub is made of a conductor via with same width of the microstrip stub and with length of 0.56 mm as shown in Fig. 6.1(a).

As explained earlier, the scattering matrix is then transformed into a 6×6 transfer matrix of a unit cell. The voltage distributions at the various circuit nodes are calculated by cascading the transfer matrices of the unit cells.

In Fig. 6.2(b) the frequency response of the voltage at the middle of the structure with 8 unit cells is plotted where a peak is observed for each of the three microstrip lines at a resonance frequency close to the 6DBE frequency, i.e., $f_{r,6DBE}$ =2.988 GHz. Fig. 6.2(c) shows the voltage distribution inside the eight cells resonator at $f = f_{r,6DBE}$, and we see that the voltage is concentrated around the middle of the structure, in particular in the lower TL, shown in Fig. 6.2(a), having the highest magnitude. This unique voltage distribution implies that anything connected, like a loading resistor, at the edges of the periodic waveguide will have a minor effect on the rest of the structure. The voltage distribution in a 6DBE cavity is analogous to that obtained in resonators having second or fourth order DBE [23]. This physical property has been found useful in conceiving new regimes of oscillation [24], and the voltage distribution provides the information of where an active device can be placed to have the most significant impact [21]. It also demonstrates the "slow light" effect associated with DBE, where the energy is trapped

inside the cavity at a frequency near f_d [23].

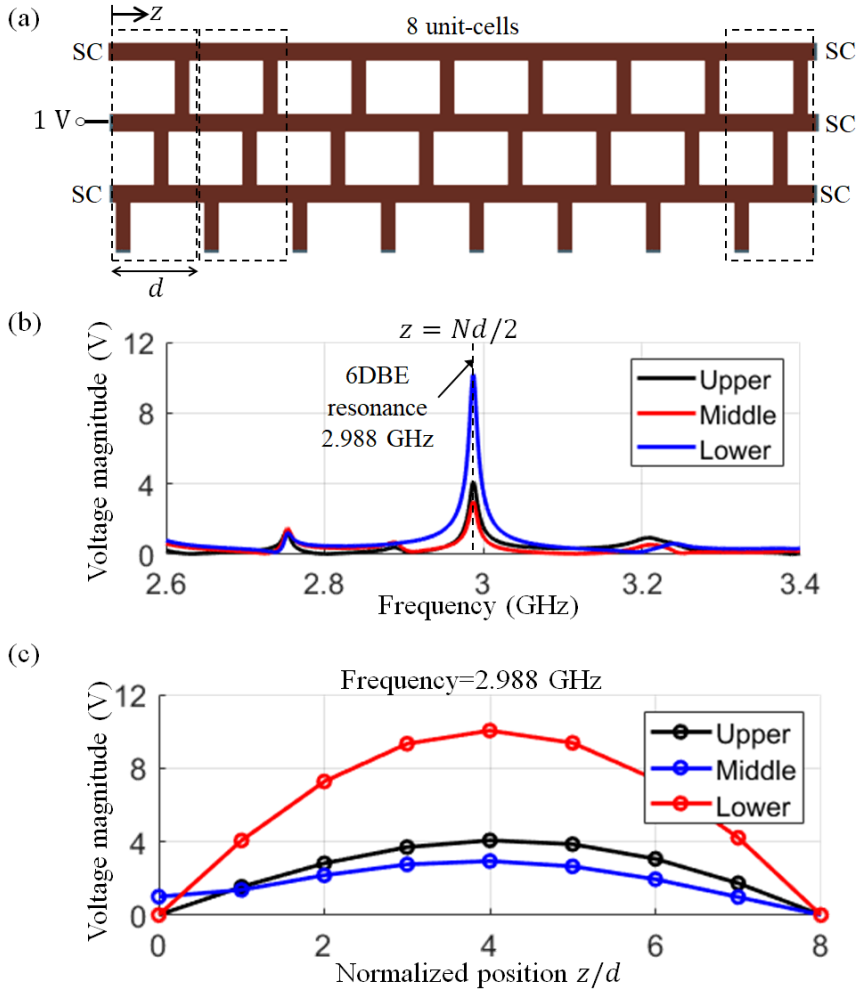

Fig. 6.2 (a) A resonance cavity formed by cascading 8 unit cells. The left and right terminations are shorted to the ground except for the middle line at the left end of the structure. We have applied a phasor voltage of 1 V as input to the resonator. (b) Frequency response of the voltage at the middle of the cavity where a resonance peak is observed at a frequency close to the 6DBE frequency. (c) Voltage profile across the structure at the 6DBE resonance frequency showing the voltage distribution at each period of the three TLs. This result is obtained by T. Mealy and A. Nikzamir.

Sec. 6.4 Experimental Verification of 6DBE in Periodic Microstrip Circuit

In this section, the experimental verification of the existence of the sixth order EPD in the microstrip three-way waveguide shown in Fig. 6.1(a) is presented. We use a grounded dielectric substrate (Rogers RO3003) and conductors as in the previous section where we have discussed full-wave simulations. The fabricated unit-cell is shown in Fig. 6.3(a) including SMA connectors. The dispersion diagram obtained from measurement of the 6×6 S-parameters matrix, along with the full-wave simulation results (as in previous section) are shown in Fig. 6.3(b). They are in a good agreement, although a shift in frequency is observed due to fabrication imperfections (especially knowing exactly the lines' length) and high sensitivity of the sixth order degeneracy to perturbations. The dispersion diagram shows the coalescence of the six modes based on measurements at the degeneracy frequency $f_d = \omega_d /(2\pi) = 2.95$ GHz. The measurement results were obtained by measuring the scattering parameters of the unit cell shown in Fig. 6.3(a) using a Rohde & Schwarz ZVA67 Vector Network Analyzer (VNA). The 6×6 S-parameters matrix was acquired by only using 2 ports of the VNA at a time as illustrated in the following way. Port 1 of the VNA is connected to port m of the unit cell while, port 2 of the VNA is connected to port n of the unit cell while the four other ports are terminated by a 50 Ω load, to measure $S(m,n)$ (as well as $S(n,m)$). The obtained S-parameters are smoothed out over frequency using Matlab to eliminate the effect of random noise. Once the 6×6 S-parameters matrix is constructed, we obtained the 6×6 transfer matrix $\underline{\mathbf{T}}$ from which the Bloch wavenumbers are solved for (as described previously). The wavenumbers for the measured and simulated results are plotted versus frequency to obtain the dispersion diagram shown in

Fig. 6.3(b).

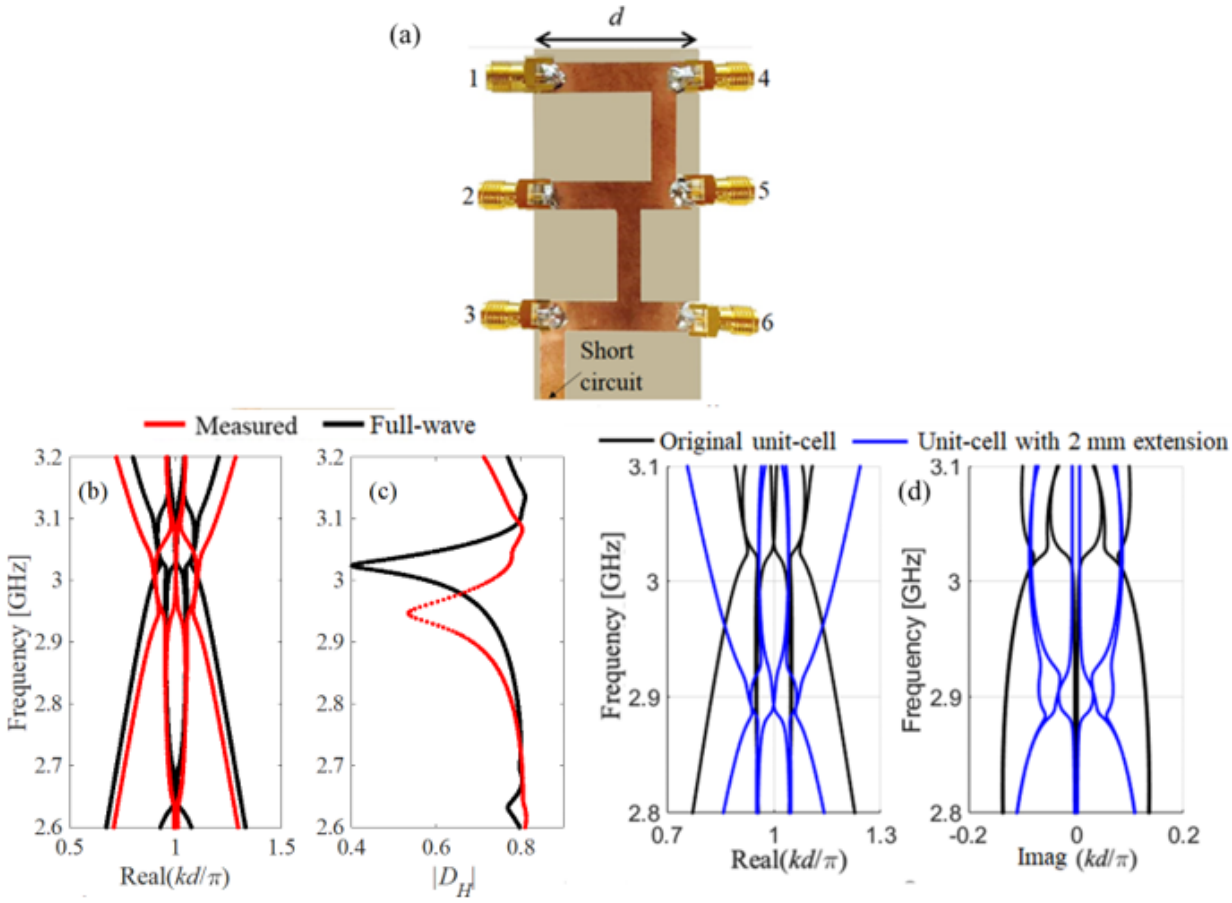

Fig. 6.3 (a) Fabricated unit cell of the proposed periodic three-way waveguide implemented in microstrip technology. (b) Bloch wavenumbers dispersion based on measurement (red dots) versus the one obtained via Method of Moments full-wave electromagnetic simulation (solid black). Both measurement and simulation are based on a six-port evaluation of the scattering parameters of the unit cell. Six modes coalescing are clearly visible, though the coalescence is not perfect because of losses and manufacturing imperfections. (c) Coalescence factor, D_H in linear scale versus frequency around the 6DBE, as a measure of closeness to the 6DBE, for the full-wave simulation results, in comparison to the measured results. (d) Tunability of 6DBE showing dispersion diagrams obtained from full-wave simulation of unit cell in Fig. 6.1(a) (black) and same unit cell after adding 1mm extension of transmission line at each port (period is extended by 2mm). The comparison shows that 6DBE frequency is very sensitive to any added extra length. Simulation results are done by T. Mealy, A. Nikzamir, and F. Yazdi, and measurements are done by D. Oshmarin and A. Almutawa.

These results show some perturbation and deviation from the ideal degeneracy condition (flat dispersion diagram at 6DBE frequency) in Fig. 6.1(b). The perturbation is due to the ohmic, dielectric and radiation losses of the waveguide, and to tolerances in the fabrication.

Since an EPD is very sensitive to perturbations, we use a figure of merit to describe "how close" we are to an EPD, based on the concept of *coalescence factor* or *hyperdistance*, $D_H(\omega)$, *between the six eigenvectors* of the transfer matrix of one-unit cell $\underline{\mathbf{T}}$ defined in [5]. The hyperdistance that defines the closeness to the 6DBE is defined as

$$D_H = \frac{1}{15}\sum_{\substack{m=1,n=1 \\ m\neq n}}^{6} |\sin(\theta_{mn})|\,, \cos(\theta_{mn}) = \frac{|(\boldsymbol{\Psi}_m, \boldsymbol{\Psi}_n)|}{\|\boldsymbol{\Psi}_m\|\|\boldsymbol{\Psi}_n\|} \tag{6.2}$$

where θ_{mn} represents the angle between two eigenvectors $\boldsymbol{\Psi}_m$ and $\boldsymbol{\Psi}_n$ in a six-dimensional complex vector space, with norms $\|\boldsymbol{\Psi}_m\|$ and $\|\boldsymbol{\Psi}_n\|$, and $(\boldsymbol{\Psi}_m, \boldsymbol{\Psi}_n)$ as their inner product. This coalescence factor helps to determine the closeness of a system to having a 6DBE and to distinguish this 6DBE from other EPDs with different orders (like the regular band edge or the DBE). The coalescence factor presented here is a very convenient figure to assess if an EPD occurs in reality, when losses and other perturbations present. Indeed, the perfect 6DBE exists only mathematically. However, a system can still preserve the full degeneracy properties when the eigenvectors are very close to each other, i.e., in a neighborhood of the 6DBE. The coalescence factor, D_H, is plotted in Fig 6.3(c) as a function of frequency, accounting for all dissipative and radiative losses, showing a good agreement between the two results based on measurement and full-wave simulations, besides a frequency shift. It

can be seen that D_H has the minimum value in the vicinity of the 6DBE frequency ($f = f_d$) as expected. In an ideal lossless case, it is expected that $D_H \to 0$ at the exact EPD.

It is important to point out that the shift in the 6DBE frequency in the dispersion diagrams obtained from the measurement and full-wave simulation is mainly due to the extra lengths accounted in the SMA connectors. Deemebeding techniques, similar to the ones in [25], [26], can be applied to remove the effect of the SMA connectors on the measurement. Note that the dispersion obtained from measurement in Fig. 6.3(b) preserves the shape of 6DBE although deembeding was not performed. We confirmed that the frequency shift is mainly due to the described effect by performing another full-wave simulation for unit cell in Fig. 6.1(a), for a similar unit cell but after adding 1mm extension of TL at each port (hence the unit-cell period is extended by 2mm). We show in Fig. 6.3(d) a comparison between the two dispersion diagrams that shows that the length extension does not impact the occurrence of 6DBE but rather shifts its frequency. Therefore, we concluded that the SMA connectors extra lengths might lower the frequency at which the 6DBE occurs as observed in Fig. 6.3(b). This result also shows a possible way to tune the 6DBE frequency.

Sec. 6.5 Conclusion

A physical realization of a novel three-way periodic waveguide exhibiting a sixth-order degeneracy (6DBE) is demonstrated for the first time using microstrip technology. The 6DBE is an exceptional point of order six where six eigenstates coalesce onto a single degenerate one. Both theoretical and experimental verifications are provided. Remarkable

physical properties may arise due to this strong sixth-order exceptional point of degeneracy including increased quality factor, high density of states, and sensitivity which can lead to novel designs for microwave and optical pulse generation [17], microwave and millimeter wave oscillators [21], [22], [24], low threshold lasers [15], [27], short delay lines with significant group delay, filters, and ultra-sensitive sensors.

This chapter is reproduced in part based on the material in [F. Yazdi, D. Oshmarin, T. Mealy, A. Almutawa, A. Nikzamir, and F. Capolino, "Experimental Demonstration of Sixth Order Degenerate Band Edge in Coupled Microstrip Waveguides", in submission to a peer-reviewed journal].

References

[1] A. Figotin and I. Vitebskiy, "Frozen light in photonic crystals with degenerate band edge," *Phys. Rev. E*, vol. 74, no. 6, p. 066613, 2006.

[2] A. Figotin and I. Vitebskiy, "Slow wave phenomena in photonic crystals," *Laser Photonics Rev.*, vol. 5, no. 2, pp. 201–213, 2011.

[3] M. A. Othman and F. Capolino, "Demonstration of a degenerate band edge in periodically-loaded circular waveguides," *IEEE Microw. Wirel. Compon. Lett.*, vol. 25, no. 11, pp. 700–702, 2015.

[4] M. A. Othman, F. Yazdi, A. Figotin, and F. Capolino, "Giant gain enhancement in photonic crystals with a degenerate band edge," *Phys. Rev. B*, vol. 93, no. 2, p. 024301, 2016.

[5] A. F. Abdelshafy, M. A. K. Othman, D. Oshmarin, A. T. Almutawa, and F. Capolino, "Exceptional Points of Degeneracy in Periodic Coupled Waveguides and the Interplay of Gain and Radiation Loss: Theoretical and Experimental Demonstration," *IEEE Trans. Antennas Propag.*, vol. 67, no. 11, pp. 6909–6923, Nov. 2019, doi: 10.1109/TAP.2019.2922778.

[6] C. Locker, K. Sertel, and J. L. Volakis, "Emulation of Propagation in Layered Anisotropic Media With Equivalent Coupled Microstrip Lines," *IEEE Microw. Wirel. Compon. Lett.*, vol. 16, no. 12, pp. 642–644, Dec. 2006, doi: 10.1109/LMWC.2006.885586.

[7] J. L. Volakis and K. Sertel, “Narrowband and wideband metamaterial antennas based on degenerate band edge and magnetic photonic crystals,” *Proc. IEEE*, vol. 99, no. 10, pp. 1732–1745, 2011.

[8] N. Gutman, C. Martijn de Sterke, A. A. Sukhorukov, and L. C. Botten, “Slow and frozen light in optical waveguides with multiple gratings: Degenerate band edges and stationary inflection points,” *Phys. Rev. A*, vol. 85, no. 3, p. 033804, Mar. 2012, doi: 10.1103/PhysRevA.85.033804.

[9] M. G. Wood, J. R. Burr, and R. M. Reano, “Degenerate band edge resonances in periodic silicon ridge waveguides,” *Opt. Lett.*, vol. 40, no. 11, pp. 2493–2496, Jun. 2015, doi: 10.1364/OL.40.002493.

[10] M. Y. Nada, M. A. K. Othman, and F. Capolino, “Theory of coupled resonator optical waveguides exhibiting high-order exceptional points of degeneracy,” *Phys. Rev. B*, vol. 96, no. 18, p. 184304, Nov. 2017, doi: 10.1103/PhysRevB.96.184304.

[11] M. A. K. Othman, X. Pan, G. Atmatzakis, C. G. Christodoulou, and F. Capolino, “Experimental Demonstration of Degenerate Band Edge in Metallic Periodically Loaded Circular Waveguide,” *IEEE Trans. Microw. Theory Tech.*, vol. 65, no. 11, pp. 4037–4045, Nov. 2017, doi: 10.1109/TMTT.2017.2706271.

[12] A. A. Chabanov, “Strongly resonant transmission of electromagnetic radiation in periodic anisotropic layered media,” *Phys. Rev. A*, vol. 77, no. 3, p. 033811, Mar. 2008, doi: 10.1103/PhysRevA.77.033811.

[13] G. Mumcu, K. Sertel, and J. L. Volakis, “Lumped circuit models for degenerate band edge and magnetic photonic crystals,” *IEEE Microw. Wirel. Compon. Lett.*, vol. 20, no. 1, pp. 4–6, 2010.

[14] J. T. Sloan, M. A. K. Othman, and F. Capolino, “Theory of Double Ladder Lumped Circuits With Degenerate Band Edge,” *IEEE Trans. Circuits Syst. Regul. Pap.*, vol. 65, no. 1, pp. 3–13, Jan. 2018, doi: 10.1109/TCSI.2017.2690971.

[15] M. Y. Nada and F. Capolino, “Exceptional point of sixth-order degeneracy in a modified coupled-resonator optical waveguide,” *JOSA B*, vol. 37, no. 8, pp. 2319–2328, Aug. 2020, doi: 10.1364/JOSAB.385198.

[16] M. A. Othman, V. A. Tamma, and F. Capolino, “Theory and new amplification regime in periodic multimodal slow wave structures with degeneracy interacting with an electron beam,” *IEEE Trans. Plasma Sci.*, vol. 44, no. 4, pp. 594–611, 2016.

[17] V. A. Tamma, A. Figotin, and F. Capolino, “Concept for Pulse Compression Device Using Structured Spatial Energy Distribution,” *IEEE Trans. Microw. Theory Tech.*, vol. 64, no. 3, pp. 742–755, Mar. 2016, doi: 10.1109/TMTT.2016.2518160.

[18] C. R. Paul, *analysis of multiconductor transmission lines*, 2nd ed. New York: Wiley-IEEE Press, 2007.

[19] N. Dunford, J. Schwartz, and W. Bade, *Linear operators*. New York: Wiley-interscience, 1971.

[20] T. Kato, *Perturbation Theory for Linear Operators*, 2nd ed. Berlin Heidelberg: Springer-Verlag, 1995. Accessed: May 02, 2019. [Online]. Available: https://www.springer.com/us/book/9783540586616

[21] D. Oshmarin *et al.*, "New oscillator concept based on band edge degeneracy in lumped double-ladder circuits," *IET Circuits Devices Syst.*, vol. 13, no. 7, pp. 950–957, 2019, doi: 10.1049/iet-cds.2018.5048.

[22] M. Y. Nada *et al.*, "Microwave Circuits with Exceptional Points and Applications in Oscillators and Sensors," in *2018 18th Mediterranean Microwave Symposium (MMS)*, Oct. 2018, pp. 108–111. doi: 10.1109/MMS.2018.8611828.

[23] A. Figotin and I. Vitebskiy, "Slow light in photonic crystals," *Waves Random Complex Media*, vol. 16, no. 3, pp. 293–382, 2006.

[24] A. F. Abdelshafy, D. Oshmarin, M. A. K. Othman, M. M. Green, and F. Capolino, "Distributed Degenerate Band Edge Oscillator," *IEEE Trans. Antennas Propag.*, vol. 69, no. 3, pp. 1821–1824, Mar. 2021, doi: 10.1109/TAP.2020.3018539.

[25] N. Apaydin, L. Zhang, K. Sertel, and J. L. Volakis, "Experimental Validation of Frozen Modes Guided on Printed Coupled Transmission Lines," *IEEE Trans. Microw. Theory Tech.*, vol. 60, no. 6, pp. 1513–1519, Jun. 2012, doi: 10.1109/TMTT.2012.2192746.

[26] M. Y. Nada, T. Mealy, and F. Capolino, "Frozen Mode in Three-Way Periodic Microstrip Coupled Waveguide," *IEEE Microw. Wirel. Compon. Lett.*, vol. 31, no. 3, pp. 229–232, Mar. 2021, doi: 10.1109/LMWC.2020.3042205.

[27] M. Veysi, M. A. K. Othman, A. Figotin, and F. Capolino, "Degenerate band edge laser," *Phys. Rev. B*, vol. 97, no. 19, p. 195107, May 2018, doi: 10.1103/PhysRevB.97.195107.

The End